



HAL
open science

Poles and zeros of the scattering matrix and coherent perfect absorption in tunable reverberating environments

Junjie Lu

► **To cite this version:**

Junjie Lu. Poles and zeros of the scattering matrix and coherent perfect absorption in tunable reverberating environments. Quantum Physics [quant-ph]. Université Côte d'Azur, 2024. English. NNT : 2024COAZ5048 . tel-04818283

HAL Id: tel-04818283

<https://theses.hal.science/tel-04818283v1>

Submitted on 4 Dec 2024

HAL is a multi-disciplinary open access archive for the deposit and dissemination of scientific research documents, whether they are published or not. The documents may come from teaching and research institutions in France or abroad, or from public or private research centers.

L'archive ouverte pluridisciplinaire **HAL**, est destinée au dépôt et à la diffusion de documents scientifiques de niveau recherche, publiés ou non, émanant des établissements d'enseignement et de recherche français ou étrangers, des laboratoires publics ou privés.

THÈSE DE DOCTORAT

Pôles et zéros de la matrice de diffusion
et absorption parfaite cohérente dans les
environnements réverbérants réglables

Junjie Lu

Institut de Physique de Nice

Presentée en vue de
l'obtention du grade de
docteur en Physique
d'Université Côte d'Azur

Dirigée par : Ulrich Kuhl / Olivier Legrand

Soutenue le : 20 Septembre 2024

Devant le jury, composé de :

Matthieu Davy,
Professeur,
IETR, Université de Rennes

Tsampikos Kottos,
Professeur,
Wesleyan University

Ulrich Kuhl,
Professeur,
INPHYNI, Université Côte d'Azur

Oliver Legrand,
Professeur,
INPHYNI, Université Côte d'Azur

Claire Migliaccio,
Professeure,
LEAT, Université Côte d'Azur

Dmitry Savin,
Maître de conférences,
Brunel University London

**Pôles et zéros de la matrice de diffusion
et absorption parfaite cohérente dans les
environnements réverbérants réglables**

**Poles and zeros of the scattering matrix
and coherent perfect absorption in
tunable reverberating environments**

Jury:

Rapporteurs

Matthieu Davy, *Professeur*, IETR, Université de Rennes
Tsampikos Kottos, *Professeur*, Wesleyan University

Examineurs

Claire Migliaccio, *Professeure*, LEAT, Université Côte d'Azur
Dmitry Savin, *Maître de conférences*, Brunel University London

Directeur de thèse

Ulrich Kuhl, *Professeur*, INPHYNI, Université Côte d'Azur

Co-directeur de thèse

Olivier Legrand, *Professeur*, INPHYNI, Université Côte d'Azur

Résumé

Dans la thèse, je présente des résultats expérimentaux sur les réseaux micro-ondes et les chambres réverbérantes. La description générale est basée sur la théorie de la diffusion, décrivant la réflexion et la transmission via les pôles et les zéros de la matrice de diffusion. Les pôles et les zéros peuvent être déterminés par l'approche de l'hamiltonien effectif, où couplage et perte peuvent être pris en compte de manière appropriée. La thèse est divisée en deux thèmes de recherche principaux : le premier concerne les réseaux micro-ondes, simulant des graphes quantiques, abordant les comportements non-Weyl se produisant en raison de l'ouverture du système. Le second est dédié à l'absorption parfaite cohérente (CPA) dans les chambres réverbérantes à fortes pertes.

Les réseaux hyperfréquences sont décrits par des liaisons reliées par des vertex. Pour la première fois, une variation de la force de couplage au réseau est implémentée expérimentalement. Ceci est réalisé en utilisant une liaison pendante de longueur variable attachée au vertex de couplage. Ainsi, nous faisons varier indirectement la condition aux limites au vertex de couplage de Dirichlet à Neumann. En suivant les pôles dans le plan complexe, on peut observer la fuite des pôles via une transition superradiante. Ces pôles manquants conduisent à une réduction du nombre de pôles, rendant ainsi nécessaire un ajustement de la loi de Weyl, appelée comportement non-Weyl dans les graphes. Cela a été observé pour la première fois dans des graphes tétraédriques ouverts, qui montrent une dynamique paramétrique complexe des pôles. Cette dynamique riche est constituée de boucles, de régions de pôles connectés et de pôles se rapprochant d'une partie imaginaire infinie. Les principales caractéristiques se trouvent déjà dans les graphes de type lasso, qui peuvent être résolus analytiquement.

Le deuxième sujet concerne les chambres réverbérantes, où les ondes électromagnétiques sont diffusées dans un environnement accordable. Par rapport aux chambres réverbérantes standards, celle-ci est équipée de surfaces intelligentes reconfigurables (RIS). Ces dernières nous permettent d'ajuster les zéros de la matrice de diffusion sur l'axe des fréquences réelles, ce qui correspond à un concept récent nommé CPA en physique des ondes, où aucune onde ne s'échappe d'un système avec perte pour une onde incidente spécifique. Nos résultats expérimentaux imposent que l'existence des CPA ne puisse être expliquée que par les états superradiants correspondants. Cette correspondance est confirmée numériquement à travers une approche matricielle aléatoire basée sur l'hamiltonien effectif en régime de surcouplage, généralement négligé dans les études théoriques. De plus, nous constatons que les zéros de la matrice de diffusion proches de l'axe réel sont plus sensibles dans le cas surcouplé que dans le cas sous-couplé. Enfin, nous démontrons que la CPA peut être utilisée comme sonde de température.

Mots clés: absorption parfaite cohérente, superradiance, théorie des matrices aléatoires, loi de Weyl, réseaux micro-ondes, chambre réverbérante

Abstract

In the thesis, I present experimental results on microwave networks and reverberation chambers. The general description is based on scattering theory, describing the reflection and transmission via poles and zeros of the scattering matrix. The poles and zeros can be determined by the effective Hamiltonian approach, where coupling and loss can be taken into account appropriately. The thesis is divided into two main research subjects: the first one deals with microwave networks, simulating quantum graphs, addressing non-Weyl behavior occurring due to the openness of the system. The second one is dedicated to coherent perfect absorption (CPA) in reverberation chambers with large losses.

Microwave networks are described by bonds which are connected by vertices. For the first time a variation of the coupling strength to the network is experimentally implemented. This is realized by using a dangling bond with variable length attached to the coupling vertex. Thus we indirectly vary the boundary condition at the coupling vertex from Dirichlet to Neumann. Following the poles in the complex plane, one can observe the escape of poles via a superradiant transition. These missing poles lead to a reduction of the number of poles, thus making an adjustment of Weyl's law necessary, which is termed non-Weyl behavior in graphs. This was first observed in open tetrahedral graphs, which show a complex parametric dynamics of the poles. This rich dynamics consists of loops, regions of connected poles and poles approaching infinite imaginary part. The main features can be already found in lasso graphs, which can be solved analytically.

The second subject concerns reverberation chambers, where electromagnetic waves are scattered in a tunable environment. Compared to standard reverberation chambers, this one is equipped with reconfigurable intelligent surfaces (RIS). The latter allow us to tune the zeros of scattering matrix to the real frequency axis, which corresponds to a recent concept named CPA in wave physics, where no wave is escaping from a lossy system for a specific incident wave. Our experimental findings impose that the existence of CPAs can only be explained by corresponding superradiant states. This correspondence is numerically confirmed through a random matrix approach based on the effective Hamiltonian in the over-coupling regime, generally neglected in theoretical studies. Additionally, we find that the zeros of the scattering matrix close to the real axis are more sensitive in the overcoupled case than in the undercoupled one. Finally, we demonstrate that the CPA can be used for temperature sensing.

Keywords: coherent perfect absorption, superradiance, random matrix theory, Weyl's law, microwave networks, reverberation chambers

Acknowledgments

I would like to express my sincere gratitude to the *China Scholarship Council* (CSC) for providing financial support for the work presented in this thesis.

During the years of pursuing my PhD, I came into contact with many people who helped me in many ways to finish my PhD.

Firstly, I would like to thank my jury members for their time in reviewing my manuscript and providing feedback. I thank Claire Migliaccio for being the president of my jury, Matthieu Davy and Tsampikos Kottos for their detailed reviews as rapporteurs, and finally, Dmitry Savin for evaluating my work during the PhD defense.

I would like to thank my supervisors, Ulrich Kuhl and Oliver Legrand, for their invaluable guidance throughout my PhD. Ulle, you were always considerate and ready to lend a helping hand, whether in research problems or personal life. Your constructive criticism reshaped the way I think and significantly improved my skills. Olivier, you always take the time to discuss my work, and your insights often help us solve challenging problems, it's really a pleasure to work with you.

It has been an honor to be part of our research group, *Waves in Complex Systems*. I deeply appreciate to work together with Fabrice Mortessagne, Geoffroy Aubry, Claire Michel, Matthieu Bellec, Valérie Doya, Mattis Reisner, Léo Colliard, Luis-Alberto Razo-Lopez, Carelle Keyrouz, and Lucas Zanaglia. The discussions with them and their suggestions helped me to overcome the situations in which my work seemed stuck.

I am also deeply grateful to Professor Maxime Ingremeau and Thomas Ourmières-Bonafos for their highly efficient collaboration. Their expertise and insightful contributions made our joint work both fruitful and inspiring.

Special thanks go to my collaborator Felix Russo from Vienna University of Technology. Together, we shared three productive months in the lab, successfully completing a challenging experiment.

During my PhD, I had the unique opportunity to work in two other research groups. I spent over two months in Professor Hans-Jürgen Stöckmann's quantum chaos group at the University of Marburg. I was inspired by Professor Stöckmann's passion for physics and grateful for the warm support from the group, especially Finn Schmidt and Tobias Hofmann.

Additionally, I had a memorable experience at Professor Guancong Ma's group at Hong Kong Baptist University, where I had the opportunity to present my work and contribute to an exciting project. I am thankful for the time spent with the group members, especially Xulong Wang, Congwei Lu, Hongkuan Zhang.

I am also grateful to my friends, Alberto, who has accompanied me throughout my entire PhD journey. Together, we shared many activities and countless joyful moments. I would like to thank Sumeyra for her genuine kindness and the warmth she extends to everyone. David introduced me to the world of outdoor adventure.

My Chinese friends have also been an essential part of my journey: Xin has always supported me, encouraged me and witnessed my growth. Dongyu and Xiuheng were my companions in exploring new places, creating unforgettable memories. I would also like to thank Ying, Zhenying, Xi, Zhiyan, Tianyi, Li, Keyu, Chenxi,

Qingwen, Xianzhang, Ziyuan and Yijiao for their friendship.

I wish to thank my partner, Qinlu, for her warm understanding and support throughout this journey. Meeting her has been a source of great comfort and encouragement.

Finally I would like to extend my heartfelt thanks to my family, their unconditional support and care have been my greatest strength, always given without asking for anything in return.

CONTENTS

1	Introduction	1
2	Theoretical Description of Wave Systems	5
2.1	Electromagnetic and Matter Waves	6
2.2	Closed Wave Systems	7
2.2.1	<i>Closed Systems: From 1D to 3D</i>	7
2.2.2	<i>Weyl's Law</i>	9
2.2.3	<i>Random Matrix Theory (RMT)</i>	10
2.3	Open Wave Systems	13
2.3.1	<i>Scattering Systems</i>	14
2.3.2	<i>Effective Hamiltonian Approach</i>	16
2.3.3	<i>Poles and Zeros of the Scattering Matrix</i>	17
2.3.4	<i>Fluctuation Properties of the Scattering Matrix</i>	19
2.3.5	<i>Superradiance</i>	21
3	Superradiance in Non-Weyl Microwave Networks	25
3.1	Quantum Graphs	26
3.1.1	<i>The Vertex Secular Equation</i>	26
3.1.2	<i>Scattering Properties of Graphs</i>	27
3.1.3	<i>Bond Scattering Matrix and Secular Equation</i>	28
3.2	Microwave Networks	30
3.2.1	<i>Microwave Network Components</i>	30
3.2.2	<i>Modeling Variable Phase: Length Transformation</i>	32
3.2.3	<i>Modeling Variable Channel Openness</i>	34
3.3	Weyl's Law in Graphs	36
3.3.1	<i>Weyl Graphs</i>	36
3.3.2	<i>Non-Weyl Graphs</i>	37
3.3.3	<i>Motivation</i>	39
3.4	Non-Weyl Tetrahedral Graphs	40
3.4.1	<i>Microwave Setup</i>	40
3.4.2	<i>Spectra Transformation</i>	40
3.4.3	<i>Experimental Findings</i>	43
3.5	Non-Weyl Lasso Graphs	45
3.5.1	<i>Analytical Description</i>	45
3.5.2	<i>Numerical Findings</i>	46
3.5.3	<i>Rational Lasso Graphs</i>	47
3.5.4	<i>Experimental Findings</i>	48
3.5.5	<i>Other Examples</i>	49
3.6	Conclusion	51
4	Superradiant Coherent Perfect Absorber	53
4.1	Theoretical Background and Motivation	54
4.1.1	<i>Chaotic Reverberation Chamber (CRC)</i>	54
4.1.2	<i>Description of Global and Local Losses</i>	54

Table of Contents

4.1.3	<i>Coherent Perfect Absorption (CPA)</i>	57
4.1.4	<i>Motivation</i>	58
4.2	Experimental Realization of CPA	59
4.2.1	<i>Experimental Setup</i>	59
4.2.2	<i>System Coupling</i>	60
4.2.3	<i>System Loss</i>	62
4.2.4	<i>CPA Optimization</i>	64
4.2.5	<i>Extraction of Zeros</i>	65
4.3	Average Antenna Transmission with Global Loss	69
4.3.1	<i>Theoretical Description</i>	69
4.3.2	<i>Numerical Verification</i>	70
4.3.3	<i>Parameter Relation for Constant Antenna Transmission</i>	72
4.4	Numerical Simulation of Zeros	73
4.4.1	<i>Under and Perfect Coupling</i>	73
4.4.2	<i>Over Coupling</i>	75
4.5	Stirring generated Zeros Dynamics	80
4.5.1	<i>Experimental Findings</i>	80
4.5.2	<i>Numerical Findings</i>	82
4.6	CPA in CRC as Temperature Sensor	83
4.7	Conclusion	85
5	Conclusions and Outlook	87
	Bibliography	89

Chapter 1

Introduction

Already in the early stage of quantum physics, everything we know about nuclear and atomic physics has been explored by scattering experiments, e.g. Rutherford's discovery of the nucleus or neutron or electron scattering in crystals [Rut11, Dav27]. Later in the 1950s and 1960s, interest in wave scattering was diverted to classically chaotic systems, where the main experimental data on spectra and scattering properties came from nuclear physics, where neutrons were scattered on nuclei [Hau52, Por65]. Two main theories were inspired and developed with these experiments: random matrix theory (RMT), initiated by Wigner [Wig55] and extended by Dyson, Mehta et al. [Por65], and scattering theory, proposed by Weidenmüller and colleagues [Mah69]. By the 1980s, the interest in the properties of chaotic systems was suddenly renewed by the conjectures of Casati et al. [Cas80] and Bohigas et al. [Boh84], now known as the Bohigas, Giannoni, Schmit (BGS) conjecture, suggesting that the universal statistical properties of quantum systems with a classical chaotic counterpart should be described by RMT. This conjecture has proved to be extremely useful and injected a new impetus to the field, which has led to intensive research activity in various areas, including nuclear physics, atomic physics, mesoscopic physics, quantum optics, and wave physics, both theoretically and experimentally. Among these, classical wave experiments have become an especially important tool. The earliest analogue experiments using vibrating solids [Wea89] and chaotic microwave cavities [Stö90] were published in 1989 and 1990. Soon after, the idea was extended to water surface and pressure waves [Blü92, Chi96], optical systems [Doy01, Din02] and semiconductors [Mar92].

Microwave experiments, in particular, offer numerous advantages especially compared to matter waves [Stö99]. First of all, they operate on a cm-scale, which is much easier to manipulate compared to the nm-scale of quantum experiments and allows for sub-wavelength precision and excellent control over the systems. Further advantages arise from the fact, that the geometry of microwave system is precisely known and can be easily varied: in 1D microwave networks [Hul04], by varying phase shifter [Bia16]; in 2D microwave billiards, by moving disk [Mén03]; and in 3D reverberation chambers, by rotating stirrers [Bes11] allowing thus to investigate statistical predictions made by RMT. Last but not least, the coupling from external channels can be introduced, varied, and explicitly included in calculations.

Originally, these microwave experiments were designed to study the spectral

properties of closed chaotic systems. However, the introduction of antennas or transducers for measurements inevitably opens the systems. Therefore, for a quantitative interpretation of the measurements, it became necessary to introduce scattering theory and effective Hamiltonian approach [Mah69, Ver85, Sok89] to establish a relation between Green's function of the closed system and the scattering matrix of the open system. This motivated a large number of experimental tests to verify the accuracy of theoretical description in their open systems [Stö99, Kuh13, Stö22].

For open system, discrete eigenvalues no longer exists, now they appear as resonances in the spectrum, or poles of the scattering matrix in the complex plane. This is due to energy decay induced by the coupling to an environment. As a result, many predictions originally used for closed wave systems needed to be adjusted. Such as Weyl's law [Wey12a, Wey12b, Wey12c], a prediction used to describe the density of states of a given closed system. To adapt Weyl's law to open systems, the fractal Weyl's law [Non05, Pot12] was introduced, which counts the resonances of open chaotic systems and reduces the wavenumber exponent due to its chaotic behavior, relating this exponent to the dimension of the classical repeller. It is a crucial ingredient that the number of "channels" increases with the wavenumber to infinity. However, also in the case where the number of channels is fixed a deviation to Weyl's law is found in quantum graphs where now the prefactor is changed compared to the original Weyl's law. These deviations occur in open graph systems when balanced vertices are present [Dav10, Dav11, Exn11, Lip15, Lawni19]. To investigate this non-Weyl behavior experimentally, microwave networks with variable coupling needed to be introduced.

As an inevitable factor in open systems, loss can be classified into three types, including channel decay, global loss and local loss [Sav06]. It causes resonance overlapping, and an important parameter to quantify it, is the mean modal overlap [Fyo96], which is determined by the average resonance widths and their mean spacing. There are microwave experiments that try to reduce the absorption from the resistance in the walls, such as superconducting microwave billiards [Grä92, Die15]. However, most microwave experiments are performed at room temperature where the losses are not negligible [Kuh05], and in some cases, the absorption from the walls dominates the losses in the system and the resonances show strong overlap [Kuh17]. Due to these experiments, theoretical descriptions have been extended to include losses as an ingredient. A large modal overlap is especially important in reverberation chambers [Hil09] to guarantee sufficient statistically independent spectra allowing for statistical investigation but still having high quality factors to perform electromagnetic compatibility (EMC) testing [Hil09].

Recently, the idea to introduce chaotic reverberation chambers (CRC) for better statistical performance as well as for a better theoretical description based on the effective Hamiltonian idea using RMT was proposed [Gro14a, Gro16]. These reverberation chambers allow to investigate coherent perfect absorption (CPA) [Cho10], a phenomenon describing all coherent incident radiation is perfectly captured by wave interference inside a lossy system. They are inherently related to the zeros of the scattering matrix, more precisely a CPA occurs exactly when a zero is located on the real axis of the complex plane [Fyo17]. CPAs are now proposed for very efficient sensors [Bar17]. An ideal experimental platform to study CPAs [Fra20, Del22],

is a CRC equipped with mechanical stirrers and reconfigurable intelligent surfaces (RIS) [Kai14]. To understand the existence of CPAs in these systems a modeling of the system's loss and effective Hamiltonian is needed to accurately describe the spectral and scattering properties of chaotic system, such as level dynamics of poles and zeros [Kuh13], fluctuation properties of the scattering matrix [Leh95a, Leh95b], and distribution of poles and zeros [Fyo97]. Furthermore, it may be necessary to modify the coupling of the system, and in the case of over-coupling, superradiance [Dic54, Wei21] may occur.

The thesis will be structured as follows: chapter 2 firstly introduces the theoretical description of closed and open wave systems, including Weyl's laws, RMT, scattering theory and effective Hamiltonian approach, as well as poles and zeros of the scattering matrix and superradiance. Then, chapter 3 presents quantum graphs, microwave networks and non-Weyl graphs, and discusses experiments on parametric studies of non-Weyl phenomena in tetrahedral and lasso graphs. Finally, chapter 4 introduces CRC, implements the precise determination of loss before using them to compare the zeros of the scattering matrix close to the real axis, intimately related to CPAs, obtained by the experiment to RMT predictions. Additionally, a discussion of the effects of parametric variation of the system on CPAs is done, confirming that the description needs a superradiant system and those CPAs can be used as sensors, here implemented as a temperature sensor.

Chapter 2

Theoretical Description of Wave Systems

Contents

2.1	Electromagnetic and Matter Waves	6
2.2	Closed Wave Systems	7
2.2.1	<i>Closed Systems: From 1D to 3D</i>	7
2.2.2	<i>Weyl's Law</i>	9
2.2.3	<i>Random Matrix Theory (RMT)</i>	10
2.3	Open Wave Systems	13
2.3.1	<i>Scattering Systems</i>	14
2.3.2	<i>Effective Hamiltonian Approach</i>	16
2.3.3	<i>Poles and Zeros of the Scattering Matrix</i>	17
2.3.4	<i>Fluctuation Properties of the Scattering Matrix</i>	19
2.3.5	<i>Superradiance</i>	21

From one-dimensional network to two- or three-dimensional cavities, there are many wave systems suitable for describing the occurrence of quantum/wave phenomena. Even though they could be quite distinct in their theoretical description, numerical simulation, and experimental realization, sometimes they share the same properties in the eigenvalues of closed wave systems or in the scattering matrix of the corresponding open systems. In this chapter, we will first examine the electromagnetic and matter waves, and discuss three types of closed microwave systems. Then we will introduce Weyl's law and random matrix theory (RMT), as well as methods for describing open system: scattering theory and effective Hamiltonian approach. Finally, we will study poles and zeros of scattering matrix in complex plane, and superradiant state as an extreme wave phenomenon.

2.1 Electromagnetic and Matter Waves

As this thesis mainly concerns microwave experiments, we will first describe the propagation of electromagnetic waves, starting with Maxwell's equations:

$$\vec{\nabla} \cdot \vec{D} = 0, \quad (2.1)$$

$$\vec{\nabla} \cdot \vec{B} = 0, \quad (2.2)$$

$$\vec{\nabla} \times \vec{E} = -\frac{\partial \vec{B}}{\partial t}, \quad (2.3)$$

$$\vec{\nabla} \times \vec{H} = \frac{\partial \vec{D}}{\partial t}. \quad (2.4)$$

Where in vacuum, displacement \vec{D} and induction \vec{B} are related to the electric \vec{E} and magnetizing field \vec{H} , respectively, by:

$$\vec{D} = \epsilon_0 \vec{E}, \quad (2.5)$$

$$\vec{B} = \mu_0 \vec{H}. \quad (2.6)$$

Here, ϵ_0 and μ_0 are permittivity and permeability of the vacuum. Note, that in mediums other than vacuum, relative permittivity and permeability must be introduced, as exemplified in microwave coaxial cables or networks, discussed in subsection 3.2.1. Using vector identity $\vec{\nabla} \times (\vec{\nabla} \times A) = \vec{\nabla}(\vec{\nabla} \cdot A) - \Delta A$, we get the time-dependent wave equations:

$$\Delta \vec{E} - \frac{1}{c^2} \frac{\partial^2 \vec{E}}{\partial t^2} = 0, \quad (2.7)$$

$$\Delta \vec{B} - \frac{1}{c^2} \frac{\partial^2 \vec{B}}{\partial t^2} = 0, \quad (2.8)$$

where c is the speed of light in vacuum. Assuming that the electromagnetic fields oscillate harmonically $e^{-i\omega t}$, we obtain the vector Helmholtz equations:

$$(\Delta + k^2) \vec{\psi} = 0, \quad \vec{\psi} = \vec{E}, \vec{B}, \quad (2.9)$$

where $k = \omega/c$ is the wavenumber and ω is the angular frequency.

In this thesis, we use microwave systems to simulate quantum systems. To establish the relation between these two, we now look at matter wave. It is described by the time-dependent Schrödinger equation:

$$\left[-\frac{\hbar^2}{2m} \Delta + V(\vec{r}) \right] \Psi(\vec{r}, t) - i\hbar \frac{\partial}{\partial t} \Psi(\vec{r}, t) = 0. \quad (2.10)$$

For a free particle ($V = 0$) in a stationary state $\Psi(\vec{r}, t) = \psi(\vec{r}) e^{-iEt/\hbar}$, Eq. (2.10) reduces to scalar Helmholtz equation:

$$(\Delta + k^2)\psi = 0, \quad k = \sqrt{2mE}/\hbar, \quad (2.11)$$

where E is the energy of the system. The quadratic k - E relationship in quantum systems contrasts with the linear k - ω relationship in wave equations due to their differing orders of time derivatives in Eqs. (2.7) and (2.10).

Here, to simplify the discussion appearing later on, we use the form of Helmholtz equation that includes both scalar and vector fields:

$$(\Delta + k^2)\psi = 0, \tag{2.12}$$

where k is the wavenumber and ψ can represent either a scalar field ψ (e.g., pressure, electric potential, wavefunction) or a vector field $\vec{\psi}$ (e.g., electric field, magnetic field).

As discussed in this section, electromagnetic and matter waves propagate freely in space. So far, they are discussed in the context of a given system where specific boundary conditions is applied. In this thesis, particular interest is focused on the fact that the equations describing electromagnetic and matter waves are found to be mathematically equivalent under certain boundary conditions. This equivalence enables the use of microwave systems to simulate quantum systems, a point of great interest, especially within the quantum chaos community. Specifically, to illustrate this equivalence, examples such as the one-dimensional network and two-dimensional cavity will be discussed in the following section 2.2.

2.2 Closed Wave Systems

Closed wave systems are physical environments where waves are confined within finite boundaries, with no coupling to the outside. These systems have different dimensions, shapes, and boundary conditions, leading to a wide variety of solutions to the wave equations. Most importantly, some of these systems are able to simulate corresponding quantum systems. In this section, we will introduce three closed microwave systems, discussing their properties separately. Then we will discuss Weyl's law and RMT, which are useful for analyzing closed systems.

2.2.1 Closed Systems: From 1D to 3D

Here we will investigate three closed microwave systems: one-dimensional networks (also known as graphs), as well as two- and three-dimensional cavities. While only 1D graph and 3D cavity are investigated in this thesis, the description of the 2D cavity is included for completeness.

For the tetrahedral graph shown in table 2.1 (a), the size of the system is determined by the total length of the graph. Waves propagate along the bonds of the graph and can be described by the Eq. (2.12), where k is the wave number and the field ψ represents the potential difference U between the inner and outer conductors' surface of the coaxial cable. The wave amplitude ψ satisfies Neumann boundary condition at a vertex. This configuration leads to the equation describing wave transport in network equivalent to 1D Schrödinger equation, thus microwave networks can be used to simulate quantum graphs [Lawni10]. Scientists also have found that spectral statistics of these systems closely following prediction of RMT,

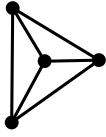
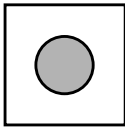
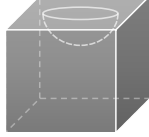
	Tetrahedral graph	Sinai billiard	Reverberation chamber
	(a) 	(b) 	(c) 
Dim:	1	2	3
Size:	Length	Area	Volume
ψ :	U	E_z	\vec{E} or \vec{B}
BC:	Neumann	Dirichlet	Mixed

Table 2.1: Sketches of three types of systems: (a) 1D microwave graph, (b) 2D microwave billiard, (c) 3D microwave cavity. Dim denotes “Dimension” and BC indicates “Boundary Conditions”.

if the network is sufficiently complex. Thus this model is widely used in the quantum chaos community [Lawni10, Lu20, Stö22]. For more detailed explanations of the quantum graph and microwave network, see chapter 3.

The Sinai billiard [Sin63, Sri91] in table 2.1 (b), named after Yakov Sinai, is a 2D billiard system, where waves propagate within a square with a circular obstacle, and its size is determined by the area. This can be experimentally realized within cylindrical microwave cavities, i.e., whose shape is translationally invariant in the z direction, and closed by top and bottom plates which are perpendicular to z , and are separated by h . In these cavities, only TM_0 modes can be excited if the excitation frequency is below $f_{\max} = c/2h$ [Stö99], where c is the speed of light. In this case, the electric field vector is always perpendicular to the bottom and top plates of the cavity, and E_z satisfies the Dirichlet boundary conditions on the outer circumference of the 2D cavity. Under these conditions, Helmholtz Eq. (2.9) becomes scalar (wave amplitude ψ corresponds to E_z), which is equivalent to the Schrödinger equation describing 2D quantum billiard system. Thus, 2D chaotic billiard is well-known in the study of quantum chaos research, alongside another common example being the Bunimovich Stadium [Bun79, Stö90]. Note that the 2D billiard will not be studied in this thesis, we show it here because it is the one of the most classical example in the field of quantum chaos or wave chaos. As well as in subsection 2.3.1, we will use 2D billiard as a tutorial to help the reader better understand how to describe a scattering system.

The reverberation chamber (RC) [Bes11] shown in table 2.1 (c) is a 3D electromagnetic cavity where the size is determined by the volume of the chamber, with a scatterer located at the top surface. In this case, we need the vector Helmholtz equation to describe the propagation of waves within the chamber, where k is the wave number and the field $\vec{\psi}$ represents the electric \vec{E} or the magnetic field \vec{B} . The chamber’s walls are modeled as perfect electric conductors (PEC), meaning the tan-

gential component of the electric field \vec{E} is zero on the surface $\vec{E}_{\text{tan}} = 0$, and the normal component of the magnetic field \vec{B} is zero on the surface $\vec{B}_{\text{n}} = 0$. This RC is chaotic, thus displaying spectral and spatial properties described by RMT already at reasonably low frequencies [Gro14c]. This makes them important tools in the study of wave chaos, even though there is no direct analogy between the vector Helmholtz equation and the scalar Schrödinger equation (since \vec{E} and \vec{B} in Helmholtz equation are not independent). In chapter 4, we will discuss RC in more detail and treat it as a 3D chaotic cavity to study its scattering phenomena.

The tetrahedral graph, Sinai billiard, and RC are examples of microwave systems spanning one to three dimensions that often used to reveal universal spectral statistics. Beyond microwave, other platforms such as acoustics [Mor93], optics [Doy01] also exhibit these characteristics. Despite variations in their geometry, boundary conditions, or platforms, these systems all display unique discrete energy spectra. Weyl's law and RMT are effective in analyzing these behaviors, providing fundamental insights into the density of states of eigenvalues and spectra statistics of wave systems. We discuss them in subsections 2.2.2 and 2.2.3. Additionally, in real experimental environments, these closed systems must be transformed into open systems. This transformation endows them with scattering properties and thus exhibits universal features and potentially unexpected wave phenomena, which will be explored in section 2.3.

2.2.2 Weyl's Law

Weyl's law, originally formulated by Hermann Weyl in 1911, was initially developed to explain black body radiation, particularly for understanding the density of states of a system based on its geometrical parameters [Wey12a, Wey12b, Wey12c]. It counts the number of eigenvalues smaller than the energy $E = k^2$ in quantum systems, or in general wave systems smaller than a wave number k , in average. In d -dimensional systems with a bounded domain Ω it is given by:

$$N(k) = \frac{\text{Vol}(\Omega)}{(2\pi)^d} \omega_d k^d + O(k^{d-1}), \quad (2.13)$$

where $\text{Vol}(\Omega)$ is the volume of the domain Ω , and ω_d is the volume of the unit ball in \mathbb{R}^d . For $d = 1, 2, 3$, the volumes are given by $\omega_1 = 2$, $\omega_2 = \pi$, and $\omega_3 = 4\pi/3$.

This formula indicates that once we determine the geometric parameters of the system, we can predict the number of eigenvalues within a certain range of k . For example, in 1D closed graph system, knowing its total length L allows us to estimate the number of eigenvalues below a specific wave number:

$$N^{1\text{D}}(k) = \frac{L}{\pi} k + O(1), \quad (2.14)$$

where $O(1)$ is defined by the number of the vertices and boundary condition [Gnu06]. Similarly, for a 2D microwave cavity, the prediction becomes

$$N^{2\text{D}}(k) = \frac{A}{4\pi} k^2 + \frac{C}{4\pi} k + O(1), \quad (2.15)$$

where A and C are the area and perimeter of the billiard, and $O(1)$ depends on the curvature and the corners in the system [Bal71]. In the case of a 3D (vectorial) electromagnetic case and for perfectly conducting boundary conditions, Weyl's law is given by

$$N^{3D}(f) = \frac{8\pi V}{3c^3} f^3 + (b_{\text{curv}} + b_{\text{edges}})f + \text{const}, \quad (2.16)$$

where V is the volume of the cavity, c is the speed of light, and b_{curv} and b_{edges} includes contributions from the curvature of the boundary and edge corrections. The constant term is related to the geometric properties of the system. Here we use the frequency $f = ck/2\pi$ to remain consistent with the Ref. [Gro14c], and detailed expressions for the second terms also could be found. Note that in the 3D case, there is no term proportional to f^2 because the different contributions of both polarisations TE and TM mutually cancel out [Bal77].

Moreover, Weyl's law has been found to hold in systems that are strongly disordered, demonstrating its robustness across different types of physical environments [Pie14, Sav17]. Specifically, it has been shown that the mean length between two consecutive bounces of a typical trajectory traversing a system depends only on the size of the system and of its boundary, which are both independent of the specific structure of the underlying medium. This robustness highlights the fundamental nature of Weyl's law in describing the average properties of wave systems regardless of the underlying physical conditions or specific details of the disorder, which holds significant potential for practical applications.

When the system is gradually opened, new features emerge. In addition to counting eigenvalues, known as Bound States in the Continuum (BICs) [Hsu16] in this case, one must also account for resonances. The concept of volume becomes ambiguous as the system couples to an external environment. For weak coupling, Weyl's law remains effective as long as the resonances develop only a small width. However, with stronger coupling to the external environment, phenomena such as the fractal Weyl law for chaotic systems appear, where the dimension d is no longer purely spatial but instead relates to the dimension of the classical repeller within the system [Zwo89, Non05, Kop10]. Experimental studies have demonstrated these effects, showcasing the transition from closed to open systems and the resulting changes in resonance behavior [Lu03, Pot12].

Despite the robustness of Weyl's law in many contexts, there are special situations where non-Weyl behavior is observed [Dav10, Dav11, Exn11, Lip15, Lawni19], namely with a modified prefactor. Specifically, these deviations occur in graph systems, and the transition from a Weyl graph to a non-Weyl graph occurs when a balanced vertex is introduced. A vertex is called balanced if the number of leads attached to it equals the number of internal edges meeting at that vertex. It is important to study these non-Weyl behaviors in order to better understand Weyl's law, and we will discuss it in detail in chapter 3.

2.2.3 Random Matrix Theory (RMT)

RMT was developed by Eugene Wigner in the 1950s to model the energy levels of complex atomic nuclei. The field significantly developed over the following decades

through contributions from Wigner, Dyson, Mehta and others [Wig55, Dys62, Meh91, Haa18]. In particular, Dyson introduced the classification of random matrices into different symmetry classes based on their invariance properties under orthogonal, unitary, and symplectic transformations. This classification helped in understanding the universal statistical properties of complex systems. Later, the theory experienced a significant resurgence in the 1980s due to the groundbreaking work of Bohigas, Giannoni, Schmit (BGS) and Casati, who conjectured that RMT could be applied to the study of spectra in chaotic systems [Cas80, Boh84], broadening its relevance and impact across various fields of physics.

In RMT, the Hamiltonian of a system is represented by an $N \times N$ matrix H , where the elements H_{nm} are randomly distributed, typically following a Gaussian distribution. These elements depend on the symmetries of the physical system. A key requirement is the Hermiticity of the Hamiltonian, expressed as $H_{mn} = H_{nm}^*$. Another important symmetry is time-reversal symmetry (TRS), represented by a time-reversal operator T . For the system with TRS, $HT = TH$.

In time-reversal invariant systems without half-integer spin, all matrix elements of the Hamiltonian are real and the time-reversal operator satisfies $T^2 = 1$. If these elements are uncorrelated and Gaussian distributed, the matrix belongs to the Gaussian orthogonal ensemble (GOE). This ensemble is extensively studied [Stö99, Haa18] and is most relevant to this thesis, such as the chaotic graph and cavity. For completeness, we also present two other common ensembles in RMT. When TRS is broken, the matrix elements become complex, resulting in the Gaussian unitary ensemble (GUE). In systems with half-integer spin, where the time-reversal operator satisfies $T^2 = -1$, it leads to the Gaussian symplectic ensemble (GSE). Numerous studies have explored both the unitary [Bia16, Reh18, Lu20, Stö22] and the symplectic one [Reh16, Lu20, Che21a, Stö22, Ma24]. Later the classical ensembles had been extended to ten-fold way, see the work of Altland and Zirnbauer [Alt97].

In RMT, for a direct comparison with experiments, where usually only the eigenfrequencies are accessible, it is essential to derive the distribution of the eigenenergies of the Gaussian ensembles. The joint probability distribution of the eigenvalues E_n is of practical interest and can be expressed in a single formula [Meh91]

$$P(E_1, \dots, E_n) \sim \prod_{n>m} (E_n - E_m)^\beta \exp\left(-A \sum_n E_n^2\right), \quad (2.17)$$

where β is the universality index, taking values 1, 2 and 4 for GOE, GUE, and GSE, respectively. The constant A is a normalization factor. The correlated energy distribution function contains all relevant information on the Gaussian ensembles. However, this joint probability distribution lacks of accessibility to compare to numerical or experimental findings.

To explore this further, we consider the density of states, an important spectral property in RMT. In the case of the Gaussian ensembles, we are interested in its average over the complete ensemble

$$\langle \rho(E) \rangle = \left\langle \sum_n \delta(E - E_n) \right\rangle. \quad (2.18)$$

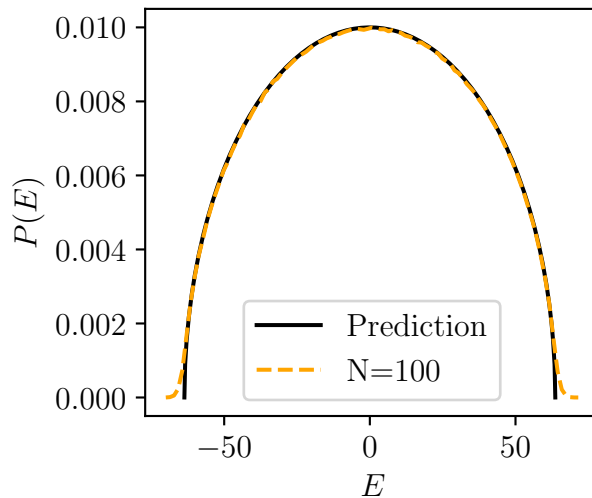


Figure 2.1: Numerical examples of probability density function of GOE random matrices, where $N = 100$ and it is averaged over 10^5 realizations.

There are several ways to calculate this quantity, such as starting from Eq. (2.17) or using supersymmetry techniques. Here, we will not delve into the detailed derivation, as these details can be found in the literature, such as Mehta's book [Meh91]. Instead, we will present the results for these matrix ensembles. When analyzing the ensemble-averaged density of states, it is observed that, in the limit $E \rightarrow 0$ the density becomes constant, and also $N \rightarrow \infty$ is typically performed thus extending this range to infinity. It is common practice to normalize the density to one ($\rho(0) = 1$), thus giving:

$$\langle \rho(E) \rangle = \begin{cases} \sqrt{1 - \left(\frac{\pi E}{2N}\right)^2}, & |E| < \frac{2N}{\pi}, \\ 0, & |E| > \frac{2N}{\pi}. \end{cases} \quad (2.19)$$

This is known as Wigner's semicircle law. As shown in Fig. 2.1, we illustrate the probability density function $P(E) = \langle \rho(E) \rangle / N$ of the GOE random matrices from the numerical simulation. In the function, the size of the Hamiltonian N is included to ensure that the integral of the probability density function over all possible energy values equals one. Note, that there is a small tail outside $2N/\pi$ due to the finite size of Hamiltonian.

Among various spectral correlations in RMT, the nearest neighbor spacing distribution stands out as one of the most extensively studied one, as it is easily accessible once the spectra are numerically or experimentally extracted. It can be calculated from the correlated eigenenergy distribution of Gaussian ensembles in Eq. (2.17) by:

$$p(s) = \int_{-\infty}^{\infty} dE_1 \int_{-\infty}^{\infty} dE_2 P(E_1, E_2) \delta(s - |E_1 - E_2|), \quad (2.20)$$

where s is the level spacing and the distribution is determined by two normalization conditions. The first one normalizes the total probability to one $\int_0^{\infty} p(s) ds = 1$, and

the second normalizes the mean level spacing $\int_0^\infty sp(s)ds = 1$. The integrals yield

$$p(s) = \frac{\pi}{2} s e^{-\frac{\pi}{4} s^2}. \quad (2.21)$$

This is the Wigner distribution for the GOE case, and it is particularly relevant for the microwave systems introduced in this thesis. Additionally, there are analytical predictions for the other two ensembles, GUE and GSE. Other spectral correlations, such as the integrated spacing distribution, two-point correlation function, number variance, and spectral rigidity, are also commonly studied [Stö99, Haa18].

With the intensive study of the universal statistical behavior of eigenenergies, it has been found that the dynamics of energy levels can also be an important subject of investigation. Consider a chaotic system that varies with a parameter X , the velocity of the eigenvalues $E_i(X)$ can be calculated as

$$v_{X,i} = \frac{\partial E_i(X)}{\partial X}, \quad (2.22)$$

and once normalized,

$$v_i = \frac{v_{X,i}}{\sigma_X}, \quad \sigma_X^2 = \frac{1}{n} \sum_{j=1}^n (v_{X,i} - \langle v_{X,i} \rangle)^2, \quad (2.23)$$

the velocities should be Gaussian distributed with a variance of unity, independent of the universality class, if the perturbation is global, i.e., has the same rank as the Hamiltonian [Bar99]. This statistical behavior of the velocities is examined in detail in chapter 4. Other correlations used in the study of level dynamics include the avoided-crossing distribution [Zak91, Zak93b], curvature distribution [Zak93a] or velocity-correlation function [Sim93].

While RMT provides a robust framework for understanding the statistical properties of closed chaotic systems, its applicability extends to open systems as well. In open systems, energy levels become resonances with finite lifetimes, and the corresponding Hamiltonians are no longer Hermitian. This leads to the study of complex eigenvalues, where both the real and imaginary parts provide valuable information about the system. In the next section, I'll provide a detailed introduction to open wave systems, exploring their unique properties.

2.3 Open Wave Systems

Open wave systems are crucial in real-world situations, as measurements inevitably cause disturbances in closed systems. A mathematical framework to manage the interaction between these systems and their external environment is scattering theory [Ver85, Sok92]. In this section, we will first introduce scattering systems, including commonly used concepts such as the scattering matrix. Next, we will discuss the effective Hamiltonian approach, a powerful tool that can be used to establish the relationship between closed and open systems. Finally, we will explore poles and zeros of the scattering matrix, their behavior described by RMT, and specific

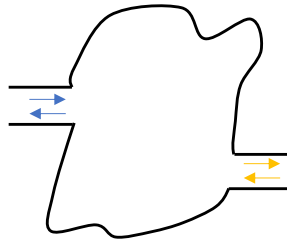


Figure 2.2: Sketch of a scattering system with two attached channels.

phenomena such as superradiance.

2.3.1 Scattering Systems

Scattering theory, originally developed in nuclear physics [Mah69, Lew91], provides a fundamental framework for understanding the wave behavior in different media. A central concept in this theory is the scattering matrix, which encapsulates all the information about how incoming waves are transformed into outgoing waves after interacting with a system.

To illustrate this, we take a straightforward and intuitive example of a 2D microwave billiard of arbitrary shape, coupled via waveguides as shown in Fig. 2.2, providing an accessible introduction as a scattering system and to the principles of scattering theory.

The amplitude of the field, denoted by $\psi(\mathbf{r}, k)$, satisfies the Helmholtz Eq. (2.12). When the widths of the waveguides are small comparable to the wavelength, and the waveguide supports only one mode, the number of channels is exactly equal to the number of waveguides. In this case, the electromagnetic field within the i -th waveguide can be described as a combination of one incoming wave and one outgoing wave

$$\psi(\mathbf{r}, k) = a_i e^{ik(\mathbf{r}-\mathbf{r}_i)} - b_i e^{-ik(\mathbf{r}-\mathbf{r}_i)}, \quad (2.24)$$

where \mathbf{r}_i is the point of entrance of the i -th waveguide, k is the wavenumber, a_i and b_i are the amplitudes that describing how waves are entering and leaving the billiard. In this section bold variables are used for vectors. Since the width of the waveguide is small compared to the wavelength, each waveguide can be assumed as one scattering channel, and the scattering matrix S reduces to an $M \times M$ matrix, where M is the number of waveguides. Assuming the amplitude vector of the waves entering or leaving the billiard by $\mathbf{a} = (a_1, a_2, \dots, a_M)$ and $\mathbf{b} = (b_1, b_2, \dots, b_M)$, the scattering matrix of the billiard is defined by

$$S\mathbf{a} = \mathbf{b}. \quad (2.25)$$

The diagonal elements S_{ii} of S correspond to the reflection as they describe the scattering back inside the port, whereas the nondiagonal elements S_{ij} are the transmission amplitudes describing the transport between different ports. For the scattering

matrix of the system in Fig. 2.2, it is

$$S = \begin{pmatrix} S_{11} & S_{12} \\ S_{21} & S_{22} \end{pmatrix}. \quad (2.26)$$

The quantities $|S_{11}|^2$ and $|S_{22}|^2$ represent the reflectance at port 1 and port 2, respectively. The transmittance from port 1 to port 2 is conventionally given by $|S_{21}|^2$, from port 2 to port 1 given by $|S_{12}|^2$. As reciprocity holds in our system: $S_{21} = S_{12}^*$. It is worth mentioning that reciprocity and time-reversal symmetry are different [Sig22]. Time-reversal symmetry refers to the Hamiltonian of the closed system, while reciprocity pertains to the scattering properties here. Some systems have scattering reciprocity without time-reversal symmetry in their Hamiltonian. In this thesis, we study systems where both reciprocity and time-reversal symmetry are preserved.

Next, we explore the relationship between the Green function and the scattering matrix. Starting from the system with Dirichlet boundary conditions, see the black lines of the Fig. 2.2, at the opening of the leads, we assume Neumann boundary conditions for the corresponding closed system. The system has a discrete spectrum of eigenvalues \bar{k}_n and corresponding real eigenfunctions $\bar{\Psi}_n$. The resulting Green function $\bar{G}(\mathbf{r}, \mathbf{r}', k)$ is defined as:

$$\bar{G}(\mathbf{r}, \mathbf{r}', k) = \sum_n \frac{\bar{\Psi}_n(\mathbf{r})\bar{\Psi}_n(\mathbf{r}')}{k^2 - \bar{k}_n^2}. \quad (2.27)$$

In this case, we assume for simplicity a point-like coupling, leading to the description in terms of the wavefunctions $\bar{\Psi}_n(\mathbf{r})$ at the openings. Without going into the detailed derivation, the relationship between the scattering matrix S and the Green function \bar{G} is given by [Stö99]

$$S = \frac{\mathbb{I} - \frac{i}{2}\kappa\bar{G}}{\mathbb{I} + \frac{i}{2}\kappa\bar{G}}, \quad (2.28)$$

where κ describes the coupling of the waveguides to the billiard, which has been assumed to be equal for all waveguides. The unitarity of S can be seen from this expression. By applying a perturbative approximation, particularly under the condition that the resonances are isolated, we can derive the following expression:

$$S_{ij} = \delta_{ij} - i\kappa \sum_n \frac{\bar{\Psi}_n(\mathbf{r}_i)\bar{\Psi}_n(\mathbf{r}_j)}{k^2 - \bar{k}_n^2 + i\Gamma_n/2}, \quad (2.29)$$

where δ_{ij} denotes the Kronecker delta, Γ_n accounts for losses such as the opening of the system by waveguides or antennas. This indicates that in open systems, we no longer obtain the wavefunctions Ψ_n for closed system, and the resonances are shifted to \bar{k}_n^2 with a broadened part Γ_n . This equation is the billiard equivalent of Breit-Wigner-formula in the context of nuclear physics [Bla52].

Eq. (2.29) is valid when the eigenvalues \bar{k}_n are well separated, leading to spectra that are combinations of Lorentzian-shaped resonances with amplitudes $\bar{\Psi}_n(\mathbf{r}_i)\bar{\Psi}_n(\mathbf{r}_j)$. In scenarios where the resonances overlap significantly, it becomes challenging to in-

interpret $\bar{\Psi}_n(\mathbf{r})$ as the wavefunctions of a closed system. Nonetheless, the spectrum S_{ij} still manifests as a superposition of Lorentzian resonances, provided that global absorption and antenna couplings remain uniform across the individual Lorentz lines.

The example in this subsection is particularly effective due to its straightforward physical interpretation, resembling a simplified billiard model. However, this approach relies on a simplifying approximation and fails to capture more complex scenarios where resonances overlap. In the following subsection, we will introduce a more comprehensive method that covers overlapping resonances and enhances our understanding of the system's scattering behavior, moving beyond the simpler approximations used here.

2.3.2 Effective Hamiltonian Approach

As previously noted, the Breit-Wigner formula is effective for isolated resonances but proves insufficient for broader resonances that overlap significantly with each other. This limitation leads us to adopt the effective Hamiltonian approach, which offers a robust framework for handling such overlapping resonances. Initially developed in nuclear physics [Mah69, Ver85, Sok89], this approach has been successfully applied to various open systems, including wave billiards [Stö99, Fyo97, Dit00]. We begin with a fundamental formula for the scattering matrix:

$$S = \frac{\mathbb{I} - iK}{\mathbb{I} + iK}, \quad (2.30)$$

where K is the Wigner reaction matrix

$$K = \frac{1}{2}W^\dagger(E - H_0)^{-1}W. \quad (2.31)$$

Here, H_0 denotes the Hermitian $N \times N$ Hamiltonian of the unperturbed system, giving rise to N real energy levels. These levels are coupled to M continuum channels via the $N \times M$ matrix W . If the system is chaotic, then H_0 can be replaced by a random $N \times N$ matrix in GOE. The constraints on the elements of H_0 are described in detail in subsection 2.3.4. For W , its element w_{nm} describes the coupling strength between n -th resonance and m -th channel. An important parameter often used later, the coupling strength κ , is actually related to w_{nm} , which will be discussed in subsection 2.3.4. For point-like couplings, as the billiard models in previous subsection, two equations here will simplify to Eq. (2.28), since w_{nm} is proportional to $\psi_n(r_m)$ at the coupling point r_m for the m -th channel.

An alternative expression for the scattering matrix is:

$$S = \mathbb{I} - iW^\dagger \frac{1}{E - H_{\text{eff}}} W, \quad (2.32)$$

where the effective Hamiltonian characterizes the open system

$$H_{\text{eff}} = H_0 - \frac{i}{2}WW^\dagger. \quad (2.33)$$

Since one is always interested in the singularities and zeros of scattering matrix, we will take determinant for scattering matrix. By using the identity $\det(\mathbb{I} - PQ) = \det(\mathbb{I} - QP)$, one can find:

$$\begin{aligned}
 \det S &= \det\left(\mathbb{I} - iW^\dagger \frac{1}{E - H_0 + \frac{i}{2}WW^\dagger} W\right) \\
 &= \det\left(\mathbb{I} - iWW^\dagger \frac{1}{E - H_0 + \frac{i}{2}WW^\dagger}\right) \\
 &= \frac{\det\left(E - H_0 - \frac{i}{2}WW^\dagger\right)}{\det\left(E - H_0 + \frac{i}{2}WW^\dagger\right)} \\
 &= \frac{\det\left(E - \tilde{H}_{\text{eff}}\right)}{\det\left(E - H_{\text{eff}}\right)} = \prod_{n=1}^N \frac{E - z_n}{E - \mathcal{E}_n},
 \end{aligned} \tag{2.34}$$

where \tilde{H}_{eff} is essentially H_{eff} with a flipped sign on the imaginary part:

$$\tilde{H}_{\text{eff}} = H_0 + \frac{i}{2}WW^\dagger. \tag{2.35}$$

This configuration illustrates that the complex eigenvalues of H_{eff} and \tilde{H}_{eff}

$$\begin{aligned}
 \mathcal{E}_n &= E_n - \frac{i}{2}\Gamma_n, \\
 z_n &= E_n + \frac{i}{2}\Gamma_n
 \end{aligned} \tag{2.36}$$

correspond to the poles and zeros of the scattering matrix, with eigen-energies E_n and positive widths Γ_n . The detailed discussion on poles and zeros will be further explored in the following subsection 2.3.3.

The coupling amplitudes are assumed to be energy independent within the relevant energy range. In the general case, elements of the matrix W are complex, as discussed in reference [Kö10], particularly when considering the coupling to a variable antenna. For our purposes of this thesis, we consider only a real W matrix.

Since here we assume there is neither gain nor loss in the system, the scattering matrix S is unitary. However, in practical scenarios, losses are inevitable. We will discuss how to formulate the scattering matrix to account for losses in subsection 4.1.2, providing a more realistic description of experimental setups.

2.3.3 Poles and Zeros of the Scattering Matrix

Beyond the effective Hamiltonian discussed in the previous subsection, which explains the interactions between closed systems and external environments, the poles and zeros of the scattering matrix are also crucial for a thorough analysis of scattering processes. The behavior of the scattering matrix is captured by Eq. (2.34), which is a representation of the Weierstrass factorization theorem [Gri13, Kra19]. It illustrates that the behavior of the scattering matrix is completely determined by the locations of its poles and zeros. Understanding this straightforward framework

helps clarify complex phenomena and is vital for furthering our knowledge of wave interactions. This subsection will focus on detailing the specific roles of poles and zeros in scattering phenomena.

Poles of the scattering matrix, \mathcal{E}_n , are also commonly referred to as resonances. The real part of these poles corresponds to the eigenenergy E_n of the resonance, while the imaginary part describes their width Γ_n , indicating exponential decay of the intensity of the n -th eigenstate in the time domain. Exploring these poles also uncovers unexpected phenomena. One particular example is the appearance of exceptional points (EPs), where multiple poles converge in the complex plane, while the corresponding eigenfunctions coalesce. These EPs introduce radical changes in the systems behavior, such as sensitivity enhancements and unusual wave propagation patterns [Dem01, Pen14, Dop16, Özd19, Kra19].

The statistical characteristics of resonances in open chaotic systems have received significant attention, much like the energy-level statistics in closed chaotic systems. The bulk of research has concentrated on scenarios where effective coupling is weak, characterized by the mean resonance width being smaller than the mean level spacing, as depicted by $\langle \Gamma \rangle / \Delta \ll 1$. In such conditions, resonances remain well-separated, facilitating the application of simple first-order perturbation theory. This separation allows for a straightforward application of the Breit-Wigner formula (2.29), simplifying the process of extracting individual resonances. While if the effective coupling is strong, it may introduce a phenomenon called superradiance, where certain resonances aligned with the system's channels, become dominant and significantly impact the system, as detailed in subsection 2.3.5.

When the ratio of the average width of the resonances to the mean level spacing is much greater than one $\langle \Gamma \rangle / \Delta \gg 1$, it complicates the extraction of the resonances. Traditional techniques such as direct curve-fitting are no longer suitable. Instead, methods like harmonic inversion [Mai99] have been developed to effectively extract resonances from a spectrum where the ratio is up to a few times [Kuh08], with the results aligning well with RMT predictions. In this thesis, we will study poles and zeros in the overlapping regime, and since this section focuses more on the case of unitary scattering matrices, we will discuss it in chapter 4.

Zeros of the scattering matrix, z_n , represent the specific energy levels at which the scattering amplitude becomes zero, indicating points where the system exhibits minimal scattering cross-section. In the case of systems without gain or loss, the scattering matrix is unitary, thus all zeros and poles are symmetrically positioned in the upper and lower halves of the complex energy plane, demonstrating $z_n = \mathcal{E}_n^*$, as illustrated in Eq. (2.36) and Fig. 2.3.

Historically, zeros were often overlooked despite their symmetry with poles. However, the emergence of coherent perfect absorption (CPA), a phenomenon only occurring for non-unitary matrices, has motivated recent studies [Fyo17, Fyo19, Osm20, Kan21, Che20, Che21c] to reevaluate the importance of zeros in the scattering matrix. A critical factor in this reevaluation is the role of loss. CPAs demonstrate that even weakly lossy systems can act as perfect traps for coherent incident radiation through wave interference effects. With the introduction of loss, as previously discussed, the effective Hamiltonian needs to be reformulated to accurately describe the scattering matrix. Consequently, this leads to modifications in both the zeros and poles

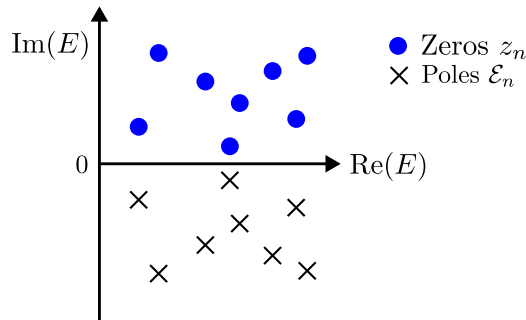


Figure 2.3: Sketch of the zeros and poles of a unitary scattering matrix in the complex plane.

accordingly. Discussions on the role of loss are further detailed in subsection 4.1.2, while the concept of CPA is explored more extensively in subsection 4.1.3.

Expanding upon this groundwork, recent theoretical studies have concentrated on analyzing the zeros of the scattering matrix in chaotic system with uniform [Li17] and non-uniform [Fyo17, Fyo19] losses, and where time-reversal symmetry is preserved or broken. These explorations aim to further capitalize on these complex interference and provide universal predictions for the properties of chaotic CPA cavities. However, experimental investigations into the zeros and their statistical distributions are still limited. This thesis aims to bridge this gap, with detailed discussions and findings presented in chapter 4.

2.3.4 Fluctuation Properties of the Scattering Matrix

Just as the eigenvalue correlations in closed chaotic systems provide deep insights into their dynamics, analyzing the scattering matrix in open chaotic systems can reveal important characteristics. Here we study the ensemble-averaged scattering matrix within the framework of the stochastic approach, which demands a statistical consideration. First, we define the Hermitian part H_0 of the effective Hamiltonian H_{eff} , as it belongs to the GOE, its elements H_{nm} following

$$\langle H_{nm} \rangle = 0, \quad \langle H_{nm} H_{n'm'} \rangle = \frac{\lambda^2}{N} (\delta_{nn'} \delta_{mm'} + \delta_{nm'} \delta_{mn'}). \quad (2.37)$$

The eigenvalues of H_0 lie in the interval $[-2\lambda, 2\lambda]$ with the density given by Wigner's semicircle law, where in this thesis we have especially chosen

$$\lambda = \frac{N}{\pi}, \quad (2.38)$$

yielding a unit level spacing at $E = 0$, see Eq. (2.19). Next, we specify the properties of the coupling amplitudes w_{nm} . These amplitudes are real and drawn from Gaussian distribution with the following properties [Sok88, Sok89]:

$$\langle w_{nm} \rangle = 0, \quad \langle w_{nm} w_{n'm'} \rangle = \frac{2\kappa\Delta}{\pi} \delta_{mm'} \delta_{nn'}, \quad (2.39)$$

where κ is the coupling parameter, assumed to be equal for all channels, and $\Delta = 1$ indicates the unit level spacing. In this thesis, κ is included in the product of $w_{nm}w_{n'm'}$, whereas in some other references, κ is treated separately. One can show that the average diagonal elements of the scattering matrix are given by the following expression:

$$\langle S_{aa} \rangle = \frac{1 - \kappa g(E)}{1 + \kappa g(E)}, \quad (2.40)$$

and $g(E)$ is given by [Leh95a, Leh95b]

$$g(E) - \frac{1}{g(E)} + \frac{m\kappa}{1 + \kappa g(E)} - i\frac{E}{\lambda} = 0, \quad (2.41)$$

with

$$m = \frac{M}{N}. \quad (2.42)$$

Note that the calculation of $g(E)$ is performed in the limit $N \rightarrow \infty$, $M \rightarrow \infty$, and $m < 1$ [Leh95a]. The amplitudes may be chosen as fixed orthogonal vectors [Ver85] or independent Gaussian-distributed random vectors [Sok92] and enter final expressions of $g(E)$. In this thesis, w_{nm} are chosen from a Gaussian distribution respecting Eq. (2.39).

In experimental settings, the transmission coefficient T_a is often the directly measurable quantity, which makes it crucial for characterizing the coupling strength to continua. We define T_a via the real transmission coefficients as follows:

$$T_a = 1 - |\langle S_{aa} \rangle|^2, \quad (2.43)$$

where T_a ranges from 0 to 1, when $T_a \ll 1$ means weak coupling and $T_a = 1$ indicates perfect coupling. The subindex a will be used to denote the number of the channels. A common way is to express T_a at $E = 0$:

$$T_a = \frac{4\kappa_{\text{eff}}}{(1 + \kappa_{\text{eff}})^2}, \quad (2.44)$$

where the ‘‘effective’’ coupling constant is

$$\kappa_{\text{eff}} = \kappa g(0). \quad (2.45)$$

Subsequently, κ can be explicitly related to κ_{eff} by

$$\kappa = \kappa_{\text{eff}} \left[\frac{1 + \kappa_{\text{eff}}}{1 + (1 - m)\kappa_{\text{eff}}} \right]^{1/2}, \quad (2.46)$$

where we obtain $\kappa = \kappa_{\text{eff}}$ when $m \rightarrow 0$, corresponding to $N \rightarrow \infty$ for finite M . In Eq. (2.44), we can see that if one substitutes $1/\kappa_{\text{eff}}$ for κ_{eff} , one gets the same T_a . In other words, T_a induces two coupling parameters, one is under-coupled ($\kappa_{\text{eff}} < 1$), and the other is over-coupled ($1/\kappa_{\text{eff}} > 1$). Note, that this holds for κ_{eff} , not necessarily for κ .

In the analysis, we choose $E = 0$ since the semicircle law guarantees the energy

level density is normalized to 1 near $E = 0$, see Eq. (2.19). This aligns with standard experimental unfolding procedures that normalize spectral density uniformly across frequency, for a direct comparison between experimental findings and theoretical predictions.

In fact, the introduction of κ_{eff} simplifies the determination of experimental coupling, since most previous studies have assumed that the Hamiltonian corresponding to their experimental system is infinite. Under these assumptions, κ_{eff} can be equivalently viewed as κ . However, one should be careful when dealing with systems with global losses (as discussed in subsection 4.1.2), where the relationship (2.46) no longer applies and the loss parameters come into play. Therefore, when the system has global losses, we need to study the coupling parameter κ , as it directly describes the coupling of the effective Hamiltonian, and this topic will be further discussed in the subsection 4.3.1.

2.3.5 Superradiance

Superradiance, initially described by Dicke, occurs when a radiating gas behaves as a single quantum-mechanical system, leading to spontaneous emission of coherent radiation from correlated molecular energy levels [Dic54]. This results in a redistribution of energy states, significantly altering scattering cross-sections. Observations of superradiance span gases [Skr73], plasmas [Xia12], semiconductors [Lim04], Bose-Einstein condensates [Ino99], quantum dots [Sch07], and cold atoms [Ara16].

Apart superradiance has been described by Dicke in the fields of optics, cold atomic systems, and so on. It also appears in systems with RMT as a background, such as microwave networks [Lu24] and microwave billiards [Stö22]. In particular, the phenomenon of resonance trapping [Per00, Stö02] arises in strongly open quantum systems, where in the limit of strong coupling some resonance states align with the channel and others return to the real axis and are trapped. The aligned states are referred to as channel, doorway or superradiant states [Per99, Vol03, Guh09, Aue11, Wei21], others remain long-lived, known as subradiant.

This behavior can be explained through the effective Hamiltonian (2.33), which provides a robust framework. In the following, we will show how the distribution manifest under two distinct limits of coupling strength. If H_0 is from GOE and in the limit of small coupling strengths, the poles are described by perturbation theory

$$\begin{aligned} \mathcal{E}_n &= \mathcal{E}_n^0 - \frac{i}{2}(WW^\dagger)_{nn} \\ &= \mathcal{E}_n^0 - \frac{i}{2} \sum_m |w_{nm}|^2. \end{aligned} \tag{2.47}$$

Due to the small magnitudes of the w_{nm} , all the poles lie close to the real axis.

In the limit of large coupling strengths, H_{eff} is substantially influenced by the term $-\frac{i}{2}WW^\dagger$. This scenario requires choosing a basis in which this term is diagonalized, while treating H_0 as a perturbation. Assuming, for simplicity, the existence of M mutually orthogonal vectors $v_m = w_m/|w_m|$ with normalized components, and $N - M$ additional normalized vectors u_α , which are eigenvectors of H_0 within the reduced subspace and orthogonal to all w_m . Using these basis vectors, the eigenvalues

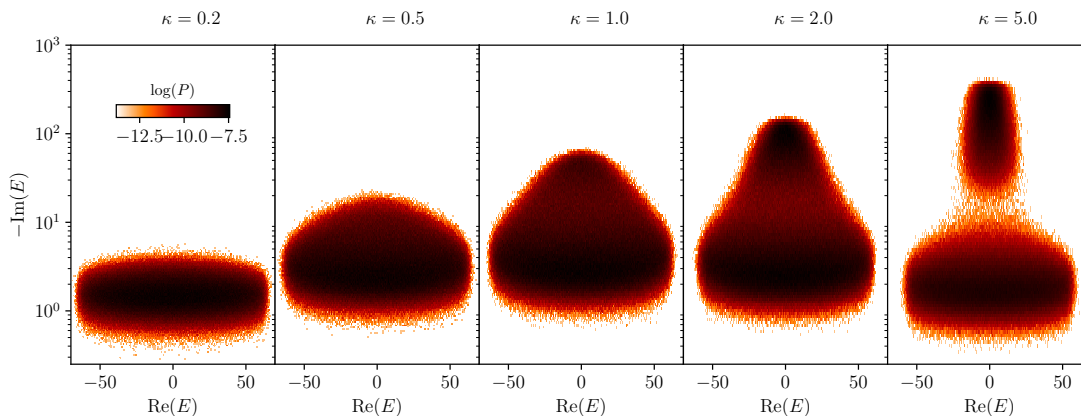


Figure 2.4: Clouds of poles in the complex plane with $M/N = 0.25$ for five different coupling strengths κ . The imaginary part is displayed in log scale. This figure is inspired by [Leh95a].

of H_{eff} are determined as follows:

$$\mathcal{E}_n = \begin{cases} v_n^\dagger H_0 v_n - \frac{i}{2} |w_n|^2, & \text{for } n \leq M, \\ u_n^\dagger H_0 u_n, & \text{for } n > M. \end{cases} \quad (2.48)$$

Only M eigenvalues obtain imaginary parts. The remaining $N - M$ eigenvalues, on the other hand, remain undamped (at least to first order in perturbation theory).

The eigenvalues distribution of Hamiltonians of the type (2.33) have been studied numerically and analytically by Haake, Lehmann and coworkers [Leh95a, Haa92]. Fig. 2.4 shows the distribution of complex eigenvalues of H_{eff} in the complex plane for $M = 25$ and $N = 100$ across different coupling strengths κ . At weak coupling of $\kappa = 0.2$, the eigenvalues are densely distributed around the real axis, indicating that long-lived states with narrow widths are very common. As the coupling strength increases to $\kappa = 0.5$ and $\kappa = 1$, the eigenvalues begin to spread vertically, reflecting their imaginary components grow. By $\kappa = 2$, an upper cloud forms, representing superradiant states that are significantly shorter-lived due to their large imaginary components. This cloud becomes more pronounced and separates further from the main body at $\kappa = 5$, where the distribution shows a clear bifurcation, superradiant states and the bulk of more stable, long-lived states. Note, that the short lived states for $\kappa = 5$ show statistically a similar behavior as for $\kappa = 1/5 = 0.2$. Thus predictions from RMT are often valid also for the over coupling case but solely for the short-lived part taking then the κ as $1/\kappa$.

The examples provided above offer a straightforward illustration of the fundamental principles involved, but when applying these concepts to various complex wave systems, more targeted discussions are required. It is important to emphasize that the large widths of superradiant states make their experimental detection exceedingly difficult. Consequently, there are very few experimental investigations into these phenomena, highlighting a substantial gap.

In this thesis, two examples of the superradiant states will be discussed. The first involves the poles in complex microwave networks, where their widths tend to be

come infinitely large by a parametric variation. The second relates to our findings in chaotic RC, where, according to numerical predictions, the zeros we observed in the experiment are expected to demonstrate large widths of corresponding resonances. These topics will be discussed in detail in chapters 3 and 4, respectively.

Chapter 3

Superradiance in Non-Weyl Microwave Networks

Contents

3.1	Quantum Graphs	26
3.1.1	<i>The Vertex Secular Equation</i>	26
3.1.2	<i>Scattering Properties of Graphs</i>	27
3.1.3	<i>Bond Scattering Matrix and Secular Equation</i>	28
3.2	Microwave Networks	30
3.2.1	<i>Microwave Network Components</i>	30
3.2.2	<i>Modeling Variable Phase: Length Transformation</i>	32
3.2.3	<i>Modeling Variable Channel Openness</i>	34
3.3	Weyl's Law in Graphs	36
3.3.1	<i>Weyl Graphs</i>	36
3.3.2	<i>Non-Weyl Graphs</i>	37
3.3.3	<i>Motivation</i>	39
3.4	Non-Weyl Tetrahedral Graphs	40
3.4.1	<i>Microwave Setup</i>	40
3.4.2	<i>Spectra Transformation</i>	40
3.4.3	<i>Experimental Findings</i>	43
3.5	Non-Weyl Lasso Graphs	45
3.5.1	<i>Analytical Description</i>	45
3.5.2	<i>Numerical Findings</i>	46
3.5.3	<i>Rational Lasso Graphs</i>	47
3.5.4	<i>Experimental Findings</i>	48
3.5.5	<i>Other Examples</i>	49
3.6	Conclusion	51

3.1 Quantum Graphs

Quantum graphs are composed of bonds which are connected with each other at vertices. Along the bonds wave propagation is governed by the Schrödinger equation without potential. The boundary conditions depend on the details of the vertices. Quantum graphs were first introduced by Pauling [Pau36] in the context of free electron models of organic molecules. Later, they were studied intensely in physics [Kot97] and mathematics [Ber13], and experimentally implemented in correspondingly-shaped microwave networks [Hul04], waveguide cavity [Zha22a, Die24], insulator integrated photonic networks [Wan23] and photonic topological insulator [Ma24]. Using supersymmetry techniques Gnutzmann and Altland [Gnu04] proved the RMT conjecture (see subsection 2.2.3) for the two-point correlation function for fully connected graphs with incommensurate bond lengths and infinite size. Their result was generalized to all correlation functions by Pluhař and Weidenmüller [Plu14].

3.1.1 The Vertex Secular Equation

Here we look more in detail into the mathematical description of graphs, following the work by Kottos and Smilansky [Kot99] and reference [Hof21]. In time-reversal invariant graphs (absence of magnetic vector potential), the wave field ψ_{nm} on the bond connecting vertices n and m obeys the following relation

$$-\frac{d^2}{dx^2}\psi_{nm}(x) = k^2\psi_{nm}(x), \quad (3.1)$$

where k is the wavenumber and x is the distance to vertex n . The wave fields within the graph have to obey two constraints. The first one is energy conservation

$$\psi_{nm}(x)|_{x=0} = \varphi_n, \quad \psi_{nm}(x)|_{x=l_{nm}} = \varphi_m, \quad (3.2)$$

where l_{nm} is the length of the bond, and this means that at each vertex n there exists a unique potential φ_n for all bonds meeting at this vertex. This condition is automatically met by means of the ansatz

$$\psi_{nm}(x) = \frac{1}{\sin kl_{nm}} [\varphi_n \sin k(l_{nm} - x) + \varphi_m \sin kx]. \quad (3.3)$$

The second constraint is current conservation at each vertex n

$$\sum_m \left. \frac{d\psi_{nm}(x)}{dx} \right|_{x=0} = 0, \quad (3.4)$$

where the sum is over all bonds connecting to vertex n . Eq. (3.4) holds for Neumann boundary conditions at the vertices. Plugging the expression (3.3) into Eq. (3.4), we obtain an homogeneous linear equation system for the potentials

$$\sum_m h_{nm}\varphi_m = 0, \quad (3.5)$$

where

$$h_{nm} = -\delta_{nm} \sum_{m'} f_{nm'} + g_{nm}, \quad (3.6)$$

with

$$f_{nm} = \cot kl_{nm}, \quad g_{nm} = \frac{1}{\sin kl_{nm}}, \quad (3.7)$$

for existing connections from vertex n to m and $f_{nm} = g_{nm} = 0$ otherwise. In reference [Kot99], matrix h is constructed via the connectivity matrix and length matrix. For the homogeneous equation system (3.5) nontrivial solutions exist if the determinant of the matrix $h(k)$ with elements $h_{nm}(k)$ vanishes,

$$\det h(k) = 0. \quad (3.8)$$

The roots k_n of this equation generate the spectrum of the graph.

3.1.2 Scattering Properties of Graphs

For an experimental study of the spectral properties, the graph has to be opened by attaching external leads. Let us hence assume that a single lead is attached to the vertices $1, \dots, N$. The field within the lead may be written as the superposition of two waves propagating in opposite directions

$$\psi_n(x) = a_n e^{-ikx} + b_n e^{ikx}, \quad n = 1, \dots, N, \quad (3.9)$$

where x is the distance to the vertex along the bond, and a_n and b_n are the amplitudes of the waves propagating towards and away from the vertex, respectively. Note, that in this thesis, the second term in Eq. (3.9) has a positive sign, following the definition in [Kot99], while in quantum dots, quantum billiard or nuclear physics, one prefers to use a negative sign, see also Eq. (2.24).

Also for the attached open leads, the wave fields need to follow two constraints at the vertices $1, \dots, N$, one being energy conservation

$$\psi_j(0) = a_j + b_j, \quad (3.10)$$

the other being current conservation

$$\left. \frac{d\psi_j(x)}{dx} \right|_{x=0} + \sum_m \left. \frac{d\psi_{nm}(x)}{dx} \right|_{x=0} = i(b_j - a_j) + \sum_m h_{jm} \varphi_m = 0 \quad (3.11)$$

for $j = 1, \dots, N$. Now the equation system (3.11) has become inhomogeneous,

$$h\varphi = i(a - b), \quad (3.12)$$

where $a = (a_0, \dots, a_N, 0, \dots)^T$ and $b = (b_0, \dots, b_N, 0, \dots)^T$. It follows that

$$\varphi = ih^{-1}(a - b). \quad (3.13)$$

Following the constrain (3.10) at the coupling vertices $1, \dots, N$, the φ_j are fixed

$$a + b = ih^{-1}(a - b). \quad (3.14)$$

Incoming and outgoing amplitudes are connected via the scattering matrix S

$$b = Sa. \quad (3.15)$$

By defining $G = h^{-1}(k)$ analogous to the Green function, the scattering matrix yields

$$S = -\frac{\mathbb{I} - iG}{\mathbb{I} + iG}. \quad (3.16)$$

Here S is unitary since h is hermitian, which ensures current conservation. This expression is similar to the Eq. (2.30), but with a negative sign due to the definition of fields in Eq. (3.9).

The $N \times N$ scattering matrix in Eq. (3.16) is obtained from the graph that every vertex is connected to an ideal coupled channel. In fact, especially in experiments, it is not necessary to couple all N vertices. Thus, by considering a more general case, we can assume that an arbitrary set of L vertices are coupled, with $1 \leq L \leq N$. The $L \times L$ scattering matrix S has to be modified in the following way [Kot99]

$$S = -\mathbb{I} + 2iW^T \frac{1}{h_{\text{eff}}(k)} W, \quad (3.17)$$

with

$$h_{\text{eff}}(k) = h(k) + iWW^T. \quad (3.18)$$

where $W_{ln} = \delta_{ln}$ is the $L \times N$ leads-vertices coupling matrix, for the case that we previously examined, with $L = N$ and $W = \mathbb{I}$. One can obtain the poles of the scattering matrix with the determinant of h_{eff} vanishing

$$\det h_{\text{eff}}(k) = 0. \quad (3.19)$$

Note, that it is important to distinguish between Eq. (2.32) and Eq. (3.17), the former comes from the effective Hamiltonian approach, and the latter is used to specifically describe the scattering matrix of the quantum graph. The effective Hamiltonian H_{eff} in Eq. (2.32) is independent of energy E , while in quantum graph, h_{eff} depends on wavenumber k .

3.1.3 Bond Scattering Matrix and Secular Equation

Another method of quantization of graphs is accomplished in a different way which is less efficient from the numerical point of view, but provides us with a natural, intuitive and convenient starting point for understanding the scattering process in quantum graphs [Kot97, Kot99, Kot03].

The general expression of the wave field on a bond d in a quantum graph is written as a superposition of two waves traveling in opposite directions:

$$\psi_d(x) = a_d e^{-ikx} + b_d e^{ikx}, \quad (3.20)$$

where a_d and b_d are the incoming and outgoing wave amplitudes and k is the wavenumber. In a vertex i where v bonds meet, the wave field must satisfy both energy and current conservation

$$\begin{cases} a_{d_1} + b_{d_1} = a_{d_2} + b_{d_2} = \dots = a_{d_v} + b_{d_v}, \\ ik \sum_{j=1}^v (a_{d_j} - b_{d_j}) = 0, \end{cases} \quad (3.21)$$

and they can be restructured into a matrix form, linking the incoming and outgoing wave amplitudes at vertex i :

$$\begin{pmatrix} b_{d_1} \\ b_{d_2} \\ \dots \\ b_{d_v} \end{pmatrix} = \sigma^{(i)} \begin{pmatrix} a_{d_1} \\ a_{d_2} \\ \dots \\ a_{d_v} \end{pmatrix}, \quad (3.22)$$

with $\sigma^{(i)}$ being a unitary matrix that characterizes the scattering at the vertex:

$$\sigma_{jj'}^{(i)} = -\delta_{jj'} + \frac{2}{v}. \quad (3.23)$$

For the corresponding time-reversed bond \hat{d} , the wave field is given by

$$\psi_{\hat{d}}(x) = a_{\hat{d}} e^{-ik(l_d-x)} + b_{\hat{d}} e^{ik(l_d-x)}, \quad (3.24)$$

and this leads to a relationship between the outgoing wave from the vertex i in the direction of vertex j and incoming wave at j coming from i , showing that they are essentially the same except for a phase shift

$$b_d = e^{-ikl_d} a_{\hat{d}}, \quad b_{\hat{d}} = e^{-ikl_d} a_d. \quad (3.25)$$

The combination of Eq. (3.22) and (3.25) leads to a set of $2B$ homogeneous linear equations for a closed graph. The existence of non-trivial solutions of these equations are determined by the secular equation:

$$\zeta_B(k) = \det [\mathbb{I} - S_B(k; \{\Phi_{ij}\})] = 0, \quad (3.26)$$

where S_B is the ‘‘bond scattering matrix’’, a $2B \times 2B$ unitary matrix defined in the $2B$ space of directed bonds

$$S_B(k; \{\Phi_{ij}\}) = D(k; \{\Phi_{ij}\})T, \quad (3.27)$$

with D being a diagonal unitary matrix that represents the metric properties of the graph, and T being a unitary matrix that encodes the graph’s connectivity and vertex scattering processes

$$D_{ij,nm} = \delta_{in} \delta_{jm} e^{ikL_{ij} + \Phi_{ij}}, \quad T_{ji,nm} = \delta_{ni} \delta_{ji} \delta_{nm} \sigma_{ji,nm}^{(i)}, \quad (3.28)$$

where L_{ij} represents the length of the bond from vertex i to vertex j , Φ_{ij} incorporates the additional phase in the bond, and the directionality is incorporated in the

transition matrix $T_{ji, nm}$ from vertex m to vertex j via vertex i .

Now, we can open the graph by introducing vertex reflection amplitude $\rho^{(i)}$ and the lead–bond transmission amplitudes $\{\tau_j^{(i)}\}$

$$\rho^{(i)} = \frac{2}{\tilde{v}} - 1, \quad \tau_j^{(i)} = \frac{2}{\tilde{v}}, \quad \sigma_{jj'}^{(i)} = -\delta_{jj'} + \frac{2}{\tilde{v}}, \quad (3.29)$$

where \tilde{v} represents the valency of vertex i , accounting for the number of bonds and channels at vertex i . For vertices that are not connected to leads, the vertex reflection amplitude is set to $\rho^{(i)} = 1$, and the lead–bond transmission amplitudes to $\tau_j^{(i)} = 0$. With these definitions, we can construct the $V \times V$ unitary scattering matrix

$$S_{ij}^{(V)} = \delta_{ij} \rho^{(i)} + \sum_{rs} \tau_r^{(i)} (\mathbb{I} - S_B(k; \{\Phi_{ij}\}))_{(ir), (sj)}^{-1} D_{(sj)} \tau_s^{(j)}. \quad (3.30)$$

Note, that S_B or D is not unitary anymore, since the graph has been coupled to external leads.

The advantage of the method discussed in this subsection is that it can describe quantum graph as close as possible to the experimental situation, for example, it can describe circulators and it can also account for phases in the bonds [Lu20, Che21a, Che22a]. This is exactly why, in this chapter, we will use this method to numerically simulate our network. Its disadvantage is that it deals with $2B \times 2B$ matrices, which requires more computing resources than the method introduced in subsection 3.1.1.

3.2 Microwave Networks

Just as quantum billiard and microwave billiard [Stö90, Kuh13, Die15, Stö22], there is a one-to-one correspondence between a quantum graph and the corresponding microwave network, which has been used in many experiments to study spectral and scattering properties of microwave graphs [Hul04, Lawni10, Reh16, Die17, Lawni19, Lu20, Che20, Che21a, Stö22, Lu24, Lawni24].

3.2.1 Microwave Network Components

Microwave networks are constructed from standard microwave coaxial cables connected by T junctions, see Fig. 3.1 (a) and (b). These cables are composed of an inner conductor surrounded by an outer conductor, and the space between them is filled with Teflon of permittivity ϵ . When operating below the cable’s cutoff frequency, each cable supports a single propagating mode known as the TEM₀₀ mode. This mode can be described by the following one-dimensional wave equation:

$$-\frac{d^2}{dx^2} U(x) = \frac{\omega^2 \epsilon}{c^2} U(x). \quad (3.31)$$

Here, $U(x)$ denotes the difference between the potentials at the conductors’ surfaces, c is the velocity of light, and $\omega = 2\pi\nu$ is the angular frequency with ν the microwave frequency. Eq. (3.31) is the telegraph equation, which is applicable for describing lossless coaxial cables. At the T-junctions, where the cables are connected and

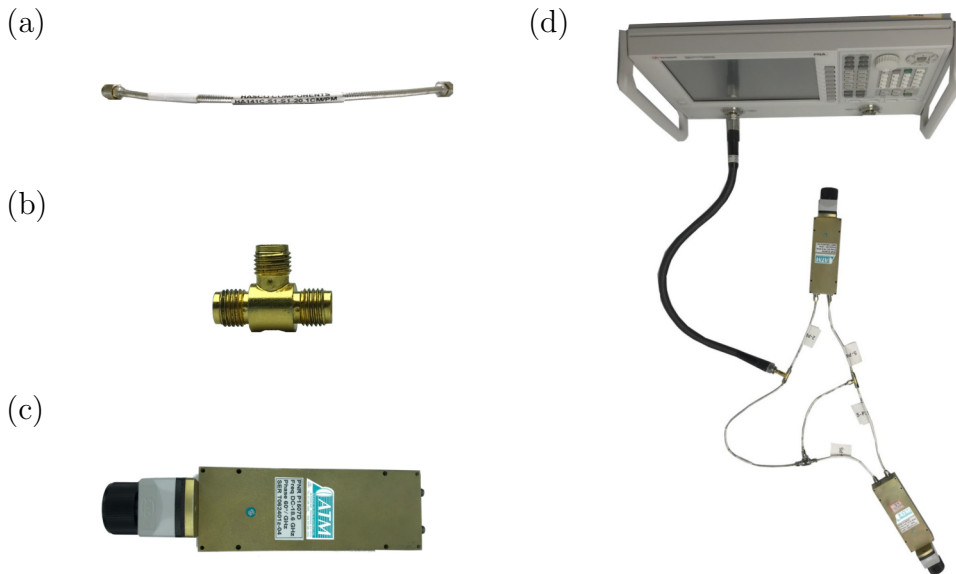


Figure 3.1: (a) Photo of a coaxial cable. (b) Photo of a T junction. (c) Photo of a phase shifter. (d) A VNA measures the reflection spectrum of a microwave network via a black coaxial cable.

which correspond to vertices with valency 3, the potential difference $U(x)$ is subject to the laws of energy and current conservation. In an ideal Neumann scenario, the scattering matrix at these T-junctions is given by:

$$S_T = \frac{1}{3} \begin{pmatrix} -1 & 2 & 2 \\ 2 & -1 & 2 \\ 2 & 2 & -1 \end{pmatrix}, \quad (3.32)$$

which aligns with the unitary vertex scattering matrix in Eq. (3.23).

Consequently, when the boundary conditions are applied, Eq. (3.31) becomes mathematically analogous to the equation of a quantum graph with Neumann boundary conditions. By equating the term $\sqrt{\epsilon}\omega/c$ from the microwave network with the wavenumber k of the quantum graph, it is revealed that the eigenfrequencies of the microwave network correspond to the eigenvalues of the quantum graph. It is important to note that within the context of this thesis, the term “length” for cables invariably refers to the electrical length, thereby simplifying the relationship to $k = \omega/c$.

The advancement of microwave graph experiments has incorporated the use of microwave phase shifters, as seen in Fig. 3.1(c). Phase shifters can be thought of as variable-length coaxial cables, where the electrical length can be adjusted, and will be used in our experiments.

In addition to these microwave components, common ones such as open or short terminals [Hul12, Reh16], isolators [Hul04, Che22a], circulators [Bia16, Reh16, Che20, Che22a], hybrids [Che22a, Far24], and attenuators [All14, Che20] can all be applied to microwave networks to achieve different effects. A vector network analyzer (VNA) measures the reflection from one open cable attached to the graph, see Fig. 3.1(d).

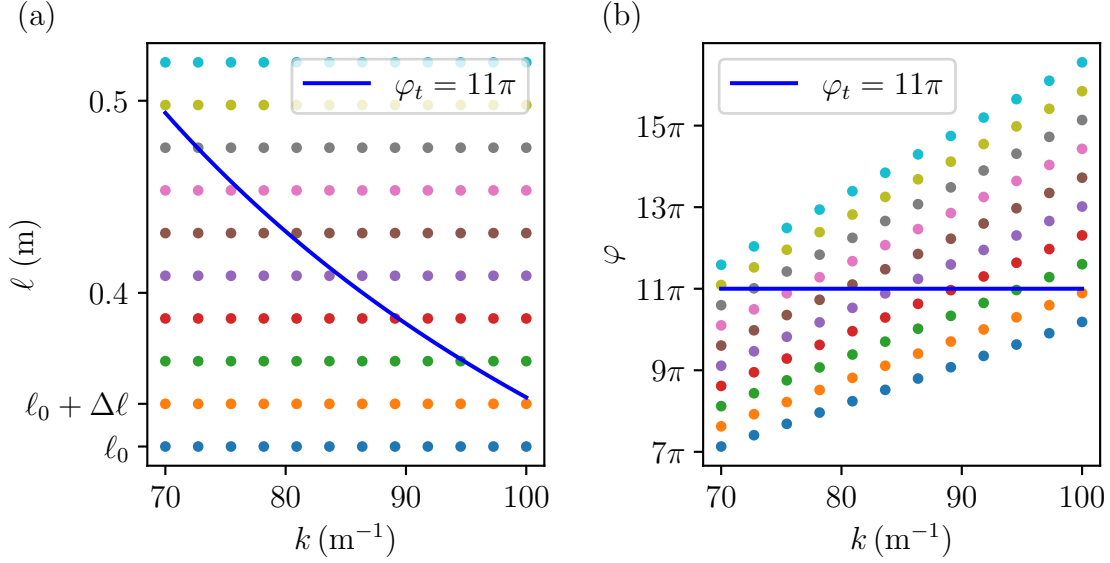


Figure 3.2: (a) This sketch displays measurement points for varying lengths ℓ of the phase shifter with same wavenumber positions, each represented by a unique color. The blue curve represents the constant phase, which is the product of the wavenumber k and length ℓ , and it equals 11π . (b) This sketch shows the transformation of the y-axis from the length ℓ of the phase shifter to the phase φ , with the horizontal blue line marking the phase value of 11π .

Microwave technology is subject to the $50\ \Omega$ convention, meaning an ideal matching of the cables connected to the VNA and each attached cable connected to the VNA is effectively an open channel with no reflections from the end.

3.2.2 Modeling Variable Phase: Length Transformation

In microwave network experiments, one uses coaxial cables and T-junctions to build networks with diverse connectivity and metric properties. In the study, one often encounters the need to vary parameters, such as changing the length of a bond or achieving a phase difference. In this subsection, we will introduce how to achieve length and phase changes in microwave networks.

Historically, if one wants to change the bond lengths, which would involve physically replacing coaxial cables of varying lengths. However, the advent of phase shifters has offered a more convenient approach. By connecting a phase shifter to a stepper motor, we can dynamically change the effective length of the phase shifter through computer commands that also control the measurements of a VNA, and finally obtain the spectra of a set of networks with different lengths.

The process is illustrated in Fig. 3.2, which is a sketch, not a true example. In Fig. 3.2 (a), we plot a series of points in the k - ℓ plane, where k is the wavenumber, and ℓ is the length of phase shifter. The blue points (k, ℓ_0) correspond to a measurement result, where their position on the x-axis is determined by the measured wavenumber k , and position on the y-axis is determined by length ℓ_0 . Each point can contain information about the scattering matrix, such as reflection $S_{11}(k, \ell_0)$ or

transmission $S_{12}(k, \ell_0)$. Now, if the phase shifter length is modified by an increment $\Delta\ell$, and the system remeasured at the same wavenumber points, we will acquire a new measurement result, $(k, \ell_0 + \Delta\ell)$, denoted by orange dots. The length of the phase shifter is repeated increasing by $\ell = \ell_0 + n\Delta\ell$, where $n = 1, 2, \dots$, so that a set of spectra could be obtained.

Sometimes one would like to introduce a phase in the network. For example, A. Rehemangiang and colleagues aimed to experimentally realize a quantum graph with energy spectrum statistics resembling GSE [Reh16]. This required a pair of subgraphs, emulating a spin up and down states, coupled at two symmetry points with a π phase difference between these two coupling points [Joy14]. Attempts using circulators and IQ modulators to achieve the necessary conditions for the experiment did not yield satisfactory results [Reh18] because of insertion losses. The successful strategy emerged with the application of a phase shifter, which effectively varies the bond length and thus the phase of the microwaves, as they pass through according to

$$\varphi = k\ell = \frac{2\pi\nu}{c}\ell, \quad (3.33)$$

where φ is the phase shift that varies with microwave frequency ν or wavenumber k .

Here we will use the example of Fig. 3.2 (a) to explain how to transform length to phase. In Fig. 3.2 (a), the y-axis of all points (k, ℓ) represents length of phase shifter ℓ . By keeping the x-axis position of these points unchanged, multiplying their y-axis values by their respective k values, we get a new y-axis, $k \rightarrow k\ell = \varphi$. As shown in Fig. 3.2 (b), after the transformation, these points (k, φ) appear distorted from the overall view. Since here only the points shown in (a) are transformed, it leads to the lower and upper boundary of measurement points in the figure. Note, that the scattering matrix information contained in these points are not changed.

Now, we will describe in detail how to extract the new spectrum with constant phase. Take the blue lines in Fig. 3.2 (a) and (b) as an example. They represent a spectrum with constant target phase φ_t , which is exactly what one wants to realize in experiment. Here $\varphi_t = 11\pi$. For each wavenumber k_i , we can choose the two points closest to the constant phase line, one point is (k_i, φ_1) , and the other point is (k_i, φ_2) , where $\varphi_1 < \varphi_t < \varphi_2$. We can then pick the scattering matrix information contained in these two points, $S(k_i, \varphi_1)$ and $S(k_i, \varphi_2)$, and perform a linear interpolation to obtain the complex $S(k_i, \varphi_t)$. Choosing $i = 1, 2, \dots$, we can get a spectrum $S(k, \varphi_t)$ with constant bond phase (zero bond length).

The quality of this new interpolated spectrum depends on the step size $\Delta\ell$ and the number of wavenumber points. Ideally, every 2π increment in phase φ_t should yield an identical spectrum; however, due to distortion of the overall positions of the spectrum points, their wavenumber ranges should be different. Also the microwave absorption in the network will lead to differences. In section 3.4 and 3.5, we will apply this transformation method to experimentally study tetrahedral and lasso graphs. In next subsection 3.2.3, we will introduce another parameter, the channel openness of the graph.

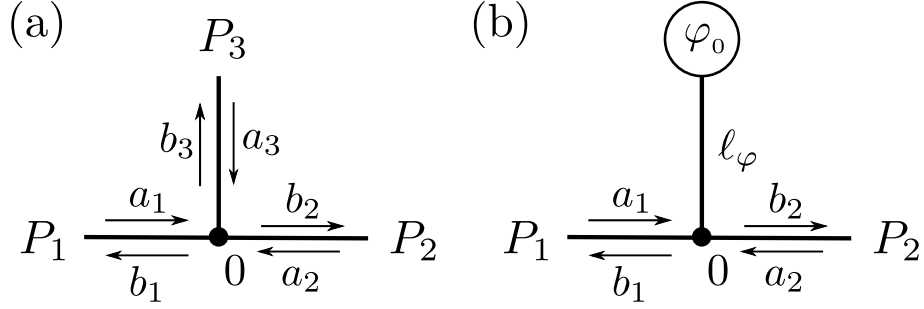


Figure 3.3: (a) Sketch of the T-junction. (b) Sketch of the T-junction with a bond ℓ_φ and a reflecting terminal φ_0 .

3.2.3 Modeling Variable Channel Openness

In microwave network experiments, the networks are attached with channels, i.e. coaxial cables, to the VNA. Due to the impedance matching in microwave components, the couplings from the channels are ideal, and their strengths are invariably fixed. This is a restriction as sometimes one would like to tune the coupling strength to the network to vary the “openness” of the graph over a large frequency range. Here, we will introduce a method to resolve this dilemma, which can indirectly adjust the coupling strength.

Let’s first discuss the properties of a T-junction as shown in Fig. 3.3 (a). The unitary scattering matrix S_T of the T-junction given by Eq. (3.32) connects the incoming vector $\vec{a}_T = (a_1, a_2, a_3)^T$ to the outgoing vector $\vec{b}_T = (b_1, b_2, b_3)^T$

$$S_T \vec{a}_T = \vec{b}_T. \quad (3.34)$$

Now we connect a bond with length ℓ_φ and a reflecting terminal of phase φ_0 at one of the ports, see Fig. 3.3 (b). Thus, at vertex 0 of the T-junction a total phase $\varphi = 2k\ell_\varphi + \varphi_0$ is acquired by the wave relating $a_3 = b_3 S_3$, where $S_3 = \exp(i\varphi)$. For an open terminal (emulating Neumann boundary condition), $\varphi_0 = 0$. Then we can calculate the transmission from a_1 to b_2 by assuming $a_2 = 0$, and Eq. (3.34) becomes

$$\frac{1}{3} \begin{pmatrix} -1 & 2 & 2 \\ 2 & -1 & 2 \\ 2 & 2 & -1 \end{pmatrix} \begin{pmatrix} a_1 \\ 0 \\ a_3 \end{pmatrix} = \begin{pmatrix} b_1 \\ b_2 \\ b_3 \end{pmatrix}. \quad (3.35)$$

By reducing the 3×3 scattering matrix of the T-junction in Fig. 3.3 (a), to the 2×2 scattering matrix of the T-junction in Fig. 3.3 (b), we find

$$S_\varphi = \begin{pmatrix} r_\varphi & t_\varphi \\ t_\varphi & r_\varphi \end{pmatrix}, \quad (3.36)$$

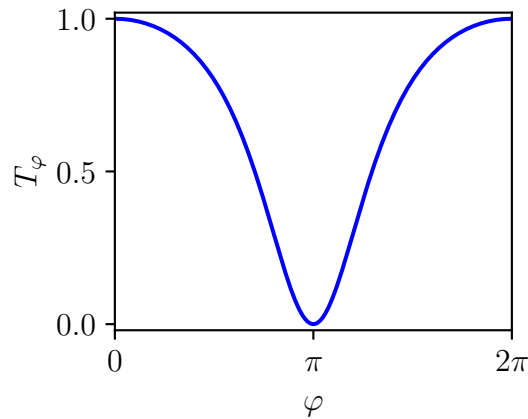


Figure 3.4: T_φ as a function the phase φ , the results is calculated from Eq. (3.39).

with

$$t_\varphi = \frac{b_2}{a_1} = \frac{2(1 + e^{i\varphi})}{3 + e^{i\varphi}}, \quad (3.37)$$

$$r_\varphi = \frac{b_1}{a_1} = \sqrt{1 - t_\varphi^2}. \quad (3.38)$$

This lead to the transmission coefficient of the T-junction

$$T_\varphi = |t_\varphi|^2 = \left| \frac{2(1 + e^{i\varphi})}{3 + e^{i\varphi}} \right|^2. \quad (3.39)$$

In Fig. 3.4, the blue line represents the relationship between φ and T_φ . It is shown that, by varying the phase φ from 0 to 2π , the transmission coefficient T_φ is changed between 0 and 1. An intuitive way to understand this phenomenon is that, the wave propagating to the upper part of the T-junction is reflected and collected a phase shift of φ , so it interferes with the excitation. If $\varphi = \pi$, this results in the wave value at the vertex needing to be 0, thus imposing a Dirichlet condition on both sides of the T-junction, effectively separating the right side from the left side, which leads to $T_\varphi = 0$. While if $\varphi = 0$ or 2π , then the wave travels free from P_1 to P_2 , and $T_\varphi = 1$.

In this way, the openness of the channel can be adjusted, which affects the transmission coefficient of the system and indirectly changes the coupling. More importantly, this simple setup can be implemented experimentally, since a fixed phase can be achieved through a phase shifter and a corresponding transformation, as we mentioned in the previous subsection 3.2.2. Thus, the approach here lays the foundation for subsequent experimental study. In section 3.4 and 3.5, we will use this method to change the coupling of the system.

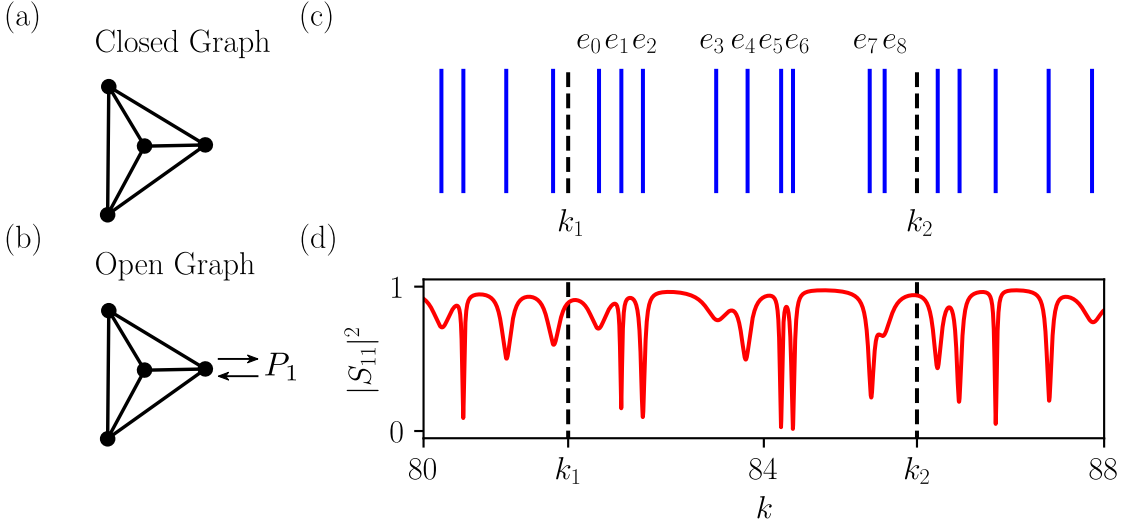


Figure 3.5: (a) Sketch of the closed Weyl graph and (b) open Weyl graph. (c) Eigenvalues calculated from closed graph (a), each solid blue line represents an eigenvalue. (d) Reflection spectrum $|S_{11}|^2$ calculated from open graph (b) with complex wavenumber $k+0.009i$, and each dip corresponds to a resonance. The black dashed lines represent the windows k_1 and k_2 , where we count the number of resonances and eigenvalues.

3.3 Weyl's Law in Graphs

In subsection 2.2.2, we introduced the Weyl's law for 1D graph system. When the graph is closed, Weyl's law always works, but if the graph is opened, Weyl's law may fail. In this section, for simplicity, we refer to graphs that satisfy the behavior on the wavenumber k as Weyl graphs, and graphs that do not meet the predictions of the asymptotes as non-Weyl graphs, and discuss them separately.

3.3.1 Weyl Graphs

In this subsection, we will give two examples of Weyl graphs. The first one is the closed tetrahedral graph, see Fig. 3.5 (a), without any connection to the outside. The spectrum of the graph is a combination of discrete eigenvalues, as shown in Fig. 3.5 (c). The second one is the open tetrahedral graph, see Fig. 3.5 (a), one vertex of the graph is attached with a single channel P_1 . In the open graph case, the spectrum is no longer discrete, but consists of resonances, see Fig. 3.5 (d).

To compare them with the prediction of Weyl's law, we plot the eigenvalues calculated from closed graph (a) as blue circles, and the resonances extracted from open graph (b) as red triangles in the complex plane, see Fig. 3.6 (a). We define a window k_1 and k_2 (dashed black lines) and count the number of resonances and eigenvalues with their real part between these two wavenumbers, and find that the number of resonances and eigenvalues are the same, and it can be predicted by the following equation, which is deduced from Eq. (2.14),

$$\Delta N = \frac{L}{\pi}(k_2 - k_1). \quad (3.40)$$

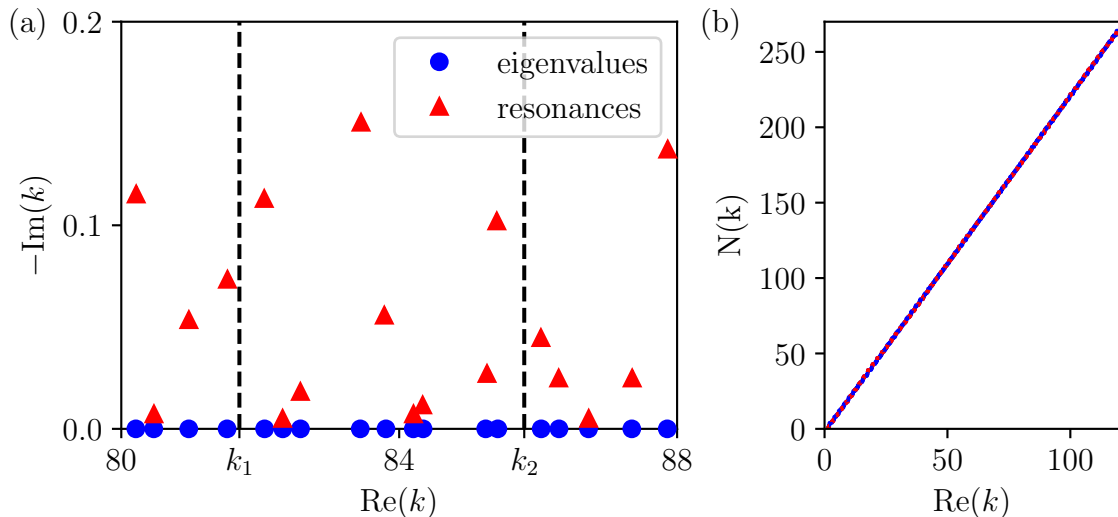


Figure 3.6: (a) Plot of the eigenvalues and resonances in complex plane. The blue circles and the red triangles denote the eigenvalues of closed graph and the resonances of open graph, respectively. (b) The counting functions $N(k)$ for the closed (blue step function) and open graph (red dotted step function).

However, this comparison is not rigorous enough. When the graph is opened, the real and imaginary parts of the resonances will be slightly shifted from the eigenvalues in the complex plane, and the number of eigenvalues for graph (a) and resonances for graph (b) may depend on how the chosen window, so one of the safest method is to compare their counting functions with the prediction of Weyl's law. See Fig. 3.6 (b), two counting functions start from $k = 0$, and as k increases, the blue and red step functions almost coincide, indicating the number of eigenvalues for graph (a) and resonances for graph (b) versus k are almost the same. Fitting these two counting functions to the Weyl's law, we can relate the fit to the total length that graph should have. This shows closed and open graphs in Fig. 3.5 are Weyl graphs. In next subsection 3.3.2, we will present the example of non-Weyl graph, where the extracted length does not correspond to the total length.

3.3.2 Non-Weyl Graphs

There are several ways to make a graph to a non-Weyl graph, for example one can introduce balanced-vertex to the graph [Lawni19], or introduce a magnetic field to the external leads [Dav10, Exn11], etc. Here, we will present a non-Weyl graph that has the simplest balanced-vertex, meaning that the number of leads connected to the vertex is the same as the number of internal bonds connected, which is 1.

In Fig. 3.7 (a), the sketch represents an open graph consisting of tetrahedral graph and a dangling bond ℓ_d , and its vertex 0 is coupled to the lead P_1 . Fig. 3.7 (b) shows the closed version of the graph in Fig. 3.7 (a). The total length of each of the two graphs is L . Numerically, we can compute resonances of open graph (a) and eigenvalues of closed graph (b), and plot them in the complex plane, see Fig. 3.7 (c). We observe that, in the wavenumber window between k_1 and k_2 , the number of resonances for the open graph in Fig. 3.7 (a) is different from the number

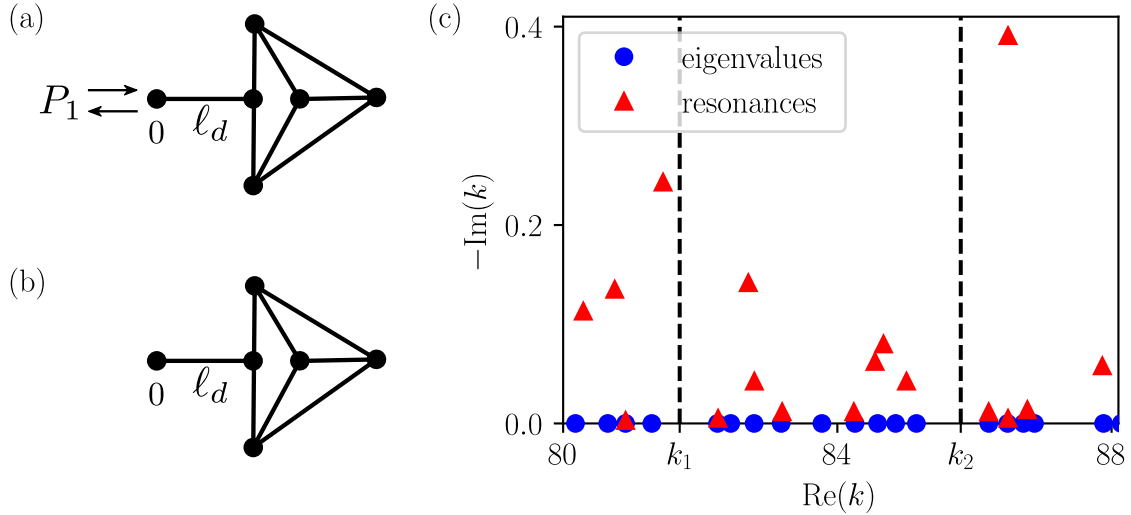


Figure 3.7: (a) Sketch of the non-Weyl graph. (b) Same graph as in (a), but without coupling. (c) Plot of the eigenvalues and resonances in complex plane. The blue circles denote the eigenvalues obtained from the closed graph (b), where there is no coupling from outside. The red triangles denote the resonances extracted from the open graph (a).

of eigenvalues for the closed graph in Fig. 3.7 (b). Specifically at $k \approx 83.8$, we can only find one eigenvalue, with no corresponding resonance around it, and this does not seem to be related to the window selection or missing levels, since the phenomenon occurs in the middle of the window and there are no missing solutions in our numerical calculations.

To show a more convincing result, we plot the counting functions of the eigenvalues of the closed graph (blue step function) and the resonances of the open graph (red step function) in Fig. 3.8. It is obvious that the two functions have different slopes and deviate from each other. For the closed graph in Fig. 3.7 (b), the number of its eigenvalues is satisfying the prediction of Weyl's law (2.14). However, for the open graph in Fig. 3.7 (a), it is shown that the number of the resonances is reduced. By fitting the counting function of open graph, we find the total length is no longer L , thus Weyl's law is not valid. In this case, the number of resonances is given by

$$N(k) = \frac{L'}{\pi}k + c, \quad L' = L - \ell_d. \quad (3.41)$$

The above results can be understood in the following way. When the graph is closed, like the one in Fig. 3.7 (b), the wave will travel to all bonds, and the total length must be L . When the graph is in perfect coupling with a dangling bond, such as the graph in Fig. 3.7 (a), the perfect matching condition removes any scattering at the vertex 0, thus resonances of the graph are only relevant to the tetrahedron, and the total length becomes effective L' . Note, that, since the reference point of the scattering is still at vertex 0, the length ℓ_d still appears in the reflection amplitude as an additional acquired global phase $\Phi_d = 2k\ell_d$.

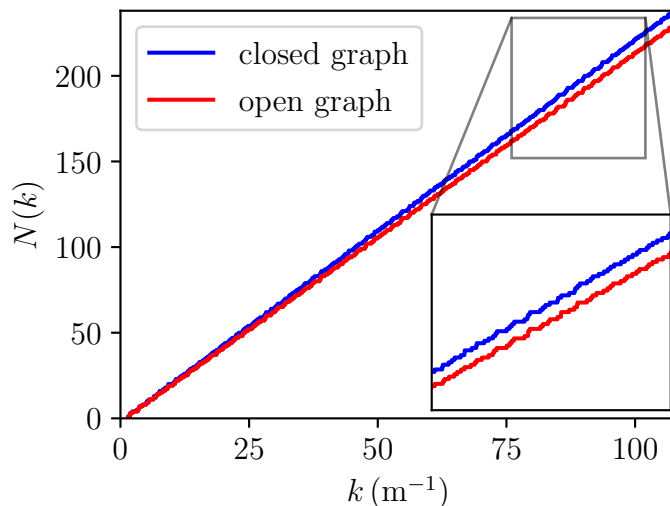


Figure 3.8: The counting function $N(k)$ of the closed graph in Fig. 3.7 (b) is represented by a blue step function, and $N(k)$ of the open graph in Fig. 3.7 (a) is represented by a red step function. The inset shows a zoom.

3.3.3 Motivation

Non-Weyl behavior has been observed experimentally by Lawniczak et al. [Lawni19] for a vertex with two semi-infinite leads and two internal bonds. In a small wavenumber region, the authors noticed a reduction of the number of resonances by two or three, in good agreement with the theoretical expectations. In the experiment the loss of resonances [Lawni17] due to negligible coupling to the openings (or no coupling as in case of BICs) is always a problem. In particular, there is never a guarantee that all resonances are found.

In subsection 3.3.2, we numerically study a non-Weyl graph for a vertex with one semi-infinite lead and one internal bond, see Fig. 3.7 (a). The analysis there confirms that Weyl's law cannot adequately describe this graph, because the total effective length is reduced to L' . Although, unlike experiments, our numerical approach does not encounter the same difficulties in extracting all resonances as observed in experiments, a key question remains: where are the missing resonances going, and is it possible to make them reappear in the complex plane experimentally?

Recalling the two graphs in Fig. 3.7, each representing an extreme configuration: one is closed and the other is fully open. What happens when the system is at intermediate coupling values? Could this offer insight into the non-Weyl behavior we observe? A practical method for varying the coupling has been proposed in subsection 3.2.3, involving the incorporation of a T-junction with a phase-adjustable bond. This experimental approach allows for the parametric tracking of resonances in the complex plane by varying the coupling. Not only does this help to overcome the challenge of experimentally determining resonances, but it also enables us to observe the transition of resonances to their final disappearance.

Thus, in section 3.4 and 3.5, we will parametrically study two examples, tetrahedral and lasso graphs, and try to explain the non-Weyl behavior in these graphs.

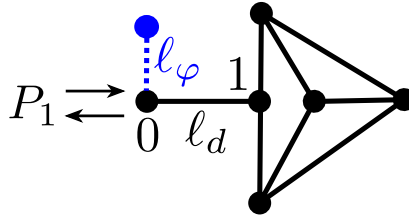


Figure 3.9: Sketch of the tetrahedral graph.

3.4 Non-Weyl Tetrahedral Graphs

3.4.1 Microwave Setup

This subsection details the microwave experimental setup used to study the tetrahedral graph, as illustrated in Fig. 3.9. On the left side of the graph, there is a T-junction, which is exactly used to vary the coupling parameters of the system, see the discussions in subsection 3.2.3.

The first port of the T-junction is connected to the analyzer, and P_1 represent the port 1 of VNA (Agilent 8720ES), where the reflection amplitude S_{11} is measured. The second port of the T-junction is connected to a bond (blue part) with length ℓ_φ terminated by an open (corresponding to Neumann boundary condition), and ℓ_φ is varied using a phase shifter (ATM, P1507). The third port of the T-junction is connected to a graph, which consists of a dangling bond with length $\ell_d = 0.2435$ m and a tetrahedral graph with lengths $\ell_{1,\dots,7} \text{ m}^{-1} = 0.949, 0.374, 1.75, 1.59, 0.868, 0.786, \text{ and } 0.438$. Each vertex (black circle) is a T-junction obeying Kirchhoff's law, i.e., Neumann boundary conditions.

The measuring frequency range of the experiment is from 0.1 GHz to 18 GHz, the number of points is 64001, and the IF-bandwidth is 1 kHz. The measurement starts with an initial length of $\ell_\varphi = 0.2981$ m, and then every measurement we increase the length by $\Delta\ell$ using a phase shifter attached to a stepper motor. After 401 measurements, the final length of ℓ_φ is 0.3422 m, and we have collected 401 realizations of spectrum $S_{11}(k, \ell_\varphi)$ with different length of ℓ_φ .

3.4.2 Spectra Transformation

In this subsection, we will describe the data processing in our experiment, that transforming measured spectra with constant length ℓ_φ into spectra with constant phase φ , which was introduced in subsection 3.2.2. Such transformations are important for varying the coupling of the system. Thus here, we will also compute the transmission coefficients of the spectra after the transformations to demonstrate couplings are indeed changed.

First, we show spectra with constant length ℓ_φ , see Fig. 3.10 (a), which is the reflection intensity $|S_{11}|^2$ in a gray scale map. We can observe that $|S_{11}|^2$ is maximal on the lines given by $2k\ell_\varphi = n\pi$ ($n \in \mathbb{N}^+$), where n is an odd number, and one of them is indicated by the cyan dotted line ($n = 21$). This property can be understood by detailing the effect of the coupling T-junction. The bond ℓ_φ will reflect the wave

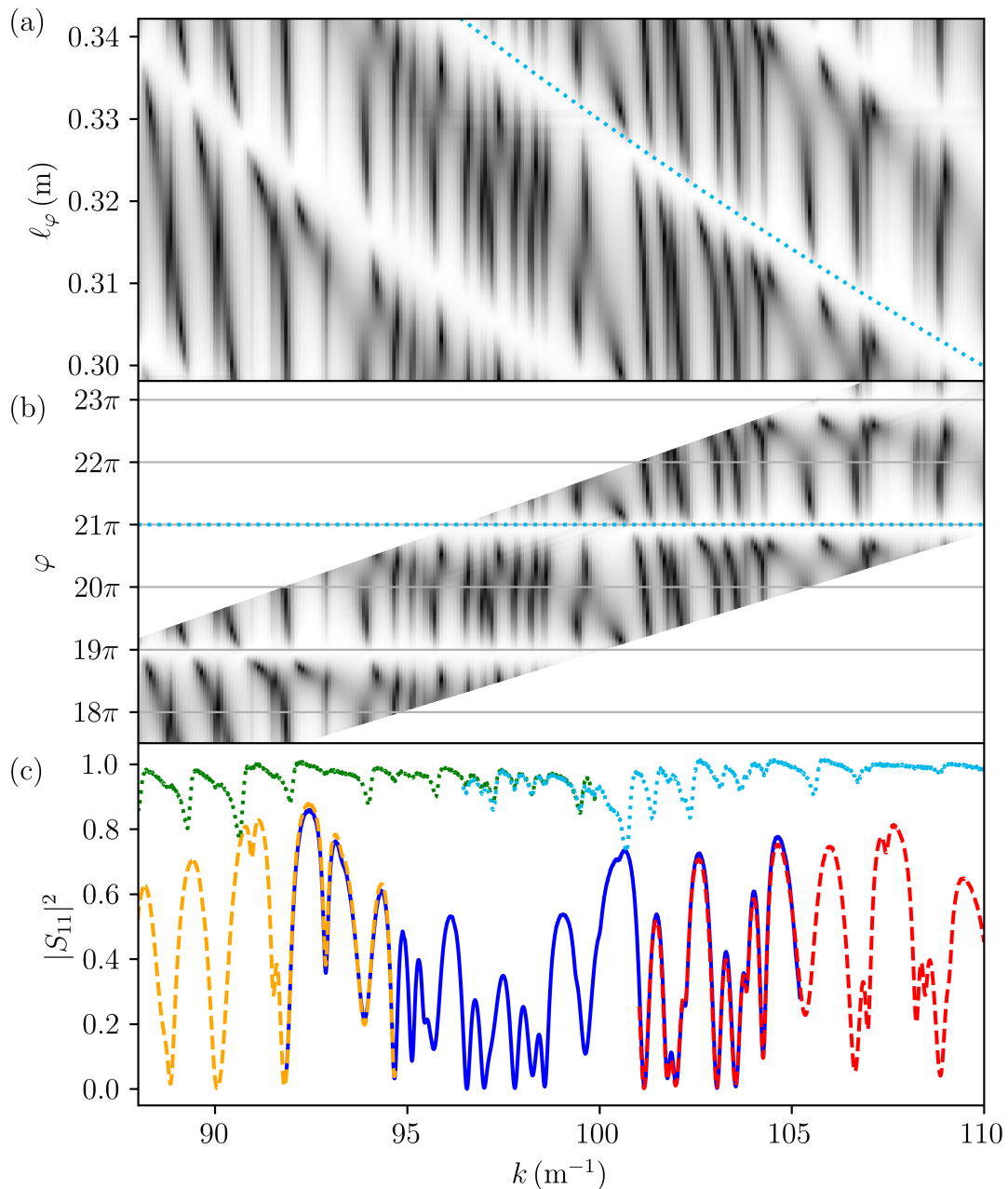


Figure 3.10: (a) Reflection $|S_{11}|^2$ in dependence of wavenumber k for constant l_φ in a gray scale, where black corresponds to 0 and white to 1 in a linear scale. The measurements for different l_φ are stacked onto each other. The cyan dotted line indicates the condition, where the phase $\varphi = 2kl_\varphi$ induced by l_φ is equivalent to 21π . (b) The same data but now rearranged to constant φ using Eq. (3.42). (c) Superposition of the reflection spectra shown in (b) along the lines $\varphi = n\pi$ for $n = 18$ (dashed orange), 19π (dotted green), 20π (solid blue), 21π (dotted cyan), and 22π (dashed red). Odd n values correspond to Neumann, even n values to Dirichlet boundary conditions at the coupling T-junction.

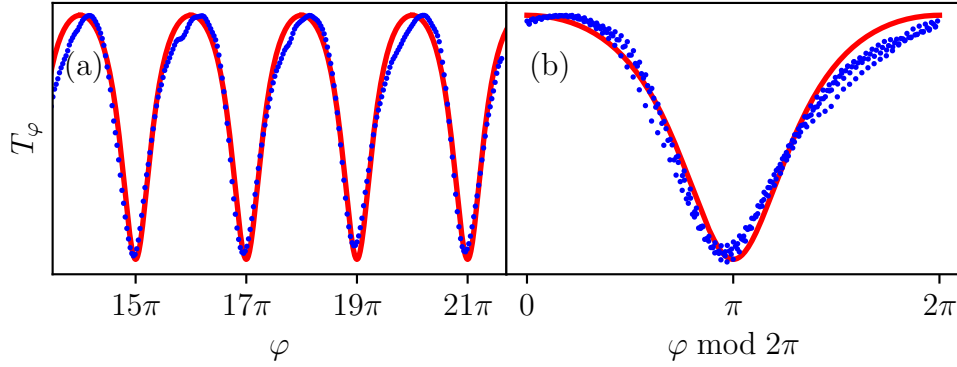


Figure 3.11: (a) Transmission coefficients T_φ as a function of φ from 13.5π to 21.7π , The blue dots have been obtained from $1 - |\langle S_{11}(k, \varphi) \rangle_k|^2$ and the red line corresponds to Eq. (3.39). (b) T_φ plotted over $\varphi \bmod 2\pi$ to highlight periodicity, using the same data from (a).

with amplitude $r_\varphi = \exp(i\varphi)$ to the vertex 0, where

$$\varphi = 2k\ell_\varphi. \quad (3.42)$$

For $\varphi = (2n+1)\pi$ the amplitude is inverted ($r_\varphi = -1$) and the wave at vertex 0 has to be zero, thus the incoming wave is totally reflected at vertex 0. This is also related that the coupling strength is zero, so for this condition we have a closed graph with Dirichlet condition at vertex 0. For $\varphi = 2n\pi$ the wave is propagating through the vertex without any scattering, thus we have a perfectly matched condition for vertex 0 with Neumann boundary conditions.

Then, we show spectra with constant φ , see Fig. 3.10 (b). The transformation uses Eq. (3.42), and has been specified in subsection 3.2.2 and Fig. 3.2. The empty triangular parts in the upper left and lower right present the fact that the length variation of ℓ_φ is limited. The same technique has been used to realize graphs with GSE symmetry [Reh16, Reh18, Lu20, Lawni24]. In Fig. 3.10 (c), the reflection spectra for the integer π values for constant $\varphi = n\pi$ are combined. For even n the resonances have large imaginary parts, and for odd n they are small. For odd n there should be a perfect reflection of 1, which is not the case as we neglected effects of absorption in the bond ℓ_φ , leading to a reduction of $|r_\varphi|^2 < 1$. Note, that in the regimes where contributions from different n overlap the spectra are nicely matching illustrating the precision of the experimental setup.

Finally, we can compute the transmission coefficients of the different φ spectra, reflecting whether they correspond to different couplings. In Fig. 3.11 (a) and (b), the blue dots correspond to the experimental transmission coefficients $T_\varphi = 1 - |\langle S_{11}(k, \varphi) \rangle_k|^2$, where $\langle \cdot \rangle_k$ denotes an average over the measured wave number for constant φ . Also in the figure, the transmission strengths T_φ computed according to the Eq. (3.39) are shown by the red solid lines, and we find a good agreement between them. With these different coupled spectra, we can extract resonances from them. In next subsection 3.4.3, we investigate the behavior of the resonances as a function of the coupling.

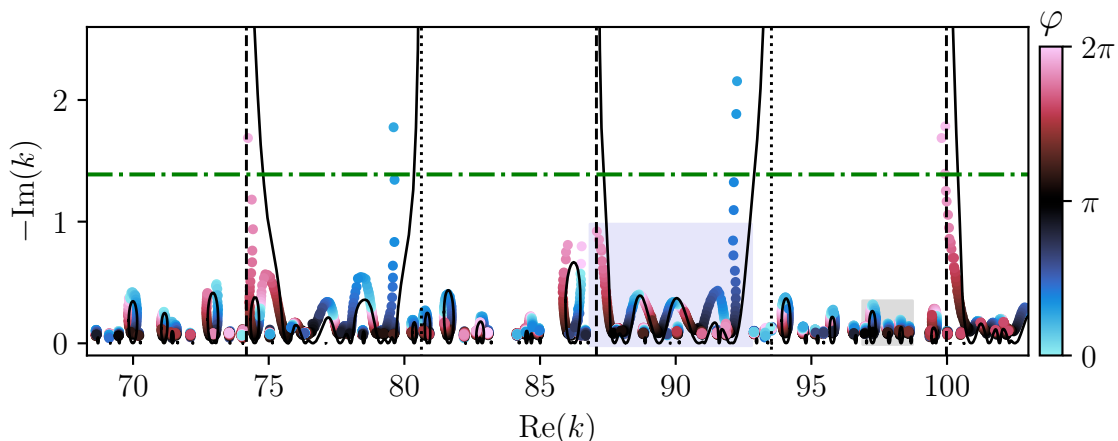


Figure 3.12: The colored circle display the poles extracted from the experimental data by harmonic inversion. The color of the circle indicates the φ value of the measured spectra (value see colorbar). The solid black lines correspond to poles calculated via numeric simulation not including absorption. The dotted and dashed vertical lines correspond to $(n+1/4)k_d$ and $(n+3/4)k_d$ where $k_d = \pi/\ell_d \approx 12.90 \text{ m}^{-1}$, respectively. The dashed dotted green line is indicating $\log(3/\ell_{min})$.

3.4.3 Experimental Findings

Since we are interested in the resonances of the tetrahedral graph, and in the previous subsection we have obtained spectra with constant phase φ , here by harmonic inversion technique [Kuh08], we can extract the corresponding resonances from these spectra. Note, that sometimes the extraction may be difficult if the resonance is not fully visible in the constant phase spectrum at a phase due to distortion after the transformation. Also, experimentally there is a limit to resolve the resonances using the harmonic inversion, which in this example is at about $-\text{Im}(k) = 1.5 \text{ m}^{-1}$. This is in the spirit of fractal Weyl law where the counting of resonances in open systems is restricted to a finite strip below the real axis [Non05, Pot12].

In Fig. 3.12 we present the resonances extracted from the experimentally measured reflection $S_{11}(k, \varphi)$ in the complex k -plane by colored circles, . The colors of the circles indicates the phase values of the spectra used to extract the resonances, where the colorbar on the right indicates their relation. The resonances show two distinct behaviors within different wavenumber ranges. From $(n+1/4)k_d$ (dotted line) to $(n+3/4)k_d$ (dashed line), $k_d = \pi/\ell_d \approx 12.90 \text{ m}^{-1}$, only loops are observed. From $(n+3/4)k_d$ (dashed line) to $(n+5/4)k_d$ (dashed line), the resonance exhibits a continuous behavior with some additional small loop structures. Somewhat more peculiarly, we find that when approaching $\varphi \rightarrow 2\pi^- \cong 0^-$ (red dots), some resonances become very broad, their $-\text{Im}(k)$ value becomes relatively large, and there is a tendency that they are moving to the top of the complex plane, which occurs at $(n+3/4)k_d$. Similarly, for $\varphi \rightarrow 0^+$ (blue dots), we also observe this phenomenon, but at this time these broad resonances are close to $(n+1/4)k_d$. In fact, these resonances correspond to superradiant states disappearing in the continuum whenever the perfect matching condition holds, i.e., whenever the vertex is balanced.

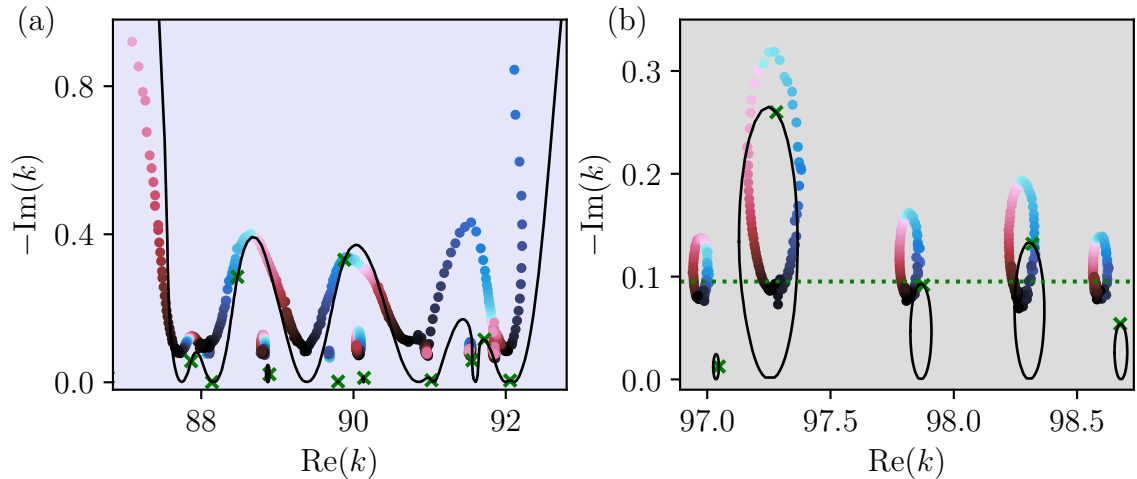


Figure 3.13: (a) and (b) are enlargements of the correspondingly marked regions in Fig 3.12. The green crosses correspond to the resonances of the open tetrahedral graph without dangling bond ℓ_d . The dotted horizontal line shows the estimated global absorption $\gamma = 0.0952 \text{ m}^{-1}$.

This superradiant state disappears regularly (determined by ℓ_d), thus leading to a reduction in the total length, $L \rightarrow L - \ell_d$, and Weyl's law no longer holds.

In addition, we have calculated the poles from the bond scattering matrix of the graph, see subsection 3.1.3, where the bond ℓ_φ was taken into account assuming a zero length and a fixed phase φ . Note, that due to experimental absorption or errors in the measurement of the electrical length of the cable, the numerical simulation may not be accurate enough. Here, in order to achieve good agreement between the numerical and the experimental results, we applied an optimization procedure to better estimate the actual length of each bond. Specifically, we can numerically calculate the complex reflection of the graph based on the known electrical length, the connectivity of the network, and the frequency points used in the measurement. Then, by minimizing the difference between the measured and simulated complex reflections, we can obtain the bonds ℓ_i and global absorption γ that are closer to the measured ones. The variation of the ℓ_i was of the order of a few mm, within the experimental uncertainty of the cable lengths. A complex wave number $k = k_r + i\gamma$ was used in the numerical calculations to take care of absorption, resulting in $\gamma = 0.0952 \text{ m}^{-1}$. The solid lines correspond to this simulation for $\gamma = 0$, i.e., without including absorption. The shift in the imaginary part of the loops observed in Fig. 3.13 (b) corresponds to the global absorption obtained (horizontal dotted line).

In the numerical results, when $\varphi = \pi$, according to Eq. (3.39), $T_a = 0$. We verified that the poles calculated from the scattering matrix touch the real axis, and they correspond to the eigenvalues of the closed graph with a Dirichlet condition at vertex 0. When $\varphi = 0$, $T_a = 1$, and the graph is fully open. The resonances obtained from this spectrum correspond to the one of the tetrahedron without the dangling bond, which are shown as crosses in Figs. 3.13 (a) and (b). When φ is varying from $\pi \rightarrow 2\pi \rightarrow \pi$, we observe two behaviors. The first behavior is a line

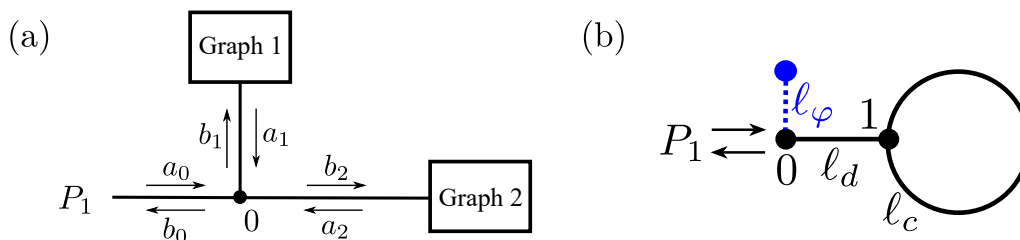


Figure 3.14: (a) Sketch of a setup, which is based on a T-junction, and the T-junction is attached to port P_1 and two separate graphs (Graph 1 and Graph 2). (b) Sketch of the lasso graph with T-junction to vary the coupling.

connecting two different kind of superradiant states, as shown in Fig. 3.13 (a). The second one is the loop structure, see Figs. 3.13 (b), the resonance width increases, then attains the maximum and decreases. Similar features are found in case of resonance trapping but there the resonances do not return to its original real parts $\text{Re}(k)$ [Mag99, Per98, Per00, Rot01, Kot04, Stö02].

Note, that the maximal $-\text{Im}(k)$ for the individual resonance is not necessarily reached for $\varphi = 0$ or 2π , but can be higher at other φ values. Also, in Fig. 3.12, we show the horizontal dashed dotted line, which corresponds to $-\text{Im}(k) = \log(3/\ell_{\min})$, where ℓ_{\min} is the minimal length in the tetrahedron and 3 is the maximal number of bonds connected to a vertex, a prediction obtained in [Ing22] for non-balanced graphs with Neumann boundary condition only. In our case, all resonances apart from the ones with large width are below this limit.

In this subsection, we study the resonance dynamics in the same complex plane by varying the parameter φ and observe the emergence of superradiance and non-Weyl. Note that since non-Weyl here is related to a balanced vertex, its behavior should be universal. In addition to the example of tetrahedral graph, we can also use simpler graphs to understand this phenomenon or even solve it analytically, such as the lasso graph, which consists of a dangling bond and a ring. In next section 3.5, we will study lasso graphs numerically and experimentally.

3.5 Non-Weyl Lasso Graphs

3.5.1 Analytical Description

Before we discuss the lasso graph, we first look at the setup in Fig. 3.14 (a). This setup is based on a T-junction, where one port of the T-junction is connected to channel P_1 , and the other two ports are connected to two arbitrary graphs. For this T-junction, one can describe the incoming and outgoing waves based on the scattering matrix (see also Eq. (3.35))

$$\frac{1}{3} \begin{pmatrix} -1 & 2 & 2 \\ 2 & -1 & 2 \\ 2 & 2 & -1 \end{pmatrix} \begin{pmatrix} a_0 \\ a_1 \\ a_2 \end{pmatrix} = \begin{pmatrix} b_0 \\ b_1 \\ b_2 \end{pmatrix}. \quad (3.43)$$

For arbitrary graph 1 and 2, their scattering matrices can be described as

$$S_1 = \frac{b_1}{a_1}, \quad S_2 = \frac{b_2}{a_2}. \quad (3.44)$$

Substituting Eq. (3.44) into Eq. (3.43), we get

$$S = \frac{b_0}{a_0} = -\frac{3S_1S_2 + S_1 + S_2 - 1}{S_1S_2 - S_1 - S_2 - 3}. \quad (3.45)$$

The above equation shows that for the setup of Fig. 3.14 (a), as long as we know the scattering matrices of graphs 1 and 2, we can solve for the reflections at P_1 .

Then in our actual example, see Fig. 3.14 (b), we can define the blue part of the sketch consisting of bond ℓ_φ and open terminal as graph 1, and define the lasso graph consisting of dangling bond ℓ_d and ring bond ℓ_c as graph 2. The scattering matrices of the two graphs can be given by the following description:

$$S_1 = e^{i\varphi}, \quad \varphi = 2k\ell_\varphi, \quad (3.46)$$

and

$$S_2 = \varepsilon_d^2 \frac{3\varepsilon_c - 1}{3 - \varepsilon_c}, \quad \varepsilon_d = e^{ik\ell_d}, \quad \varepsilon_c = e^{ik\ell_c}. \quad (3.47)$$

Substituting in Eqs. (3.46) and (3.47) to Eq. (3.45), one gets

$$S = \frac{(-9e^{i\varphi} - 3)\varepsilon_d^2\varepsilon_c + (3e^{i\varphi} + 1)\varepsilon_d^2 + (e^{i\varphi} - 1)\varepsilon_c - 3e^{i\varphi} + 3}{(3e^{i\varphi} - 3)\varepsilon_d^2\varepsilon_c + (-e^{i\varphi} + 1)\varepsilon_d^2 + (e^{i\varphi} + 3)\varepsilon_c - 3e^{i\varphi} - 9}. \quad (3.48)$$

Now, if we are looking for the pole of the scattering matrix, that is k that satisfies the Eq. (3.48) with zero denominator. In next subsection 3.5.2, we will compare the results for poles from numerical simulation using the bond scattering matrix introduced in subsection 3.1.3 with those obtained by solving Eq. (3.48) with zero denominator.

3.5.2 Numerical Findings

The lasso graph we choose here is analogous to the tetrahedral graph in section 3.4. By keeping ℓ_c of the lasso graph the same as the total length of the tetrahedral graph (excluding ℓ_d and ℓ_φ), and letting ℓ_d here the same as ℓ_d of the tetrahedral graph, see Fig. 3.9 and 3.14 (b), we get a lasso graph with the same total length as the tetrahedral graph.

In Fig. 3.15, we show numerical results for the resonances of the lasso graph with different φ . For comparison, the display range in the complex plane is consistent with Fig. 3.12. Clearly, both figures show similar behavior. The dotted lines at $(n + 1/4)k_d$ and the dashed lines at $(n + 3/4)k_d$ have the same positions as the ones in Fig. 3.12, due to $k_d = \pi/\ell_d$. We observe loop structures from dotted lines to dashed lines and a continuous transition from dashed lines to dotted lines. The dynamics of the poles in the lasso graph have simpler shapes than the dynamics of the resonances in the tetrahedral graph, which is related to the complexity of

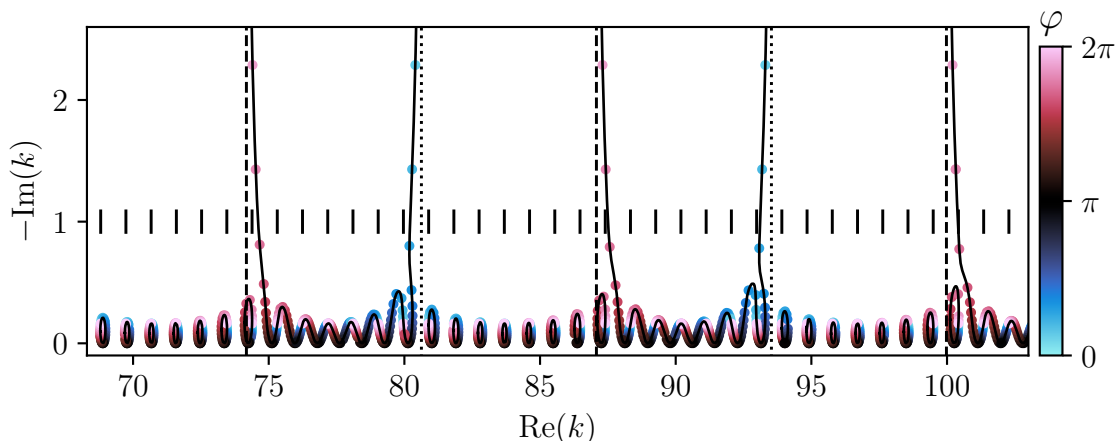


Figure 3.15: The colored circles show the poles extracted from the numerical data of lasso graph, where ℓ_c is equal to the total length of the tetrahedron graph in Fig. 3.9 excluding ℓ_d and ℓ_φ , and ℓ_d of this lasso graph is equal to ℓ_d in Fig. 3.9. The solid black lines correspond to poles calculated via Eq. (3.48). The display range of the complex plane, dotted and dashed vertical lines in the figure are the same as Fig 3.12. Vertical slabs indicate BICs, $k_c = 2n\pi/\ell_c$.

the graph structure. As φ approaches 0^+ (blue dots) or $2\pi^- \equiv 0^-$ (red dots), the resonances are significantly broadened, corresponding to superradiance. These superradiant resonances will escape to or come back from infinity at the same $Re(k)$ as in the tetrahedral graph, and can be predicted by dotted lines and dashed lines. When $\varphi = 0$ or 2π , no resonances can be extracted in numerical calculations. For this reason, the lasso graph no longer satisfies Weyl's law.

In the previous subsection 3.5.1, we provided an analytical description of the lasso graph and derived the scattering matrix for the setup shown in Fig. 3.14 (b), as described in Eq. (3.48). Using this equation, we can compute the poles of the scattering matrix, and the solid lines in Fig. 3.15 represent these calculations. Our results show good agreement between the analytical predictions and the numerical results, demonstrating the accuracy of the analytical description. The vertical slabs indicate eigenvalues of the circular structure related to $k_c = 2n\pi/\ell_c$, which do not couple to the dangling bond thus neither to the environment, which correspond to BICs [Gnu13, Wan24b]. Note that we cannot extract BICs from the scattering matrix, so if one wants to compare the number of resonances in the lasso graph with the predictions of Weyl's law, one should additionally include the number of these BICs. In subsections 3.5.3 and 3.5.4, we will study another example of a lasso graph with $\ell_c/\ell_d = 4$.

3.5.3 Rational Lasso Graphs

Here we will further study the analytical description of the lasso graph, in particular the case where the ratio of ℓ_c to ℓ_d is an integer. We can express the $e^{i\varphi}$ term in

Eq. (3.48) by trigonometric functions:

$$e^{i\varphi} = -\frac{1 - i \cot \frac{\varphi}{2}}{1 + i \cot \frac{\varphi}{2}}, \quad (3.49)$$

then the condition for the poles of the scattering matrix, that is the denominator of Eq. (3.48) is 0, simplifies to

$$\varepsilon_d^2 \frac{3\varepsilon_c - 1}{3 - \varepsilon_c} + 1 = -2i \cot \frac{\varphi}{2}. \quad (3.50)$$

For a number of situations Eq. (3.50) allows for an analytic solution, in particular for a lasso graph with a ratio of $\ell_c/\ell_d = 4$. One can simplify the result using $\varepsilon_c = \varepsilon_d^4$ to

$$\frac{3\varepsilon_d^6 - \varepsilon_d^4 - \varepsilon_d^2 + 3}{\varepsilon_d^4 - 3} = 2i \cot \frac{\varphi}{2} \quad (3.51)$$

whence follows that the real part of the left hand side must be zero,

$$\text{Re} \left(\frac{3\varepsilon_d^6 - \varepsilon_d^4 - \varepsilon_d^2 + 3}{\varepsilon_d^4 - 3} \right) = 0 \quad (3.52)$$

and defines which resonance exist for arbitrary φ values, whereas the imaginary part of Eq. (3.51) precises for which φ the resonance is found. Introducing $z = \varepsilon_d^2 = x + iy$ and defining $\rho = |\varepsilon_d^2|^2 = x^2 + y^2$ and $x = \text{Re}(\varepsilon_d^2)$ a quadratic equation for $\rho(x)$ is obtained

$$\rho^2 (3x - 1) + \rho (26x - 6) - 36x^3 + 12x^2 + 3x - 9 = 0 \quad (3.53)$$

with the solution

$$\rho_{1,2} = \frac{-13x \mp 2\sqrt{x(27x^3 - 18x^2 + 43x - 12)} + 3}{3x - 1}. \quad (3.54)$$

Only solutions for $\rho \in R^+$ are allowed giving rise to have either zero, one, or two resonances, in accordance with the observation. In next subsection 3.5.4, we will study the lasso graph with $\ell_c/\ell_d = 4$ by microwave experiment.

3.5.4 Experimental Findings

Here we will perform experimental investigations on the lasso graph, following the experimental descriptions in section 3.4. In our experimental setup, the lasso graph is configured with a dangling bond of length $\ell_d = 0.307$ m and a ring graph approximately four times this length, giving $\ell_c = 4\ell_d$. We choose this ratio because in this case, loops and continues lines appear alternately and present the simplest pattern. Note, that although our goal is to achieve this ratio accurately, slight deviations are inevitable due to experimental limitations.

In Fig. 3.16, we show experimental results on the resonance of the lasso graph with $\ell_c/\ell_d = 4$. For comparison, the display range in the complex plane is consistent with Figs. 3.12 and 3.15. In this particular experimental setting, the unique ratio between the dangling bond ℓ_d and the ring graph ℓ_c yields periodicity of the

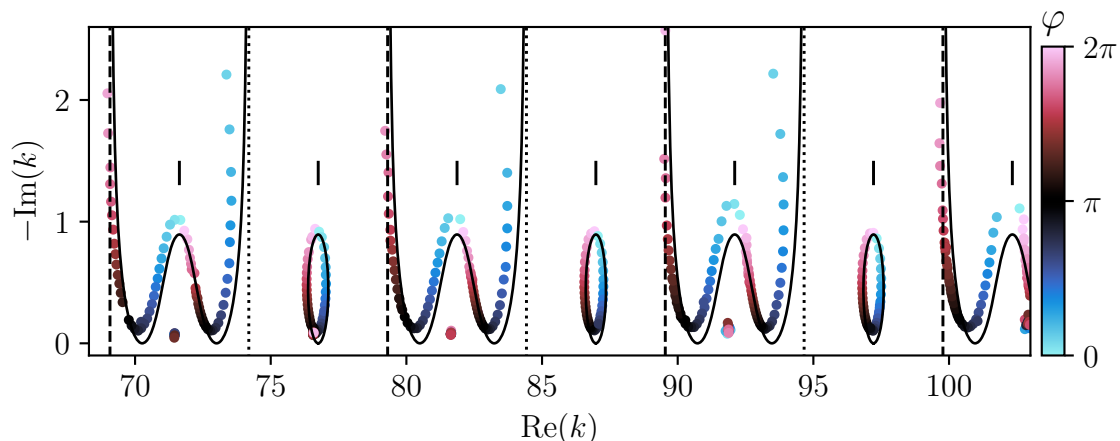


Figure 3.16: Similar to the description in Fig. 3.15, the colored circles in this figure represent the experimental results, obtained from a lasso graph with ratio $\ell_c/\ell_d = 4$, where $\ell_d = 0.307 m$. Vertical slabs indicate BICs, $k_c = 2n\pi/\ell_c$.

structures. We observe that transitions from dotted lines to dashed lines form only a single loop structure, while transitions from dashed lines back to dotted lines present a continuous transition resembling the “W”-shape structure. Note, that since the ℓ_d and total length of this examples are different from the examples in Figs. 3.12 and 3.15, there is no direct correspondence between their dashed or dotted lines, and the number of resonance in each wavenumber interval. Nevertheless, the superradiance phenomenon can still be observed. Specifically, the resonance goes to infinity as φ approaches 0^+ (indicated by the blue dots) or $2\pi^- \equiv 0^-$ (indicated by the red dots).

Here we also present the poles computed from Eq. (3.54), see the black solid line in Fig. 3.16, which presents the solution where $\text{Im}(k) = \log(\rho)/2$ and the real part of k is determined by $\text{Re}(k) = \text{Re}(\log(\varepsilon_d)/2i)$. We found that these theoretical predictions are in good agreement with experimental results, demonstrating the accuracy of our analytical model. As discussed in subsection 3.5.2, the structure of the ring graph inherently supports BICs, see the vertical slabs in the figure, which in theory cannot be extracted from the scattering matrix. However, due to the imperfections of the experimental setup, these BICs are transformed into observable resonances, which appear as small loop structures in the complex plane. These features can be seen in the vicinity of $\text{Re}(k) \approx 71.4, 76.5, 81.5, 91.9$.

In this subsection, we experimentally study the lasso graph satisfies $\ell_c/\ell_d = 4$ and find that loops and continues lines appear alternately, indicating that the relatively simple lasso graph can reflect the complex tetrahedral graph in studying the dynamic behavior of poles. In next subsection 3.5.5, we will look at other configurations of the lasso graph.

3.5.5 Other Examples

Here we experimentally study two lasso graphs, one with the most natural ratio $\ell_c/\ell_d = 1$ and the other with $\ell_c/\ell_d = 3/2$.

First, we look at the case where $\ell_c = \ell_d = 0.4386 m$, as shown in Fig. 3.17 (a).

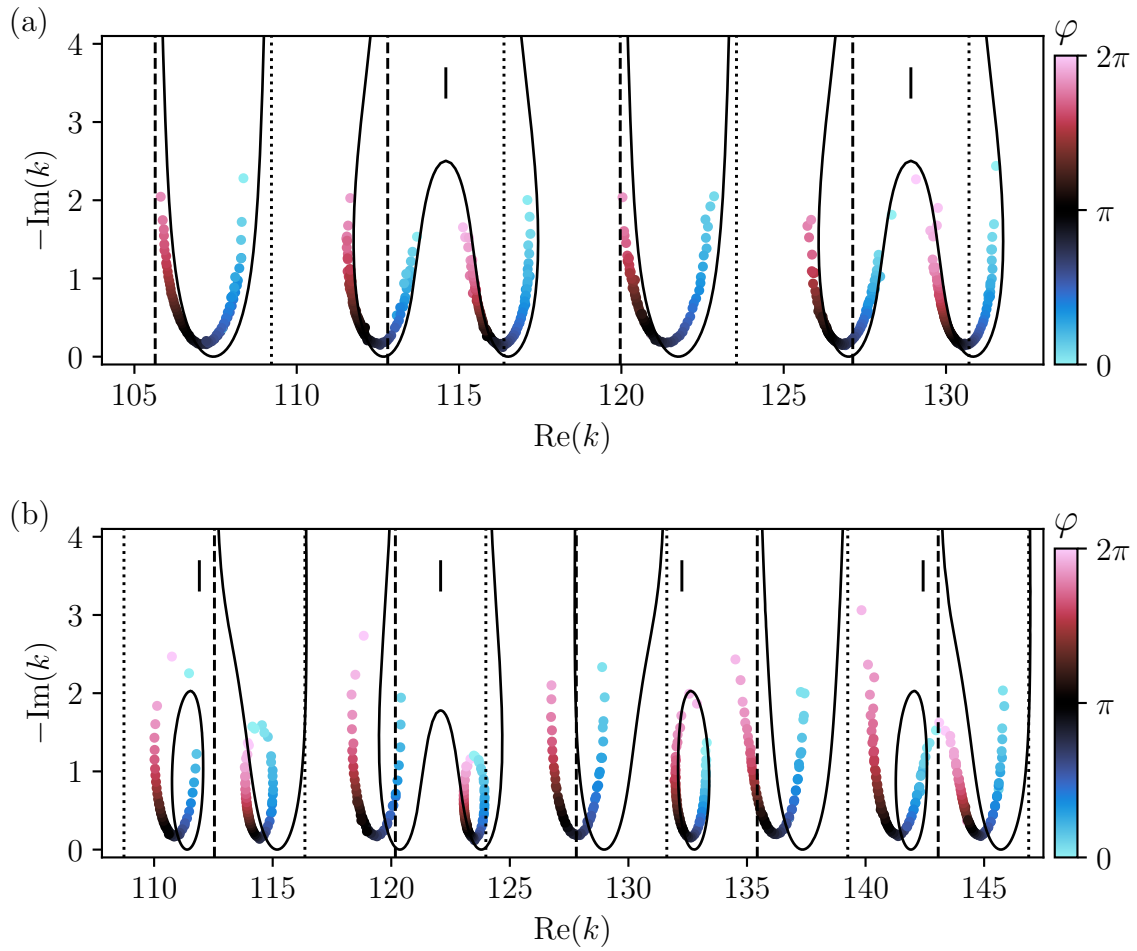


Figure 3.17: Similar to the description in Fig. 3.15, these colored circles represent the experimental results from lasso graphs. For (a), $\ell_c = \ell_d = 0.4386 \text{ m}$. For (b), $\ell_c/\ell_d = 3/2$, where $\ell_d = 0.4117 \text{ m}$.

Similar to the case of $\ell_c/\ell_d = 4$, the periodicity of the structure is immediately observed, and here the dynamics of resonances from dotted lines to dashed lines no longer show loop structures. Instead, they appear as the left or right part of a widened “W” structure. And from dashed lines to dotted lines, the dynamics sometimes show a “U”-shape or a “∩”-shape structure. Note, that when φ approaching 0 or 2π the resonances may appear outside of dashed/dotted vertical lines. These structures are different from anything previously observed in other lasso graphs. By calculating the poles from Eq. (3.50), see the black line in Fig. 3.17 (a), we confirm good agreement between experimental and numerical results. The broad resonances and the transition of the superradiant states are still existing, since the only essential ingredients for this behavior is a graph coupled via a dangling bond to the continuum. In this case, the BIC will only exist in the middle of the “W” structure, see the black vertical slabs in Fig. 3.17 (a).

Next, we discuss the case where $\ell_c/\ell_d = 3/2$, and $\ell_d = 0.4117\text{m}$. The numerical simulations, shown as black solid lines in Fig. 3.17 (b), highlight a range of dynamic resonant behaviors, including loops, “U”-shaped, and “W”-shaped structures, which arise from the specific ratio of ℓ_c to ℓ_d . In this case, although more obscure, the periodicity of the structure exists. The experimental results, shown as colored circles, display deviations from the predictions. For example, in the $\text{Re}(k)$ range of 120 to 150, a “W” structure is expected to appear, but the experimental results show only two isolated loop structures. This discrepancy may be caused by the imperfect length of the coaxial cables used in the experiment. For the rest, the lasso graph with this ratio explains why non-Weyl behavior occurs, which is due to the resonance undergoing a superradiant transition and going to infinity.

3.6 Conclusion

In section 3.1, we introduce quantum graphs and how to compute their spectra and scattering matrices. The two main numerical methods are vertex secular equation and bond scattering matrix. The former takes less time in numerical calculations, while the latter allows describing quantum graphs as close as possible to the experimental situation, e.g. it allows taking into account phases in the bonds, which is exactly what we want to describe in our thesis.

The section 3.2 introduces the definition and components of microwave networks, such as coaxial cables, T-junctions, and phase shifters. It details how to obtain a set of spectra with different lengths through phase shifter experiments and transform them into spectra with different phases. It also introduces a method based on a T-junction. By varying the phase of one port, it changes the boundary condition at the vertex, thus indirectly changing the coupling. These two are important approaches in this thesis.

In section 3.3, we mainly introduce Weyl’s law in quantum graphs and give some examples. For closed graphs, they satisfy Weyl’s law. But when the graph is opened, it may not be the case. We give some examples of Weyl and non-Weyl graphs, and show their counting function of resonances, and compare them with the predictions. We also give the motivation for this chapter, we want to know why Weyl’s law fails in a graph with balanced vertex.

In section 3.4, we discuss the experimental study based on tetrahedral network. First, we introduce the microwave setup and use the method of modeling varied phase. Then, in the experiment, we obtain the spectra with constant phase in a large wavenumber interval. By harmonic inversion, we extract the resonances from these spectra and plot them in the same complex plane as a function of coupling. While going from closed (Dirichlet) to fully open (Neumann) graph, we see resonances escaping via a superradiant transition leading to the non-Weyl behavior when the coupling to the outside is balanced. The open tetrahedral graph displays a rich parametric dynamic of the resonances in the complex plane presenting loops, regions of connected resonances and resonances approaching infinite imaginary parts.

In section 3.5, we study the lasso graphs, since many features are already present in these simple graphs. First, we analytically derive the reflection of the lasso graph using the scattering theory of graph. Then, we numerically study the lasso graph whose dangling bond and total length are consistent with the tetrahedral graph. We find that its resonances behave as a function of phase very similarly to those shown in the tetrahedral graph and exhibit rich parametric dynamics, including superradiance that could lead to non-Weyl phenomena. Then, we analytically derive the lasso graph satisfying $l_c/l_d = 4$ and perform experiments and comparisons, finding good agreement. By observing the dynamics of resonances in the complex plane, we find that they have loop and continuous line structures. We also show experimental results for $l_c/l_d = 1$ and $l_c/l_d = 3/2$ lasso graphs, which exhibit different resonance dynamics due to their special length ratios.

Chapter 4

Superradiant Coherent Perfect Absorber

Contents

4.1	Theoretical Background and Motivation	54
4.1.1	<i>Chaotic Reverberation Chamber (CRC)</i>	54
4.1.2	<i>Description of Global and Local Losses</i>	54
4.1.3	<i>Coherent Perfect Absorption (CPA)</i>	57
4.1.4	<i>Motivation</i>	58
4.2	Experimental Realization of CPA	59
4.2.1	<i>Experimental Setup</i>	59
4.2.2	<i>System Coupling</i>	60
4.2.3	<i>System Loss</i>	62
4.2.4	<i>CPA Optimization</i>	64
4.2.5	<i>Extraction of Zeros</i>	65
4.3	Average Antenna Transmission with Global Loss . .	69
4.3.1	<i>Theoretical Description</i>	69
4.3.2	<i>Numerical Verification</i>	70
4.3.3	<i>Parameter Relation for Constant Antenna Transmission</i>	72
4.4	Numerical Simulation of Zeros	73
4.4.1	<i>Under and Perfect Coupling</i>	73
4.4.2	<i>Over Coupling</i>	75
4.5	Stirring generated Zeros Dynamics	80
4.5.1	<i>Experimental Findings</i>	80
4.5.2	<i>Numerical Findings</i>	82
4.6	CPA in CRC as Temperature Sensor	83
4.7	Conclusion	85

4.1 Theoretical Background and Motivation

4.1.1 Chaotic Reverberation Chamber (CRC)

Reverberation chambers (RCs) are widely used in electromagnetic compatibility applications or antenna characterizations [Kil02, War03]. A fully functional RC includes a metallic shielded room with finite conductivity, featuring a stirring device, antennas, a device under test (DUT), and various utilities such as lamps, tables, and supports. The characterizations and tests conducted within an RC rely on statistical quantities, with theoretical evaluations based on isotropic, homogeneous, and depolarized fields as a function of device and measurement antenna positions and the stirring. However, at low frequencies, this assumption may not be valid. Therefore, the operational frequency of an RC must always exceed a critical threshold known as the lowest usable frequency (LUF) [Hil98]. In this chapter, all presented experimental measurements are well above the LUF.

Then, chaotic reverberation chamber (CRC) was proposed [Gro14a], adopting concepts from wave chaos. It has been noted that at quite low frequencies, most modes in chaotic cavities exhibit Gaussian statistics [Stö99]. The CRC displays universal spatial and spectral statistics in the low frequency range, meaning that it can naturally fulfill the above mentioned fields requirements, and can be used as a well-operating RC without the use of any spatial stirring [Gro14c, Gro15, Gro16].

Traditionally, CRCs are designed with irregular geometries, often based on parallelogram cavities by modifying their geometry, e.g., adding spherical lids or hemispheres [Gro14c, Gro15, Gro16, Bas17, Kuh17, Oub20]. These cavities typically include mechanically movable elements known as stirrers, which enhance chaoticity and enable ensemble averaging through mode stirring [Hil09].

More recently, Gros et al. explored a novel construction method for CRCs by utilizing reconfigurable intelligent surfaces (RIS) [Gro20]. This technology allows for local tuning of cavity boundary conditions. The chaoticity of these systems was confirmed by comparing the experimental wave field distribution to RMT predictions for wave chaotic systems, with the mean modal overlap being the critical experimental parameter [Gro20]. Further research indicated that RIS could rapidly produce numerous uncorrelated field realizations even in small chambers, broadening the potential applications of CRCs in fields such as computational imaging [Sle16], antenna characterization [Kil04], and testing wireless devices [SH10].

In this chapter, we take a CRC equipped with three RISs as the study object. In the next subsection 4.1.2, we will address the non-negligible losses in CRCs and discuss how they can be introduced into the effective Hamiltonian approach.

4.1.2 Description of Global and Local Losses

In CRC microwave experiments, energy dissipation is unavoidable and comes from various sources, such as antenna coupling, metal wall absorption, and localized interactions with objects. Consequently, to accurately model systems experiencing energy dissipation, the effective Hamiltonian approach (introduced in subsection 2.3.2) must be revised to include these diverse dissipation mechanisms.

4.1. Theoretical Background and Motivation

(i) The first type comes from the channels such as antennas or waveguides. These components connect the system to external environments via M_a scattering channels, resulting in energy leakage from the cavity to the coaxial feed. This phenomenon is captured in the term W within Eq. (2.32). For clarity in this thesis, we refer to this phenomenon as energy decay.

(ii) The second type involves Ohmic loss at the cavity boundaries. These boundaries can be viewed as distributed M_b fictitious channels, each with *ad hoc* impedance. Typically, in a 3D cavity, M_b is approximately $2\pi\mathcal{A}/\lambda^2$, where \mathcal{A} is the wall area and λ is the wavelength, applicable in the limit $\mathcal{A} \gg \lambda^2$ [Gro14a]. Additionally, we also account for losses from the cavity's internal volume, in our case the air, which are generally negligible compared to the other ones. Here we refer to this type of dissipation as global loss.

(iii) The third type arises from localized absorption on the boundary, distinct from the second type. This dissipation is quantified by M_c channels, emphasizing point dissipation of energy within the system. It may include elements like non-measuring antennas or surface irregularities. These are not as finely distributed as the wavelength and may involve the DUT or other aspects not fully captured by the second type of dissipation mechanism. It can also be considered as the contribution from non-measuring ports in a system [Fyo17, Fyo19, Pic19]. In the thesis, we refer to this as local loss.

To refine our model, we decompose the coupling matrix W into three components: $\{A, B, C\}$, corresponding to coupling through M_a antennas, M_b “bulk” and M_c “contour” channels. This decomposition is crucial for modeling different dissipation behaviors effectively. Accordingly, the total channel count is defined as $M_{\text{tot}} = M_a + M_b + M_c$, leading to a $N \times M_{\text{tot}}$ dimensional coupling matrix and a corresponding $M_{\text{tot}} \times M_{\text{tot}}$ scattering matrix:

$$S_{\text{tot}} = \begin{pmatrix} \mathbb{I}_{M_a} - iA^\dagger GA & -iA^\dagger GB & -iA^\dagger GC \\ -iB^\dagger GA & \mathbb{I}_{M_b} - iB^\dagger GB & -iB^\dagger GC \\ -iC^\dagger GA & -iC^\dagger GB & \mathbb{I}_{M_c} - iC^\dagger GC \end{pmatrix}, \quad (4.1)$$

where

$$G = \frac{1}{E - H_{\text{eff}}}, \quad H_{\text{eff}} = H_0 - \frac{i}{2} (AA^\dagger + BB^\dagger + CC^\dagger). \quad (4.2)$$

If the system is chaotic (such as CRC), H_0 is from GOE to describe the statistical properties of the quantities of interest. The coupling matrices A , B and C are composed of independent Gaussian-distributed random vectors with zero means and specific covariance, similar to those described in Eq. (2.39) or as referenced in [Sav06].

The total M_{tot} -dimensional scattering matrix (4.1) is constructed unitary by assuming a Hermitian H_0 . However, experimentally, one can only access the $M_a \times M_a$ subblock of the total scattering matrix S_{tot} given by

$$S = \mathbb{I}_{M_a} - iA^\dagger \frac{1}{E - H_{\text{eff}}} A, \quad (4.3)$$

which is notably subunitary.

In cases where the number of weakly coupled fictitious channels is large, particularly at the high frequency limit where $M_b \rightarrow \infty$ and their mean coupling strength diminishes $\langle T_b \rangle \rightarrow 0$, the product $M_b \langle T_b \rangle \equiv 2\pi\Gamma_{\text{hom}}/\Delta$ remains constant [Sav03, Sav06]. For a large number of fictitious channels, the central limit theorem enables us to neglect the fluctuations in widths caused by Ohmic losses at the walls, thus allowing for the isolation of the homogeneous term Γ_{hom} . With these assumptions, the effective Hamiltonian simplifies to

$$H_{\text{eff}} = H_0 - \frac{i}{2} (AA^\dagger + \Gamma_{\text{hom}} \mathbb{I}_N + CC^\dagger) . \quad (4.4)$$

Note, that in the literature [Fyo17, Che21b], Γ_{hom} could also be included in complex energy: $E \rightarrow E + \frac{i}{2}\Gamma_{\text{hom}}$. Taking the determinant of Eq. (4.3) according to Eq. (2.34), one finds:

$$\begin{aligned} \det S(E) &= \frac{\det (E - H_0 - \frac{i}{2}AA^\dagger + \frac{i}{2}\Gamma_{\text{hom}} \mathbb{I}_N + \frac{i}{2}CC^\dagger)}{\det (E - H_0 + \frac{i}{2}AA^\dagger + \frac{i}{2}\Gamma_{\text{hom}} \mathbb{I}_N + \frac{i}{2}CC^\dagger)} \\ &= \frac{\det (E - \tilde{H}_{\text{eff}})}{\det (E - H_{\text{eff}})} = \prod_{n=1}^N \frac{E - z_n}{E - \mathcal{E}_n} . \end{aligned} \quad (4.5)$$

In the above expression, the poles \mathcal{E}_n of the scattering matrix are complex eigenvalues of the non-Hermitian Hamiltonian H_{eff} , whereas the zeros z_n are complex eigenvalues of the non-Hermitian Hamiltonian

$$\tilde{H}_{\text{eff}} = H_0 - \frac{i}{2} (-AA^\dagger + \Gamma_{\text{hom}} \mathbb{I}_N + CC^\dagger) . \quad (4.6)$$

If we assume both uniform and localized absorption are absent (i.e., $\Gamma_{\text{hom}} = CC^\dagger = 0$), the description (4.3) of the scattering matrix will reduce to Eqs. (2.32) and (2.33), where the poles and zeros of the system will be complex conjugates of each other, as illustrated in Eq. (2.36), exhibiting symmetry along the real axis as a consequence of scattering matrix unitarity.

In this chapter, we assume that global losses are present ($\Gamma_{\text{hom}} > 0$) while local losses are absent ($CC^\dagger = 0$). This yields the effective Hamiltonian for poles to

$$H_{\text{eff}} = H_0 - \frac{i}{2} (AA^\dagger + \Gamma_{\text{hom}} \mathbb{I}_N) , \quad (4.7)$$

and for zeros to

$$\tilde{H}_{\text{eff}} = H_0 - \frac{i}{2} (-AA^\dagger + \Gamma_{\text{hom}} \mathbb{I}_N) . \quad (4.8)$$

This assumption primarily reflects the dominance of Ohmic losses at the walls over other forms of energy dissipation, a condition encountered in our CRC experiments as detailed in subsection 4.2.3. This scenario implies that all poles and zeros shift downwards by $\Gamma_{\text{hom}}/2$ in the complex plane. Note, that the symmetry is preserved in the system, since global loss only causes a shift effect, and each zero has a corresponding pole. Consequently, if zeros can still be found near the real axis under the influence of strong global loss, investigating these zeros corresponds to identifying

the superradiant poles in the system. In this chapter, we discuss this phenomenon both experimentally and numerically.

However, if $CC^\dagger \neq 0$, the local losses break the symmetry of z_n and \mathcal{E}_n , shifting them in an arbitrary fashion, though on average downwards. This type of local loss will not be included in this chapter, but relevant discussions can be found in [Fyo17, Che21b].

In this subsection, we have introduced the effective Hamiltonian framework for analyzing three types of losses, setting the stage for our detailed examination of scattering behaviors in open lossy systems. Moving forward, the next subsection 4.1.3 will explore the CPA phenomenon. Furthermore, in section 4.3, we will introduce the uniform global loss into in the calculation of average scattering fluctuations, improving the RMT description for lossy chaotic systems.

4.1.3 Coherent Perfect Absorption (CPA)

Perfect absorber (PA), where a device fully absorbs any incident electromagnetic wave, is a significant achievement in optics [Ra'di15]. This occurs when all scattered wave components within the device are absorbed, thereby converting the wave's energy into heat, electrical current, or fluorescence.

The recent development, CPA [Cho10, Bar17], is a special case of perfect absorption, as it is only absorbing perfectly a specific incoming waves. The condition of CPA is given by

$$S\mathbf{a}_{\text{CPA}} = 0, \quad (4.9)$$

where S is the scattering matrix connecting the incoming and outgoing waves, and \mathbf{a}_{CPA} is a non-zero vector of input wave amplitudes.

As can be seen from Eq. (4.9), CPA is realized if all incoming energy is completely absorbed for a specific injection \mathbf{a}_{CPA} , and corresponds to a zero eigenvalue of the scattering matrix on the real frequency axis. It is crucial to distinguish the CPA from a PA where S itself is zero. The CPA specifically leverages destructively interference from coherent radiation to create perfect traps in lossy systems, while the PA primarily focuses on directly reducing the amplitudes of the S parameters to achieve absorption for any incoming wave front.

Of special interest is that CPA can be explained by zeros. Recall the zeros and poles: if the scattering matrix is unitary, they are symmetrically distributed around the axis, see Fig. 2.3. The additional loss makes the scattering matrix subunitary and moves these zeros and poles around in the complex plane, as was discussed in subsection 4.1.2. In Fig. 4.1 the case of adding uniform global loss to a system is depicted by downshifting the zeros and the poles by $\Gamma_{\text{hom}}/2$, with mirror symmetry maintained.

A CPA occurs whenever one zero is sitting at the real E axis, i.e., $z_n = \text{Re}(z_n)$. In fact, this is the exact contrary to what people do when they try to construct lasers, where laser engineers try to move poles of the lower half plane upwards by adding gain to the system. Therefore, this phenomenon of CPA can be associated with a time reversed version of a laser, a so called ‘‘anti-laser’’. This only holds for the laser at threshold as thereafter non-linear effects take over in the laser, whereas the CPA does not exhibit these non-linear effects.

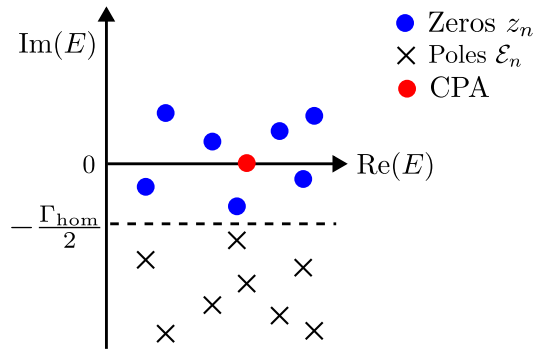


Figure 4.1: Sketch of the zeros and poles of a subunitary scattering matrix in the complex plane, and the shift is due to uniform loss.

CPA phenomenon is not only investigated in many theoretical works [Cho10, Li17, Fyo17], but was also realized in experiments, e.g., in optics [Wan11, Wan21, Slo22, Jia24, Hö24], acoustics [Wei14, Men17] and microwaves [Pic19, Che20, Suw22, dH20, Fra20]. At the very beginning people achieved CPA in highly symmetric structures and excitation conditions [Won16], but nowadays, it is realized also in complex environments [Pic19, Che20, dH20, Fra20, Jia24]. People have studied CPA in experiments breaking time-reversal symmetry [Che20] and in nonlinear systems [Suw22, Wan24a]. There are also works about EP CPA [Wan21, Suw22, Hö24]. It's worth mentioning that the recent tunable environment has also made realizing CPAs much more elegant [Che20, dH20, Fra20]. In this thesis, we will study CPA in CRC by using RIS as a tunable parameter.

4.1.4 Motivation

It now appears that the CRC is an ideal model due to its wave chaos property. Instead of solving an irregular 3D cavity, one can construct an effective Hamiltonian that reflects its statistical properties [Gro14c, Gro14b, Gro16, Gro20, Gro21, Dav21]. Recently, by introducing the new technique of RIS in CRC, we are able to obtain a large number of uncorrelated realizations easily and quickly, which contributes to a more comprehensive study of the statistics of spectral properties.

RISs promote a more efficient realization of CPA in complex scattering environments by tuning the boundary conditions of its programmable meta-atoms, which has been achieved in several works [Fra20, dH21]. However, so far, these CPA experiments rely more on the fact that CPA can be manipulated more conveniently in tunable environments.

In addition, Chen and co-workers introduced a complex generalization of the Wigner time delay to study CPAs [Che21b, Che22b]. However, the absorption in their microwave networks are not large, resulting in both poles or zeros being still relatively isolated.

Moreover, considering CPA as a specific zero and exploring its behavior through the distribution of zeros has not been investigated experimentally. Fortunately, a CRC equipped with RIS offers a platform that can be effectively analyzed using RMT, providing a powerful tool to study zeros from a statistical perspective.

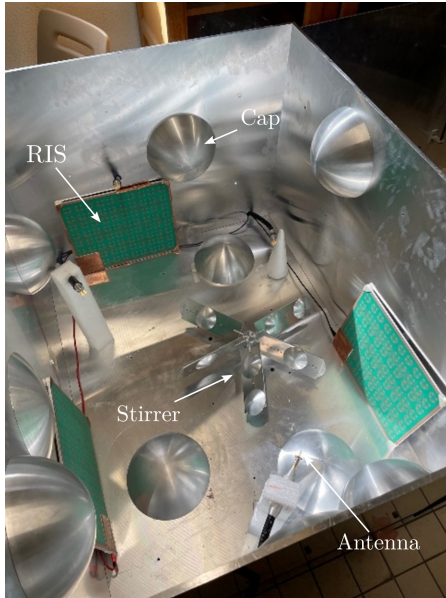


Figure 4.2: Photograph of the CRC which have been removed the top plate.

In this thesis, we aim to explore why CPAs/zeros occur near the real axis in the strong overlap regime. First in section 4.2, we will realize CPAs experimentally and obtain the distribution of zeros. Then in section 4.4, we try to build a corresponding model to describe our experimental findings. Finally, in sections 4.5 and 4.6, we study the sensitivity of the CPAs to external perturbations.

4.2 Experimental Realization of CPA

4.2.1 Experimental Setup

The experimental setup consists of an aluminum CRC with dimensions of $100\text{ cm} \times 77\text{ cm} \times 62\text{ cm}$ (see Fig. 4.2), which has already been used in [Kuh17, Oub18, Oub20] to study statistics of reflection and transmission and estimate the number of independent samples. Fourteen spherical caps are mounted on the cavity walls to reduce parallel surface to suppress bouncing ball modes [Gro14c]: eight caps each with a height of 8.5 cm and six caps with a height of 3 cm. The effective volume of the cavity is 0.4629 m^3 , which will be used later to calculate the mean level spacing.

Three RISs (fabricated by Greenerwave) are positioned along the cavity walls, see Fig. 4.2, which operate in the frequency range of 5 – 5.5 GHz. In total there are 456 pixels that can be electronically configured to mimic Dirichlet and Neumann boundary conditions by independently controlling the bias voltage of a diode, inducing a relative π phase shift in the reflected electric field [Kai14]. Thus, RISs offer 2^{456} distinct configurations, enabling unique wave reflection patterns for each setting. Configuration commands to RISs are relayed through a USB connection from a computer.

A metallic stirrer equipped with five paddles is installed at the base of the chamber, see Fig. 4.2, and can be manipulated via computer commands to a step motor,

allowing rotation to any specified angle. In section 4.5, we will use the stirrer to apply perturbations to the system.

A four-port vector network analyzer (VNA, Keysight E5071C), not shown in Fig. 4.2, is connected to 4 monopole antennas ($l = 15$ mm) via small holes (2 mm radius) through 8 mm thick side walls, enabling the measurement of a 4×4 scattering matrix. In the measurement, the coaxial cables are not placed in the CRC as shown in Fig. 4.2, and they only injected into the cavity by about 3 cm, including the antennas. In subsection 4.2.2, we will show that we can modify the change in coupling by changing the antenna to different lengths. The calibration of VNA is carried out through electronic calibration kit and the plane of calibration of the VNA is where the coaxial cables are attached to the antennas.

To monitor the environmental conditions within the room, two temperature and humidity sensors of differing accuracies are employed. The first sensor, a DHT22 (Grove), offers a temperature resolution of 0.1°C and an accuracy of 0.5°C . The second, an SHT35 (Grove), provides a higher resolution of 0.01°C and an accuracy of 0.1°C . Six sensors are strategically placed on the top surface of the cavity to minimize measurement noise. These sensors are interfaced with an Arduino, enabling temperature and humidity data to be queried remotely from a computer via command. The dynamics of zeros in response to temperature changes are studied in two laboratory rooms. One room lacks temperature control, with temperature variations naturally occurring due to weather conditions. The other room is equipped with an air conditioner, allowing for a rough manual temperature adjustment, and has a better temperature stability over time. In section 4.6, we investigate the CPAs behavior on temperature and show that it can act as a temperature sensor.

4.2.2 System Coupling

In our microwave experiment, the scattering matrix contains important information about the CRC system, such as coupling and loss, and in this and next subsections we will describe how to extract these parameters.

First we discuss coupling. Our objective is to enhance the interaction between the external environment and the CRC, this is done by adjusting the length of the monopole antennas. In our experiments, we use monopole antennas [Bal16], as illustrated in Fig. 4.3 (a). These antennas are designed to efficiently radiate and receive electromagnetic waves when their length l and wavelength λ follow

$$l = \frac{\lambda}{4}. \quad (4.10)$$

Given that measurement frequency spans 5–5.5 GHz, corresponding to the operating frequency of RISs, the antenna length are set to 15 mm to optimize transmission at $f = 5$ GHz (or $\lambda = 60$ mm). In Fig. 4.3 (a), it shows the antennas' reflection measurements in free space, highlighting the reflection dips at 5 GHz. These dips indicate minimal reflection, suggesting good coupling to the free space environment.

To accurately characterize the system's coupling, one needs to install the antennas in the CRC to assess their coupling effects. Referring back to Eq. (2.43), transmission coefficient T_a is important in quantifying coupling, with $T_a \rightarrow 0$ indi-

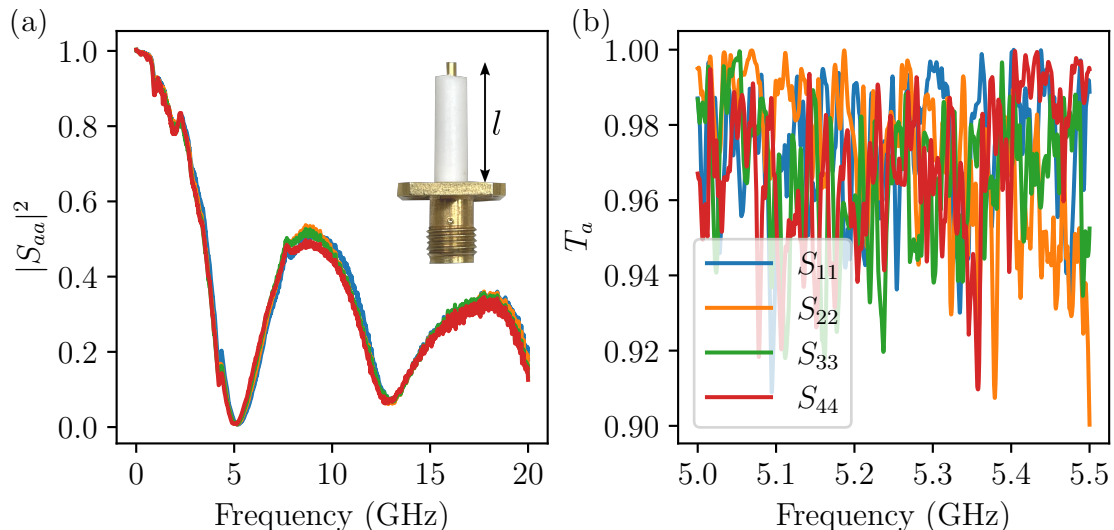


Figure 4.3: (a) The reflections of the antennas with length of 15 mm measured in free space, the colors represent 4 measured antennas. A monopole antenna used in the experiment is shown in the upper left. (b) Transmission coefficient T_a calculated from $1 - |\langle S_{aa} \rangle|^2$, where S_{aa} is measured from random configurations of the RISs for antennas' length of 15 mm.

cating nearly closed channels, and $T_a \rightarrow 1$ representing completely open channels. Experimentally, T_a is determined by setting the RISs' pixels to random configurations and averaging the measured scattering matrices $\langle S_{aa} \rangle$. This is previously noted in subsection 4.1.1, that these configurations are uncorrelated, allowing for ensemble averaging to compute T_a .

As illustrated in Fig. 4.3 (b), T_a values derived from various reflections S_{aa} are plotted over the 5–5.5 GHz frequency range for antennas with $l = 15$ mm. The figure shows the fluctuations of T_a . If we average over frequency and the four antennas ($a = 1, 2, 3, 4$), then we get $T_a = 0.97$, which indicates that there is strong coupling in the operating frequency range.

For completeness, T_a values from antennas of other lengths are also presented, see Fig. 4.4. The monotonic behavior observed in the figure can be attributed to the lengths of the monopole antennas, which determine the most effective operating frequency, and none of the other lengths exhibit as strong coupling as the one with $l = 15$ mm.

In this subsection, we have obtained the measured transmission coefficients T_a , which are crucial for determining the coupling parameter κ , as outlined in the effective Hamiltonian model discussed in subsection 2.3.4. However, the relationship between κ and T_a in lossy systems is quite different from the descriptions typically associated with non-lossy systems. To accurately determine the coupling parameter κ and construct an exact RMT model for our CRC system, it is necessary to consider these differences. Therefore, we will explore the relationship between κ and T_a in the context of lossy systems in section 4.3. Here, in subsection 4.2.3, we will look at another crucial experimental observation, the loss of the CRC.

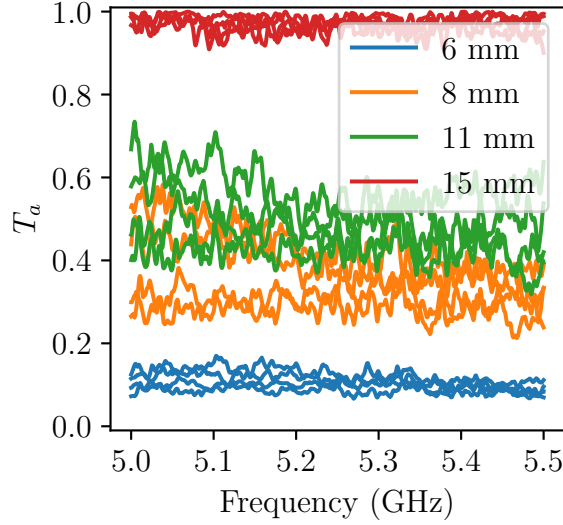


Figure 4.4: Comparison of the T_a with different length of antenna. Each length is represented by four curves, corresponding to reflections from four different channels.

4.2.3 System Loss

Next we discuss loss. As previously noted in subsection 4.1.2, loss is an important parameter in CRC, particularly in realizing CPAs. First, we evaluate the decay rate of its impulse response, represented by $I(t) \sim e^{-\langle \Gamma \rangle t}$.

In Fig. 4.5, the experimental curve $I(t) = \langle |\mathcal{F}^{-1}(S_{ij})|^2 \rangle$ is displayed, where $\langle \cdot \rangle$ denotes average over both RIS configurations and all transmission pairs $i \neq j$. This curve results from the inverse Fourier transformation of 500 random scattering matrix S_{rand} , with their averages smoothing the curve and providing a more precise estimation. By fitting the linear part of the curve on a logarithmic scale, depicted by the orange dashed line in Fig. 4.5, an average width $\langle \Gamma \rangle = 19.67$ MHz is extracted from the experiment. The mean modal overlap d in 3D electromagnetic cavities is determined by average resonance widths $\langle \Gamma \rangle$ and mean frequency spacing Δ_f , following established relationships [Gro14a, Kuh17, Oub20]:

$$d = \frac{\langle \Gamma \rangle}{2\pi\Delta_f}, \quad (4.11)$$

where Δ_f is defined as

$$\Delta_f = \frac{c^3}{8\pi V f^2}, \quad (4.12)$$

where V is the volume of the cavity, c is the speed of light and f is the center of the measured frequency window, reflecting Weyl's law for 3D cavities, which has been discussed in subsection 2.2.2. At $f = 5.25$ GHz, the mean frequency spacing of the system is calculated as $\Delta_f = 84$ kHz. This leads to a mean modal overlap of $d = 37.26$ and a quality factor of $Q = 2\pi f / \langle \Gamma \rangle = 1677$.

In this analysis, it is crucial to distinguish between the quality factor Q and the mean modal overlap d , as they relate differently to the system's loss characteristics. The quality factor Q is most directly associated with the average width of the

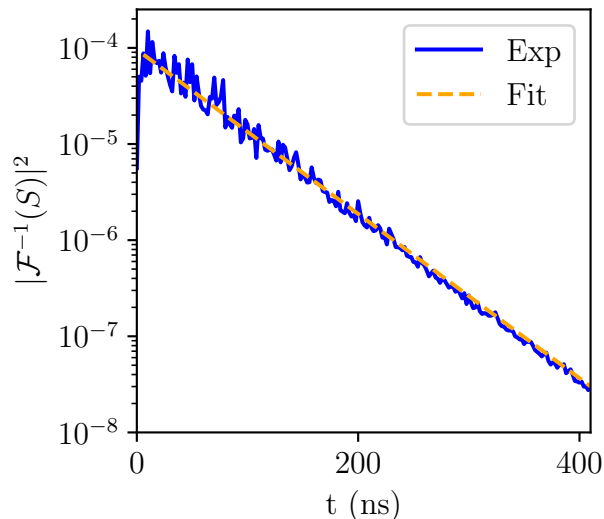


Figure 4.5: The modulus squared of the ensemble-averaged inverse Fourier transform of transmission data, collected with RIS in random configurations. The orange dashed line indicates the linear fit on a logarithmic scale, which is fit with an exponential function $I(t) = \exp(at + b)$, where $a = -0.0197$ and $b = -9.2523$.

resonances $\langle \Gamma \rangle$. This factor primarily measures the energy loss per cycle relative to the stored energy, with lower values indicating higher losses, typically under $Q < 100$ for high-loss systems.

On the other hand, the mean modal overlap d , not only depends on $\langle \Gamma \rangle$ but also on the mean frequency spacing Δ_f , describing the average degree of resonance overlap. This measure is critical for assessing how individual resonances in the system interact and overlap with each other. Unlike Q , a high d value (about 10 or higher) indicates a significant overlap, suggesting a different aspect of system loss.

In this thesis, we primarily consider the system's loss characteristics from the perspective of the mean modal overlap d . It's noteworthy that even with a high d , it is possible to maintain a high quality factor Q . This observation underscores the fact that a system can exhibit extensive resonance interactions while still preserving a considerable amount of energy relative to its losses.

In our experiments, we extracted that $\langle \Gamma \rangle = 19.67$ MHz, which includes all forms of decay: energy decay from real antennas, global loss, and local loss. Importantly, in these CRC experiments, the contribution from antennas is small, thus we assume that the main absorption is from the resistance in the walls, which can be effectively described by global loss Γ_{hom} , as described in subsection 4.1.2. Note that we must distinguish between $\langle \Gamma \rangle$ and Γ_{hom} . $\langle \Gamma \rangle$ comes from the experiment and represents the average width of the resonance, while Γ_{hom} comes from the description of Hamiltonian and represents the global loss parameter without units. Under this assumption, the global loss Γ_{hom} is equated with the normalized averaged width, namely the mean modal overlap, thus $\Gamma_{\text{hom}} = d = 37.26$.

As mentioned in subsection 4.1.2, global loss Γ_{hom} can be incorporated into the effective Hamiltonian. The integration of this subsection bridges the experimental observations of loss with the RMT model, effectively laying a robust foundation for the numerical simulation in section 4.4.

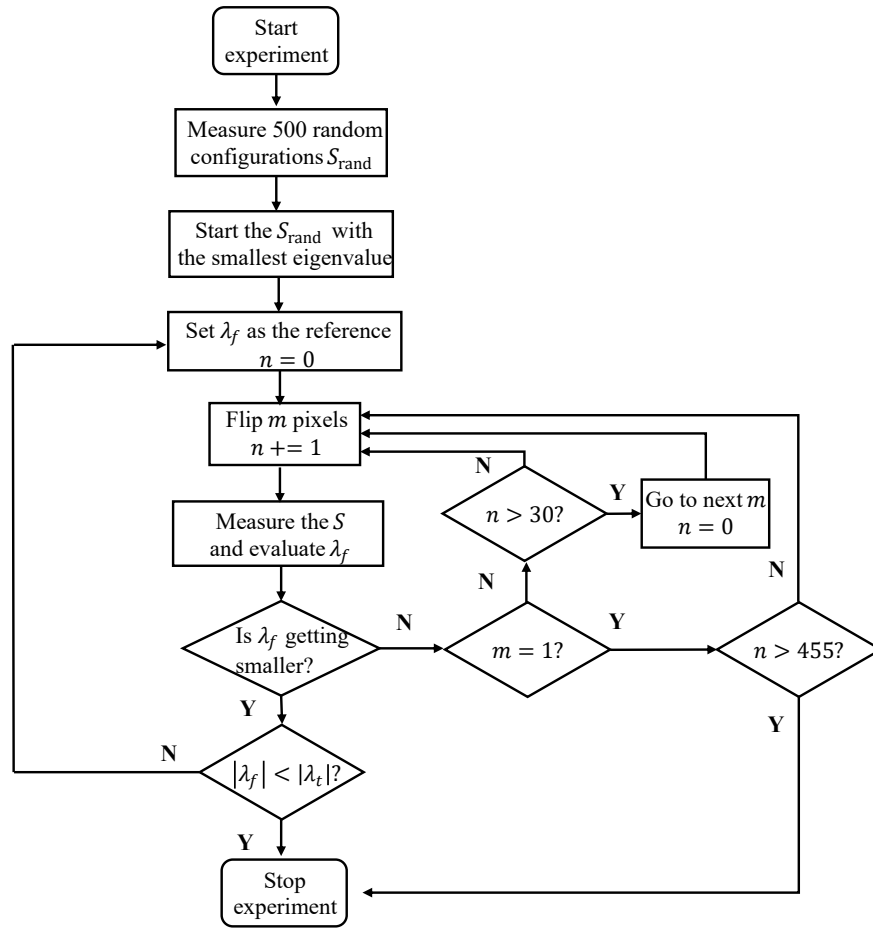


Figure 4.6: Flow chart of the optimization algorithm used to realize CPAs, where m is the number of flipping pixels, n is the counting of measurement with a new m , λ_f is the minimum eigenvalue of scattering matrix, and λ_t is the threshold.

4.2.4 CPA Optimization

Our objective is to find a CPA state at a specific frequency point, f_{CPA} , by employing an iterative optimization algorithm designed to minimize the modulus of eigenvalue of the S matrix [Fra20, dH21]. Initially, we measure 500 random configurations S_{rand} and select the scattering matrix configuration with the smallest eigenvalue λ_f as our starting point. During each iteration, we choose m pixels to flip their states ($0 \rightarrow 1$ or $1 \rightarrow 0$). If this action yields a smaller eigenvalue than the previous one, we keep this configuration as the new reference. The optimization process involves repeatedly flipping another m pixels as the iterations advance. If after n attempts there is no improvement in minimizing the eigenvalue, we conclude that the process has converged for that set of m and proceed to the next value. We define m as a sequence [150, 60, 40, 25, 12, 6] and set $n = 30$. Once all the elements of m have been used, we switch to flipping one pixel at a time. Finally, when all pixels are flipped individually but there is no improvement or when λ_f reaches the threshold λ_t , we considered the optimization has saturated. Here we also provide a flowchart of the optimization algorithm, see Fig. 4.6.

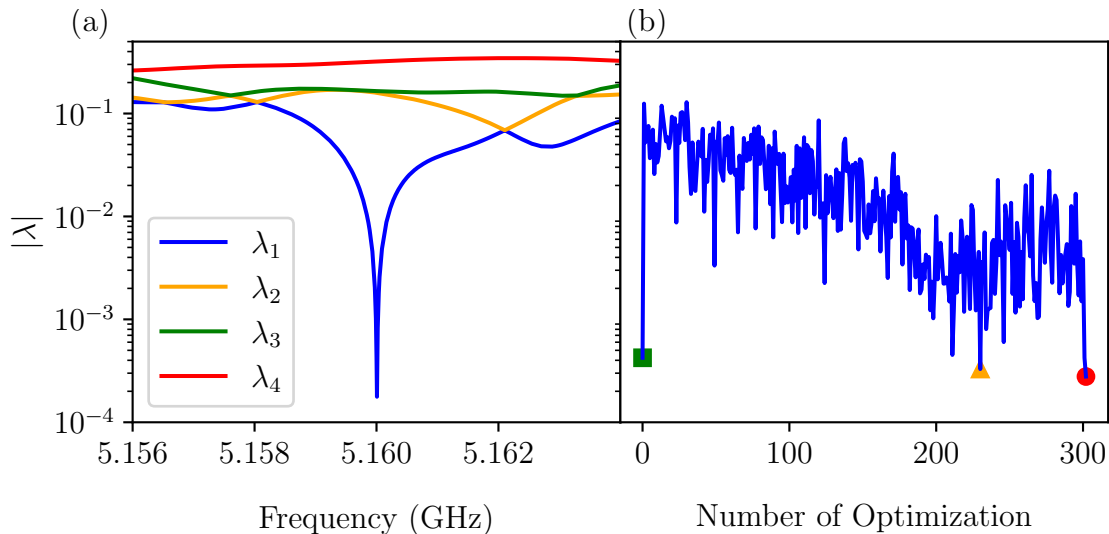


Figure 4.7: (a) An example of the eigenvalues λ_i of S_{CPA} . (b) At f_{CPA} , the eigenvalue λ vary with the number of optimizations. The symbols represent those measurements for which smaller eigenvalues were obtained.

One experimental example of the eigenvalues of S_{CPA} where the system reaches a quasi-CPA state is shown in Fig. 4.7 (a). In the figure we confirm that we can find the smallest eigenvalue λ_{\min} close to 10^{-4} , and around 5.16 GHz the curve has a very sharp dip. We can further visualize this optimization by tracing the evolution of the smallest eigenvalue at frequency point f_{CPA} with the number of optimizations. As we can see in Fig. 4.7 (b), the starting λ has been shown to be a very small value from the selection of S_{rand} , see green square marker. Then, the optimization starts, but most of the configurations lead to larger eigenvalues until the 230-th optimization (orange triangle). The eigenvalue is smaller than at the green square one, so we take the configuration of RISs to and the eigenvalue here, as the new references. Eventually, at the 302-nd optimization, the red circle in the figure, it again refreshes the minimum eigenvalue record as well as reaches the threshold we set, so the optimization terminates. Note, that in the experiments corresponding CPA waveforms are not injected. The above realization of CPA is widely used in this chapter, for example, in section 4.6, where we study the sensitivity of CPA to temperature, it is necessary to first tune the initial state to the quasi-CPA state.

4.2.5 Extraction of Zeros

In this chapter, we are interested in zeros of scattering matrix, so now we will describe how to extract complex zeros from experimental data.

One possibility to extract the zeros is inverse of the scattering matrix in Eq. (4.5), and its determinant can be written as:

$$\det S^{-1}(E) = \prod_{n=1}^N \frac{E - \mathcal{E}_n}{E - z_n}, \quad (4.13)$$

where each zero z_n appears in the denominator, manifesting as a pole in the spec-

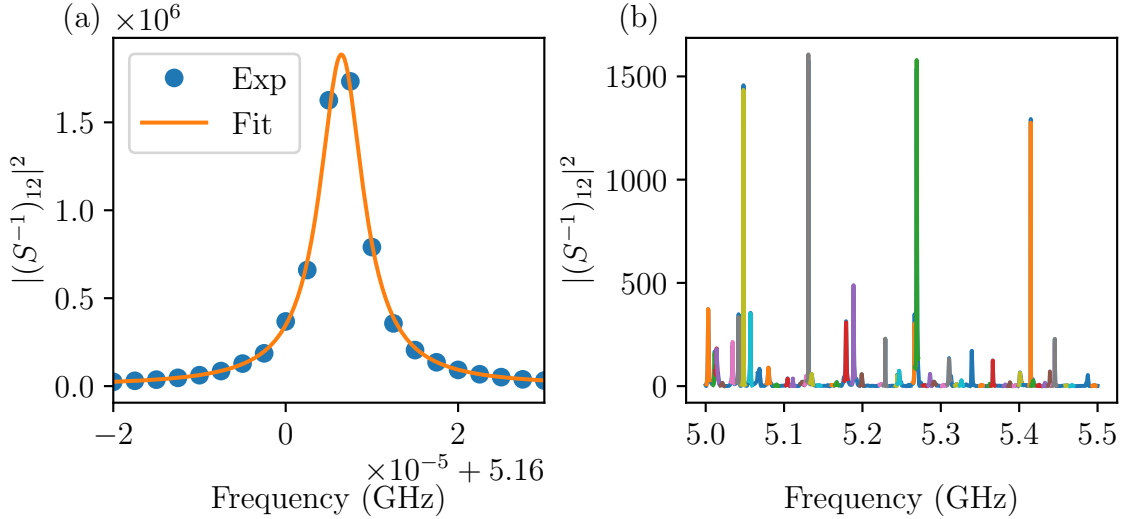


Figure 4.8: (a) An optimized zero is extracted by Lorentz fitting. Dots are experimental measurements and the orange line is the fitted curve. The fitting results give that the real part of the zero is 5.16 GHz, and the imaginary part is 3.07×10^{-6} GHz. (b) The extraction of multiple zeros in full frequency window.

trum of $|(S^{-1})_{12}|^2$. Note, that Eq. (4.13) is represented in terms of the energy E , whereas in the experiments the extraction of the zeros is performed in the frequency domain. To extract these zeros, we utilize the same method applied for poles extraction. In our experiments, Lorentzian fitting is employed to determine the resonance frequency and width of these zeros.

First, we look at a small frequency window, such as the optimized CPA in Fig. 4.7 (a), where the CPA eigenvalue has a dip. However, instead of a dip, the CPA in the spectrum $|(S^{-1})_{12}|^2$ corresponds to a narrow peak, see Fig. 4.8 (a). By applying Lorentzian fitting to this single peak it is trivial to extract the zero (see the orange fit line), we are able to get the information of complex zero and its residue.

Then when the frequency window becomes large, as shown in Fig. 4.8 (b), we can observe numerous peaks in the modulus squared of diagonal element of S_{rand}^{-1} . The idea is actually the same, that we can use a Lorentzian to fit each peak, sequentially. In Fig. 4.8 (b), different colored lines represent the individual fitting results. Nonetheless, a significant challenge remains in extracting zeros with small amplitudes and broad width. Therefore, it is impossible to guarantee that we are able to extract all zeros in the experiment. In the extraction, we impose a threshold $|(S^{-1})_{12}|^2 > 2$ and disregard any peaks falling below this intensity. Current research also explores an alternative method for the extraction of zeros, based on the generalization of Wigner time delay [Che21b].

Here we look at the fitting results even further, in Fig. 4.9, a spectrum segment is presented, where the blue line represents the experimental data, and the yellow, green, and red lines indicate the fit results of a single Lorentzian locally to the experimental data. If we only look at panel (a), we cannot determine the sign difference of the imaginary frequency part between the extracted zeros, but in fact, the yellow and green colors correspond to zeros with negative imaginary parts, while the red line correspond to a zero with positive imaginary parts (see the values in

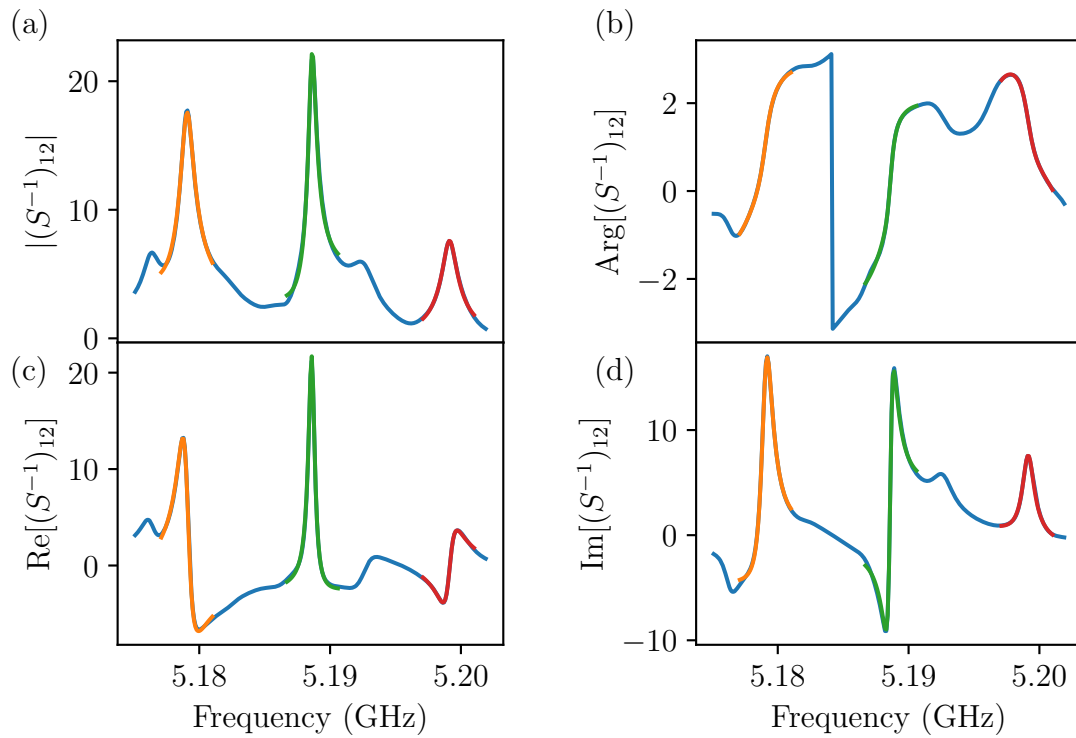


Figure 4.9: An example of fitting zeros by Lorentzian fitting, where the blue lines are from experiment, and the yellow, green, and red lines represent the fitting results of three different zeros. The complex frequency values of these zeros are $5.179 - 0.0005i$ (yellow), $5.189 - 0.0003i$ (green), and $5.199 + 0.0006i$ (red) in GHz. From (a) to (d), they display module, phase, real and imaginary of $(S^{-1})_{12}$.

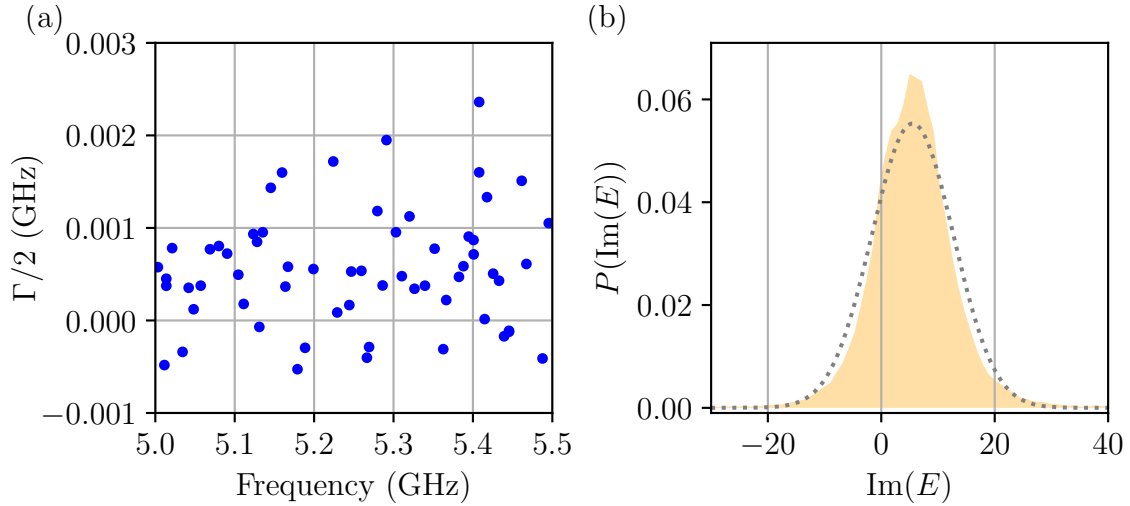


Figure 4.10: (a) The zeros, extracted from the spectrum of Fig. 4.8 (b), are plotted with frequency on the horizontal axis and half of width $\Gamma/2$ on the vertical axis. (b) The distribution of the imaginary part of zeros, normalized by Δ_f , see Eq. (4.12), collected from 500 random realizations. The dotted line is a Gaussian distribution.

the caption of Fig. 4.9). This information is actually contained within the phases, see panel (b), which correspond to ascending and descending curves, respectively. Note, that unlike the zeros, in the case of resonances, they always have a negative imaginary part due to the global loss which makes them shift downward from the real axis. It is also due to the fact that the imaginary part of the zeros in the experiment has both positive and negative parts, making the harmonic inversion method not applicable to extracting the zeros. In panels (c) and (d), the real and imaginary parts of $(S^{-1})_{12}$ are shown, for completeness. Note, that in order to match the experimental data exactly, the Lorentz fit deals with complex data and also takes into account the constant and linear background.

Now the extracted zeros can be drawn in the complex plane, as demonstrated in Fig. 4.10 (a), which exactly are the fitting results of Fig. 4.8 (b). It is quite obvious that zeros appear in the upper and lower parts of the real axis, respectively. To better show the distribution of zeros, we can use RIS to generate uncorrelated S_{rand} , thus collecting as many zeros as possible. To be noticed that the length of the antenna here is $l = 15$ mm, and we also try to extract the zeros of S_{rand} obtained from other lengths of antennas $l = [6, 8, 11]$ mm, but we could not extract even a single zero for them. This highlights the importance of achieving strong coupling of the system and adjusting the antenna length, as mentioned in subsection 4.2.2.

In Fig. 4.10 (b), the distribution of the imaginary part of the zeros after unfolding is presented. Note, that when the Lorentzian peaks have large widths, their extraction becomes difficult. Importantly, we point out that the distribution of experimental zeros is asymmetric, there are more zeros with positive imaginary part. The mean and standard deviation of the distribution $P(\text{Im}(E))$ of experimentally obtained zeros are 5.52 and 7.21, respectively. Using these parameters to construct a Gaussian distribution, as represented by the gray dots in Fig. 4.10 (b), it becomes evident that the experimental results deviate from this Gaussian model.

In this subsection, we find in our experiments, that realizing CPA and extracting zeros in our CRC system are both feasible. Can this phenomenon be described theoretically? It would be nice to have statistical results that explain our experimental results. In theory, assuming local losses can be neglected, the zeros and poles are maintaining the mirror symmetry in the complex plane, and the uniform global loss in CRC should drag all zeros by $\Gamma_{\text{hom}}/2$. This is a global description, but in order to describe it as close as to our experiment results, we need to construct the effective Hamiltonian with the parameters extracted experimentally. In sections 4.3 and 4.4, we will try to find a statistical theoretical description that explains our experimental findings, using effective Hamiltonian approach based on RMT.

4.3 Average Antenna Transmission with Global Loss

4.3.1 Theoretical Description

As described in subsection 2.3.4, the fluctuation properties of the scattering matrix of a chaotic system can be characterized statistically by effective Hamiltonian approach and RMT. However, this description only includes the energy decay due to coupling in an open system. In the thesis, we study CRC systems, thus for a more complete description, other loss mechanisms must be included, as discussed in subsection 4.1.2. Here, we will focus on the global losses, i.e., the Ohmic losses due to the CRC walls.

Given the fact that Eq. (2.41) also applies in the upper part of the complex E -plane [Leh95a], we can introduce the global loss term Γ_{hom} to the complex energy

$$E_c = 0 + i \frac{\Gamma_{\text{hom}}}{2}. \quad (4.14)$$

With $\Gamma_{\text{hom}} = 0$, substituting E_c into Eq. (2.41) yields:

$$g(0) - \frac{1}{g(0)} + \frac{m\kappa}{1 + \kappa g(0)} = 0, \quad (4.15)$$

which aligns with the results from subsection 2.3.4. However, if $\Gamma_{\text{hom}} \neq 0$, substituting E_c into Eq. (2.41), one arrives at

$$g_\gamma - \frac{1}{g_\gamma} + \frac{m\kappa}{1 + \kappa g_\gamma} + \frac{\Gamma_{\text{hom}}}{2\lambda} = 0. \quad (4.16)$$

where $g_\gamma = g(i\Gamma_{\text{hom}}/2)$. Note, that the last term on the left side of the equation does not vanish, significantly affecting the calculations. In cubic Eq. (4.15), one can solve $g(0)$ given only m and κ . However, Γ_{hom} and λ enter the Eq. (4.16), making the solution for g_γ not straightforward.

In the case of κ of the order of unity, the equation for g_γ can be simplified to

$$g_\gamma \simeq -\frac{\Gamma_{\text{hom}}}{4\lambda} + \sqrt{(1 - m) + \frac{\Gamma_{\text{hom}}^2}{16\lambda^2}}. \quad (4.17)$$

Using this approximation, we then can compute the average scattering matrix $\langle S_{aa} \rangle$ by Eq. (2.40), and finally relate it to the transmission coefficients T_a .

This subsection provides both exact and approximate solutions for the average scattering characteristics of lossy systems. It mathematically formulates the relationship between experimentally extractable data, specifically transmission coefficients T_a and global loss Γ_{hom} , and the coupling parameter κ of the RMT model. Note, that although g_γ in Eq. (4.16) can be explicitly solved, the approximation is sufficient for our analysis in this thesis. To validate this, in subsection 4.3.2, we will compare the exact and approximate solutions with numerical simulations by systematically varying the parameters.

4.3.2 Numerical Verification

This subsection focuses on the numerical verification of our estimation about averaging scattering properties for lossy systems. We compare the mathematical formulations with numerical simulations. There are several key parameters that are critical to our analysis: size of the Hamiltonian N , number of channels M , coupling parameter κ , and global loss Γ_{hom} .

We will compare the results for T_a . In exact or approximate formulas, the transmission coefficients T_a are determined by g_γ and κ , where we need to substitute the parameters into Eqs. (2.40), (2.43), (4.16) and (4.17). While in numerical simulations, T_a is computed by constructing the scattering matrix S and then averaging over ensembles and energies close to $E = 0$, as specified in Eqs. (2.43) and (4.3).

In the first comparison, we set $N = 91$, $M = 4$, $\kappa = 0.996$, and $\Gamma_{\text{hom}} = 37.26$. The value of M is consistent with the actual number of antennas used in our experiments, and Γ_{hom} is the global loss of CRC. The N is chosen because we want to test whether the formulas are valid when N is relatively small. The $\kappa = 0.996$ here keeps $T_a = 0.97$ when $N = 91$ and $M = 4$ with $\Gamma_{\text{hom}} = 37.26$. As shown in Fig. 4.11, each panel illustrates the effect of varying a single parameter on the transmission coefficient T_a . In panel (a), as the size of the Hamiltonian N increases, T_a stabilizes, which is expected as the limit $N \rightarrow \infty$. In panel (b), T_a decreases with an increasing number of channels M . Notably, while the exact solution consistently aligns with numerical results, the approximation shows significant deviation as M increases. In panel (c), all results agree as Γ_{hom} increases, with T_a decreasing accordingly, confirming the expected impact of higher global loss on reducing transmission.

For the second comparison, we have adjusted the initial parameter settings to: $N = 91$, $M = 4$, $\kappa = 2.005$, and $\Gamma_{\text{hom}} = 37.26$. The reason for choosing to test the higher κ value is that T_a suggests two potential κ values. In panel (d), as N changes, T_a initially increases, peaks near $N = 40$, and subsequently decreases, indicating a non-monotonic response before stabilizing as N increases. Panel (e) shows an increase in T_a with an increasing number of channels M . And the gap between the approximate and exact solutions becomes more pronounced with higher M . Panel (f) illustrates that changing Γ_{hom} leads to T_a peaking around $\Gamma_{\text{hom}} = 80$ before it decreases, which highlights the complex relationship between global loss and transmission performance.

Lastly, with fixed parameters $M = 4$ and $\Gamma_{\text{hom}} = 37.26$, we examined the impact

4.3. Average Antenna Transmission with Global Loss

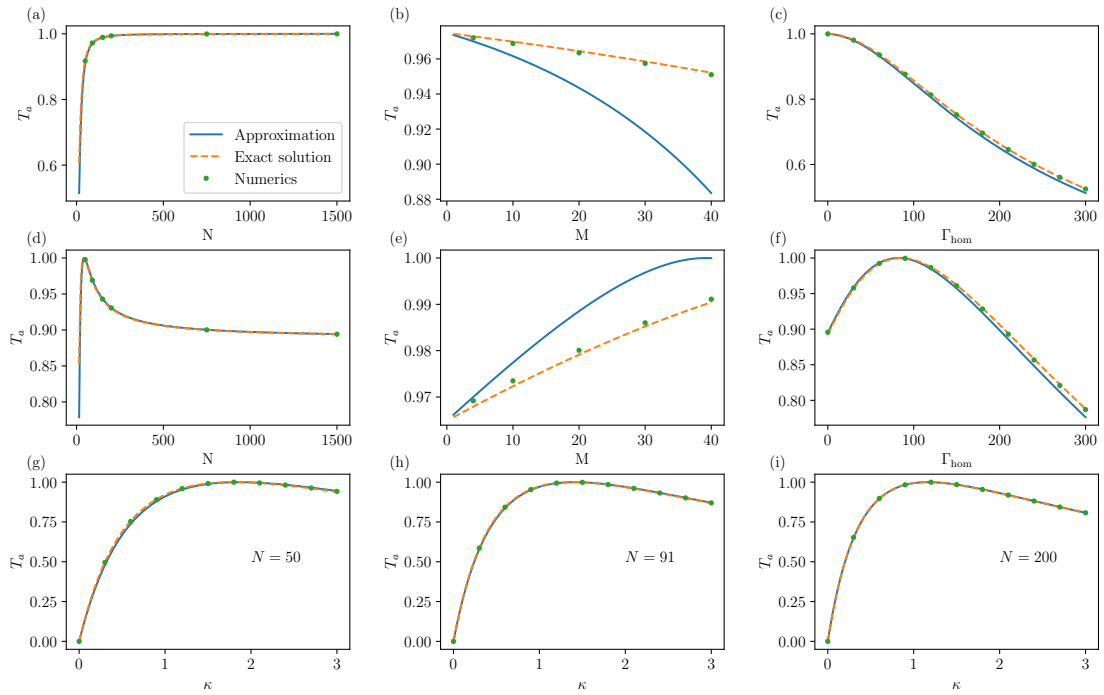


Figure 4.11: Variation of transmission coefficient T_a with parameter adjustments across different panels. Initial parameters for panels (a), (b), and (c) are set to $N = 91$, $M = 4$, $\kappa = 0.996$, and $\Gamma_{\text{hom}} = 37.26$. For panels (d), (e), and (f), only κ has been changed to $\kappa = 2.005$. Each sub-figure varies a single parameter while holding others constant. Panels (g), (h), and (i) feature different values of N and varying κ , with constant $M = 4$ and $\Gamma_{\text{hom}} = 37.26$. Approximations based on Eq. (4.17) are depicted as blue solid lines, exact solutions based on Eq. (4.16) as orange dashed lines, and numerical simulations are represented by green dots.

of varying κ for different values of N . In panel (g) for $N = 50$, panel (h) for $N = 91$, and panel (i) for $N = 200$, we observed that as κ increases, T_a initially increase and then decreases. Both the approximate and exact solutions show good agreement with the numerical simulations.

In this way, we can isolate the effect of each parameter on T_a and thus get a clear picture of their respective effects. The exact solution shows excellent agreement with numerical simulations, affirming the applicability and accuracy of our theoretical framework in practical situations. While the approximate solutions generally perform well, notable discrepancies arise only when increasing M . Note, that in our thesis, M is treated as a fixed value, representing the real number of antennas used in our experiments, thus the approximation remains sufficiently accurate for the purposes of this study. In next subsection 4.3.3, we will take a more practical view of our estimation about averaging scattering properties.

4.3.3 Parameter Relation for Constant Antenna Transmission

After verifying the reliability of our theoretical framework, we now turn our attention to further refining the RMT parameters that describe our experimental system. While some of the parameters have already been determined, $M = 4$ and $\Gamma_{\text{hom}} = 37.26$, the determination of N and κ remains outstanding. Instead of specifying these parameters directly, we first try to establish a relationship between them. This approach benefits from the transmission coefficient $T_a = 0.97$ extracted in subsection 4.2.2. By solving for the objective T_a , we can efficiently compute the relationship between N and κ .

Fig. 4.12 (a) illustrates the relationship between N and κ required to realize a transmission coefficient, $T_a = 0.97$ for fixed parameters $M = 4$ and $\Gamma_{\text{hom}} = 37.26$. It displays the theoretical curves where the solid lines represent approximate solutions and the dashed lines represent exact solutions. It can be seen that for a given N , there are usually two κ solutions. Notably, when N is small, both κ values are greater than 1. As N increases, one κ value remains greater than 1, while the other decreases below 1. The difference between the approximate and exact solutions also decreases as N increases.

To verify the accuracy of the theoretical predictions from Fig. 4.12 (a), we performed numerical simulations. As shown in panel (b), N is varied between 50 and 100, and κ is obtained from Fig. 4.12 (a), with each N corresponding to two values. Two parameters N and κ , combine the established parameters $M = 4$ and $\Gamma_{\text{hom}} = 37.26$ to compute the average scattering matrix $\langle S_{aa} \rangle$, subsequently deriving T_a . The circular markers represent numerical simulations, which show that the results agree very well with the target value $T_a = 0.97$ and that the error decreases as N increases.

Another numerical simulation in Fig. 4.12 (b), N is varied between 50 and 100, but κ is replaced by fixed κ_{eff} , respectively 0.7047 and 1.419, as computed by substituting $T_a = 0.97$ into Eq. (2.44). Clearly, these results marked by triangles deviate significantly from the target value T_a , highlighting that the long-standing $N \rightarrow \infty$ assumption and the use of κ_{eff} to model scattering matrices is inappropriate for our

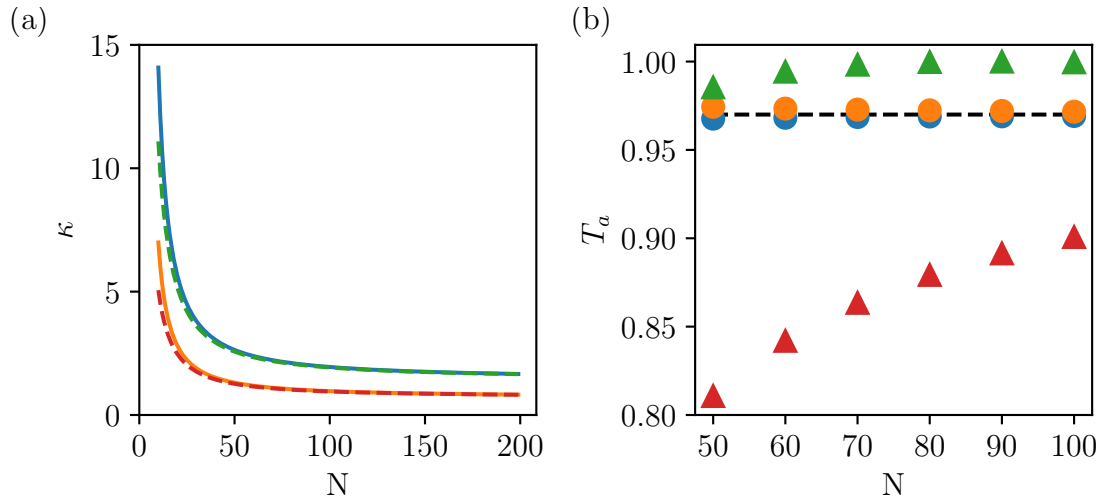


Figure 4.12: (a) Relationship between N and κ required to achieve $T_a = 0.97$ for fixed parameters $M = 4$ and $\Gamma_{\text{hom}} = 37.26$, with approximate (solid lines) and exact (dashed lines) solutions. (b) Comparison of numerical T_a values with the target $T_a = 0.97$ for different N values. Blue and orange circles represent larger and smaller calculated κ values, respectively. Green and red triangles indicate results from larger and smaller κ_{eff} , respectively.

lossy system. This comparison highlights the need for modeling lossy system.

This subsection numerically verifies the feasibility of our theoretical predictions. Although the corresponding numerical parameters are not yet fully determined, since for any N a corresponding κ can always be found to satisfy the objective T_a , we are still searching for a more rigorous approach. One possible way would be to compare experimental and numerical zeros distributions. Thus, in subsection 4.4.1, we will discuss how to obtain the zero distributions by numerical simulation, compare between numerical and experimental results, and try to determine the appropriate N and κ values for the RMT model.

4.4 Numerical Simulation of Zeros

4.4.1 Under and Perfect Coupling

Based on the numerical validation in the previous section, we confirm the reliability of our formulas, both exact and approximate. In this subsection, we present the distributions of numerically obtained zeros that are extracted either directly from the Hamiltonian (4.8) or indirectly extracted from the scattering matrix, both of which are constructed from the parameters of the established relationships. Specifically, the distributions extracted from the scattering matrix will be used as numerical results for comparison with experimental findings.

In Fig. 4.13 (a), we present the distribution of the imaginary parts of zeros calculated from Hamiltonian (4.8). We focus on zeros whose real parts are close to zero, satisfying $|\text{Re}(E)| \leq N/100$, since the semicircle law states that density

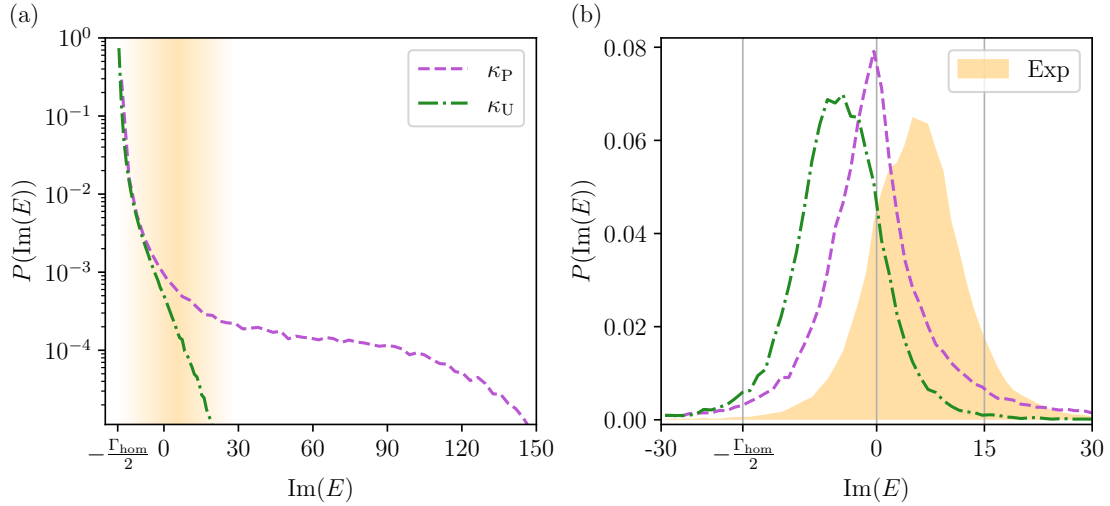


Figure 4.13: (a) Distribution of the imaginary parts of zeros calculated from Hamiltonian for perfect-coupling κ_P (purple dashed line) and under-coupling κ_U (green dashdot line). The stripe (light yellow) marks the range of the imaginary part of the zeros extractable from the experiment, and the shading of the color represents the probability. (b) Comparison of numerical distributions with experimental one for imaginary parts of extracted zeros. The numerical zeros here are extracted the same way as experiment.

of states is constant only near $E = 0$. This figure illustrates two distinct coupling scenarios. The green dashed line represents an under-coupling case with parameters $N = 1500$, $M = 4$, $\kappa_U = 0.7196$, and $\Gamma_{\text{hom}} = 37.26$. The purple dotted line depicts a perfect-coupling scenario with $\kappa_P = 1$, while all other parameters remain identical to those from the green line. Note, that here we have chosen a sufficiently large N , a typical way for numerical studies of quantum chaos problems. The under-coupling κ_U is derived from solving the relationship between the experimentally obtained T_a and three other parameters.

As shown in the figure, the distribution of zeros is shifted by $-\Gamma_{\text{hom}}/2$ due to the global loss, which is due to the downward shift of the zeros in the complex plane. Another notable observation is the decreasing behavior in the distribution, where perfect-coupling allows for a significantly larger width of zeros than the under-coupling case. This phenomenon can be better understood by reviewing the study of superradiance, as shown in Fig. 2.4. The distribution of poles there in the complex plane expands vertically as the coupling of the system goes from weak to strong and then to perfect-coupling. The same is true here for zeros, since the uniform loss only leads to global downshift.

However, it is important to note that the zeros distribution presented in Fig. 4.13 (a) cannot be directly compared with experimental data. In experiments, we are only able to extract those zeros that are located near the real axis. We extracted an average of 45 experimental zeros per realization, which predicts that there should be 5955 zeros in a CRC system in the frequency interval $5 - 5.5$ GHz according to Weyl's law, resulting in a percentage of 0.754%. Whereas the distribution shown here includes all zeros, as they are calculated directly from the Hamiltonian. Obviously, this comparison is not adequate because the experimental conditions inherently

restrict the observable zeros.

A distribution that really needs to be used for comparison would be to extract the zeros of the numerical simulation as the experiment. That is, one should build a scattering matrix from the effective Hamiltonian, invert this scattering matrix in an energy range close to 0, where the density of zeros/poles can be assumed to be constant ($\rho(E) \approx 1$). Then use Lorentzian fits to extract the zeros to finally get the distribution of their imaginary parts, as done for the experiment as well.

In Fig. 4.13 (b), two numerical distributions are compared with the experimental findings. The distribution for the under-coupling case is centered on a negative value, which clearly deviates significantly from the experimental results. This discrepancy suggests that despite careful calculation of the κ_U values by incorporating all parameters and processing the data according to the experimental procedure, the model or the parameters still do not agree with the experimental results. Similarly, for the κ_P case, the distribution does not align with the experimental results. In fact, in the regime of $0 < \kappa < 1$, the probability distribution $P(\text{Im}(E))$ always exhibits a monotonically decaying behavior, resulting in a consistent shift towards the left, see Fig. 4.13 (b). Note, that the figure shows that there are some zeros below $-\Gamma_{\text{hom}}/2$, which is impossible from a theoretical point of view and is due to errors in the fitting during extraction. Nevertheless, in the perfect-coupling case, the center of distribution is shifted towards the right compared to the under-coupling case. This may indicate to us that a larger κ is needed if we want to observe the effect of shifting the distribution to the right in the experiment.

Here, we show that neither under-coupling nor perfect-coupling scenarios adequately explain the experimental findings. In the case of under-coupling, the monotonic decreasing characteristic leads to a distribution of zeros that is predominantly shifted towards negative values. Pushing the scenario to an idealized perfect-coupling, we note a significant slowdown in the decreasing of the distribution, which shifts the distribution in panel (b) center more towards positive values, approaching a balance around zero. This adjustment to an extreme case raises an intriguing question: What would the results be if the system were over-coupled, and could this potentially explain the experimental findings? We will explore this possibility in the following section, as detailed in subsection 4.4.2.

4.4.2 Over Coupling

Before discussing the distribution of zeros for over-coupled scenarios, it is useful to examine their density of states. For under-coupling, the distribution of the real parts of zeros typically aligns with the predictions of the semicircle law. Although weak coupling is not explicitly displayed here, the limiting case of perfect-coupling sufficiently illustrates the expected behavior.

For perfect-coupling, in Fig. 4.14 (a), zeros calculated from the effective Hamiltonian (4.8) are plotted in the complex plane, with colors representing probabilities as indicated by colormap. The parameters used here are $N = 1500$, $M = 4$, $\kappa_P = 1$, and $\Gamma_{\text{hom}} = 37.26$. When analyzing the distribution of the real parts of these zeros, as shown in Fig. 4.14 (b), we find a perfect alignment with the semicircle law's predictions. Note, that for a better comparison with over-coupling case, the real

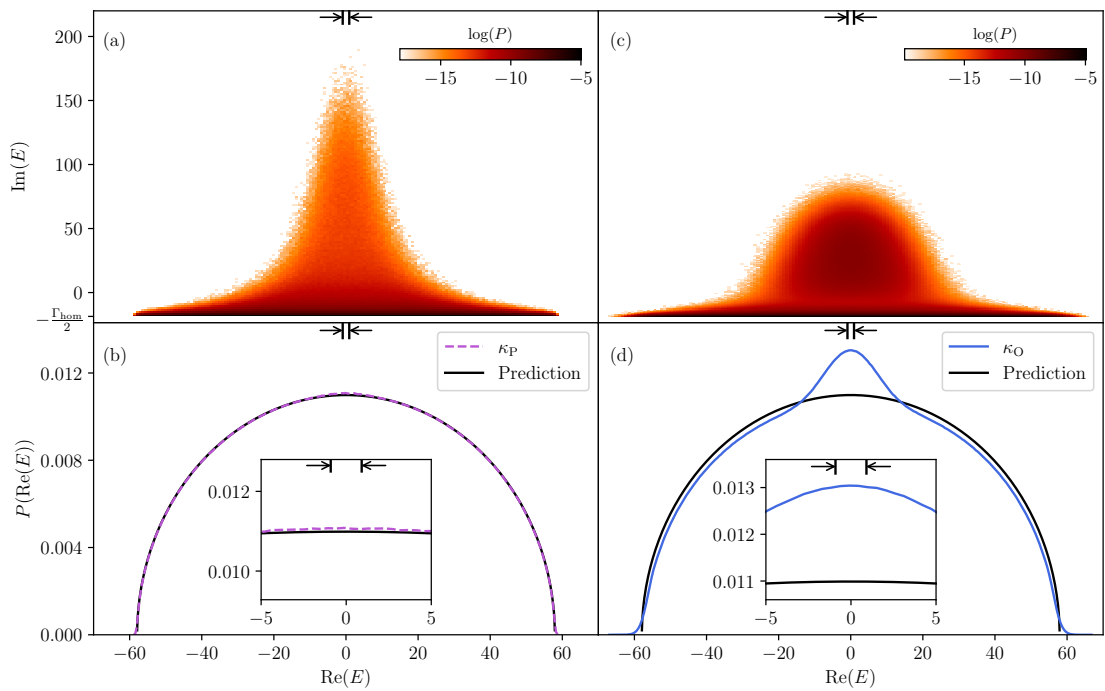


Figure 4.14: (a) and (b) show the distribution of complex zeros and their real parts, respectively, for a non-Hermitian Hamiltonian with $N = 1500$, $M = 4$, $\kappa_P = 1$, and $\Gamma_{\text{hom}} = 37.26$. The real parts of the zeros have been rescaled by $91/N$ for the sake of comparison to (c) and (d). (c) and (d) same as (a) and (b) but with $N = 91$ and $\kappa_O = 2.005$.

part of zeros in panels (a) and (b) has been rescaled by a factor $91/1500$ ($91/N$), while the imaginary part remains unchanged. The black arrows indicate the real energy interval $|\text{Re}(E)| \leq N/100$, which is used to constrain the zeros for probability statistics, as mentioned already in subsection 4.4.1. It is shown that the density of states is practically constant and equal to 1 in this interval.

For over-coupling, the zeros in this case are calculated from an effective Hamiltonian with parameters $N = 91$, $M = 4$, $\kappa_O = 2.005$, and $\Gamma_{\text{hom}} = 37.26$. The specific choice of parameters will become evident later as they will be the ones describing the experimental results the best. Unlike the distribution observed in Fig. 4.14 (a), which decreases significantly as the imaginary part increases, the distribution in Fig. 4.14 (c) creates a distinct bump around the central region. Further examining the distribution of the real parts of zeros, as shown in Fig. 4.14 (d), we can see that a bump forms near $E = 0$. This deviation from the semicircle law highlights a distinct feature of over-coupling. As explained in subsection 2.3.5, large over-coupling value can cause M eigenvalues to acquire large imaginary parts, leading to a clear separation of the eigenvalue cloud. Note that in the region indicated by the black arrow, although the density of states appears to be constant, it is slightly larger than 1, due to the fact that the 4 resonances associated with the 4 channels accumulate close to zero (see also Fig. 2.4 in subsection 2.3.5). In this case the semicircular behavior is created by the $87=91-4$ standard states and the additional Gaussian like bump at $E = 0$ by these 4 zeros related to the 4 superradiant states/resonances.

Note, that the imaginary part for perfect-coupling shows a larger tail than the over-coupling one, but there is already an increased probability for zeros having an imaginary part around 25. Turning our focus back to the main discussion, we explored the distribution of the imaginary part of the zeros in the over-coupling case, to see if it could possibly explain the experimental findings. Starting from the most natural setup, as detailed in the previous subsection 4.4.1, we will choose a fairly large Hamiltonian, with $N = 1500$. The number of channels, $M = 4$, and the global loss, $\Gamma_{\text{hom}} = 37.26$, are kept unchanged. Within this framework, we apply the average transmission formula trying to keep $T_a = 0.97$ as in the experiment and κ as a function of M/N and T_a , which yields two values: one for under-coupling, $\kappa = 0.7196$, which has already been discussed, and the other for over-coupling, $\kappa = 1.449$.

As depicted by the green dash-dotted line in Fig. 4.15 (a), the zeros computed from the Hamiltonian with $N = 1500$ and $\kappa = 1.449$ show a decreasing behavior at very small imaginary parts, but show a clear bump between around 20 and 500. Actually the distribution for small $\text{Im}(E) < 100$ is exactly the same as in the under-coupling case with a slight renormalization due to the bump. The occurrence of the bump is in line with expectations, as we've previously discussed the characteristics of superradiant poles in subsection 2.3.5. To compare with experimental results effectively, we must examine the extracted zeros for the over-coupling case. Fig. 4.15 (b) displays the distribution of the imaginary parts of zeros extracted numerically for $N = 1500$ and $\kappa = 1.449$, following the same process used in experiments. We find that the distribution is centered on the negative imaginary value, despite the presence of over-coupling, which is clearly different from the experimental center and similar to the under-coupling results of the previous subsection. Note, that it shows

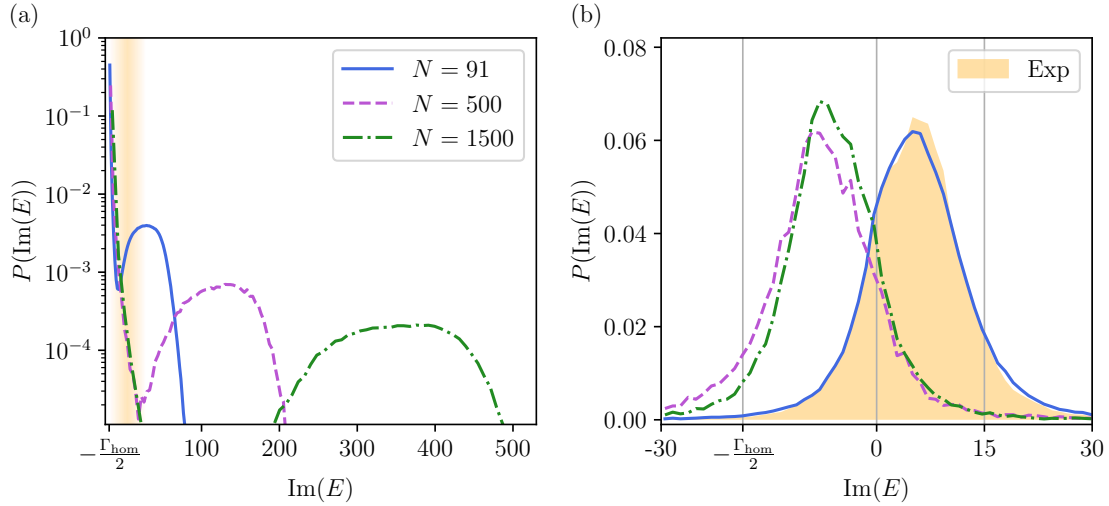


Figure 4.15: (a) Distribution of the imaginary parts of zeros calculated from non-Hermitian Hamiltonian with $N = 91$ and $\kappa_{\text{O}} = 2.005$ (blue solid line), $N = 500$ and $N = 1500$ (purple dashed line), and $N = 1500$ and $\kappa = 1.449$ (green dash-dotted line), while maintaining $M = 4$, $\Gamma_{\text{hom}} = 37.26$, and corresponding over-coupling κ are calculated for each N keeping $T_a = 0.97$. (b) Comparison of the distributions of the imaginary parts of zeros extracted following experimental protocols, experimentally and numerically (as in (a)).

that there are some zeros below $-\Gamma_{\text{hom}}/2$, which is theoretically impossible and is due to fitting errors in the extraction process.

Going back to Fig. 4.15 (a), the orange region indicates the range of the imaginary part of the zeros that experimental extraction can reach. In this range, the distribution of $N = 1500$ and $\kappa = 1.449$ shows a consistent decreasing, much like the under-coupling case. In both the numerical and experimental setups, only real energy/frequency is accessible, so that zeros can only be extracted near $\text{Im}(E) = 0$. Thus, even the presence of a significant bump in the higher imaginary part is difficult to achieve in practice, which explains why the over-coupling distribution in Fig. 4.15 (b) is so similar to the under-coupling distribution, see Fig. 4.13 (b).

This shows that, in the over-coupling case, zeros of extremely large widths occur. However, these large width zeros do not substantially change the final distribution. This observation leads to the question: what happens if we choose smaller N while maintaining the high κ values typical of over-coupling?

In Fig. 4.15 (a) and (b), we show the simulation with $N = 500$ and $\kappa = 1.511$, keeping M and Γ_{hom} unchanged. The κ value is calculated by keeping T_a as in the experiment. The purple dashed line in Fig. 4.15 (a) shows that, despite the reduction of N , the bump in the distribution still occurs at high values, beyond the range of the experimental extraction. Therefore, as shown in Fig. 4.15 (b), the distribution is still similar to the one observed with $N = 1500$ and $\kappa = 1.449$, and does not adequately characterize the experimental results.

As observed, by decreasing N and adjusting κ , the bump in the distribution of zeros computed from the Hamiltonian moves closer to $\text{Im}(E) = 0$. It is conceivable that if this bump moves within the extractable range, the large width of the zeros

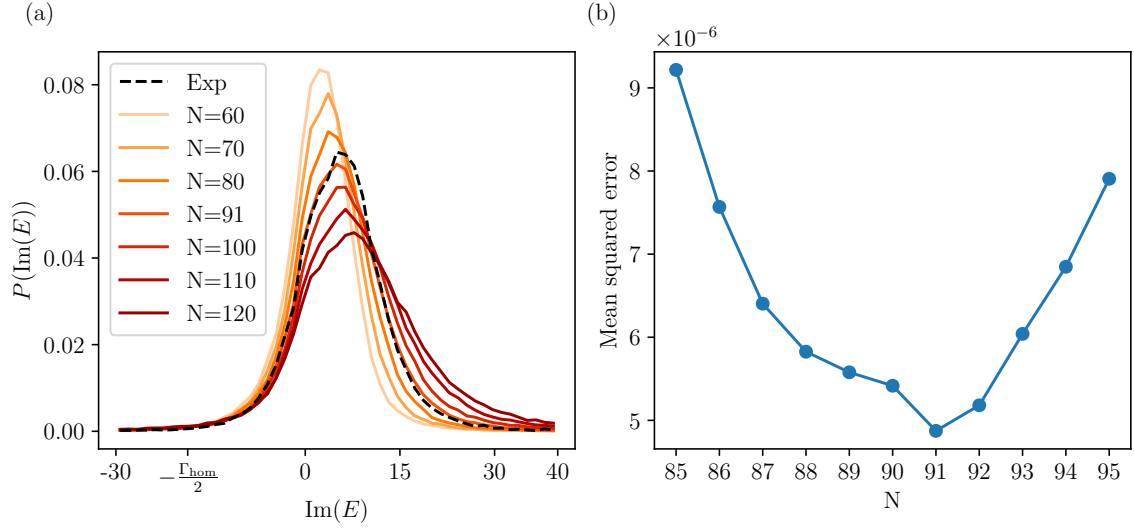


Figure 4.16: (a) Distribution of the imaginary part of the extracted zeros, with the experimental and numerical results shown as black dashed and solid lines, respectively. The colors of the solid lines transition from yellow to red, as the size of Hamiltonian N increases, and over-coupling κ is calculated correspondingly with $M = 4$ and $\Gamma_{\text{hom}} = 37.26$ satisfying experimental $T_a = 0.97$. (b) Mean squared error between the experimental and numerical distributions across different values of N and over-coupling κ .

may significantly affect the final extracted distribution of zeros.

In Fig. 4.15 (a) and (b), the blue solid lines represent the cases $N = 91$ and $\kappa_O = 2.005$. κ_O is calculated from $N = 91$, $M = 4$ and $\Gamma_{\text{hom}} = 37.26$ to keep $T_a = 0.97$ as in the experiment. In panel (a), the distribution of the blue solid line no longer exhibits monotonic decreasing within the orange region; it first decreases, then reaches a local minimum around $\text{Im}(E) = -7$, and then increases. This suggests that not only the decreasing part but also the bump part of the zeros can be reached, which may influence the extracted distribution of zeros with respect to previous observations. Panel (b) shows this distribution of imaginary part of extracted zeros, and finally it is shifted towards positive values, having a good agreement with the experimental one.

Parameters $N = 91$ and $\kappa_O = 2.005$ are carefully chosen. In Fig. 4.16 (a), we show numerical simulations from $N = 60$ to $N = 120$, where each N corresponds to a specific over-coupling parameter κ , with $M = 4$ and $\Gamma_{\text{hom}} = 37.26$ satisfying $T_a = 0.97$. Comparing these results, one can observe that as N increases, the center of the distribution shifts towards larger values and the peak of the distribution decreases. This trend suggests that the best match with experimental results may occur between $N = 80$ and $N = 100$. Fig. 4.16 (b) provides a detailed calculation of the mean square error between the numerical and experimental distributions, from $N = 85$ to $N = 95$. By increasing N by 1 each time and plotting the error corresponding to each N , we find that there is a minimum value, which indicates that the best match between numerical simulation and experimental findings at $N = 91$ and $\kappa_O = 2.005$. Note, that in this chapter, long before this result was given, some of the numerical simulations were done using these specific parameters to present the finally relevant case already there.

Here by comparing the distributions of imaginary parts of numerical and experimental extracted zeros, we find the numerical parameters that best describe the experimental findings are $N = 91$, $\kappa_O = 2.005$, $M = 4$ and $\Gamma_{\text{hom}} = 37.26$. In next section 4.5, we will parametrically study the statistical behavior of the zeros, and verify again that the description from RMT and effective Hamiltonian built from the optimal parameters here, are consistent with the experimental findings.

4.5 Stirring generated Zeros Dynamics

4.5.1 Experimental Findings

Perturbation is a key tool in studying the dynamic behavior of zeros. It is possible to generate a perturbation by flipping pixels of RIS, this imposing a shift of the resonances, but then flipping another pixel leading to non-continuous behaviors of the perturbation. To achieve a more consistent and continuous perturbation, we use a mechanical stirrer in CRC. By combining RIS and the stirrer, we can find zeros near the real axis, and continuously perturb the system, greatly facilitating the observation of the dynamics of zeros.

Typically, a mechanical stirrer in RC is used to create perturbations and thus allows for statistical investigations. Fig. 4.2 shows the mechanical stirrer in the CRC system, which consists of five irregular paddles. The stirrer is controlled by a stepper motor that receives commands from the computer, and the rotation of the stirrer is synchronized with the measurements of the VNA.

In order to capture the full dynamics of the zeros in our experiments, we try to move the zeros initially close to the real axis. This is because we want to capture the movement of the zeros throughout the dynamics and the pronounced peaks in the spectrum $(S^{-1})_{12}$ facilitate the extraction. Specifically, we measured the scattering matrix while RISs are in random configuration. If the eigenvalues of scattering matrix is small (corresponds to a zero near real axis), we zoom in to this small frequency range and rotate the stirrer at a small angle $\Delta\alpha$ for 20 times, measuring the scattering matrix after each angular adjustment. Note, that the rotation angle of the stirrer needs to be adjusted so that even after rotation one can extract zeros, and RISs remained unchanged until the stirrer has completed 20 steps ($20\Delta\alpha$) and moves on to the next set of experiments.

Using the method of zero extraction described in subsection 4.2.5, we can obtain the dynamics of the zeros. Fig. 4.17 (a) presents an example of 4 consecutive measurements from a set of 20 perturbations, with the order indicated by the color from light red to dark red. In the top panel, we observe that the peak and center position of the $|(S^{-1})_{12}|$ change as the stirrer rotates. Further inspection in the middle panel, the phase of $(S^{-1})_{12}$ reveals a phase shift near the peak, with first two measurements showing a negative slope and last two showing a positive slope. Recalling the example in Fig. 4.9, we may conclude that the imaginary part of the zero is likely to change sign between the initial and final measurements. The bottom panel confirms that the zeros extracted by the complex Lorentzian fit moves from above to below the real axis, under the influence of stirrer-induced dynamics.

In Fig. 4.17 (b), we show the zero dynamics in an energy range, with both

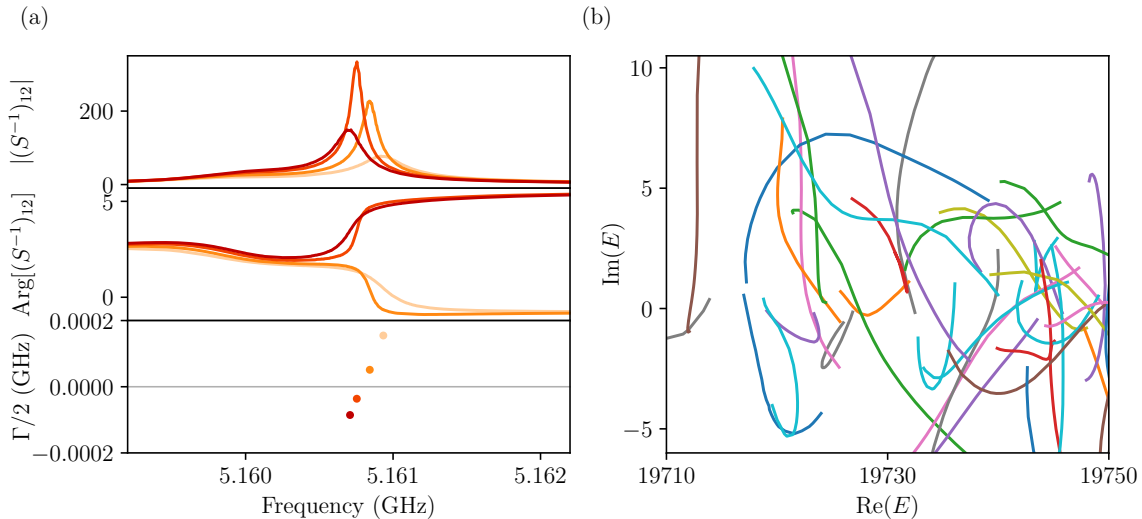


Figure 4.17: In the top and middle part of panel (a), the modulus and phase of $(S^{-1})_{12}$ are shown. The bottom part plots the zeros in the complex plane, extracted from $(S^{-1})_{12}$ by Lorentz fitting. The color of lines and dots indicated the order of dynamics, from light red to dark red. Panel (b) shows the trajectories of zeros in the complex plane for several experiments, each represented by a different color.

the real and imaginary parts normalized by the mean frequency spacing. Different colors in the figure represent independent experiments, with each line consisting of 20 points. These zero curves show their diverse behavior in response to the stirrer's perturbations. One possible way to analyze their statistical behavior is to study the velocity of these dynamics. As mentioned in subsection 2.2.3, the velocity of eigenvalues in a chaotic system could be predicted by RMT. Here, we will compute the velocities of the real part of the zeros $\text{Re}(z_i)$. Note, that for simplicity, $\text{Re}(z_i)$ will be replaced by z_i in the following discussion.

The velocity $v_{\alpha,i}$ of z_i with respect to the angle parameter α can be expressed as a finite difference approximation of the derivative:

$$v_{\alpha,i} = \frac{z_i(\alpha + \Delta\alpha) - z_i(\alpha)}{\Delta\alpha}, \quad (4.18)$$

where $\Delta\alpha$ is the single rotation angle of the stirrer. The system-specific properties related to the parametric variation should be eliminated by unfolding the parameter along $z_i(\alpha)$:

$$\tilde{v}_i = \frac{v_{\alpha,i}}{\sigma_\alpha}, \quad (4.19)$$

here the standard deviation σ_α is calculated from the data of all velocities. In our experiments, $\sigma_\alpha = 381$. So far, we have experimentally extracted the dynamics of the zeros and computed the normalized velocities, and we will compare the distribution of experimental with numerical results in subsection 4.5.2.

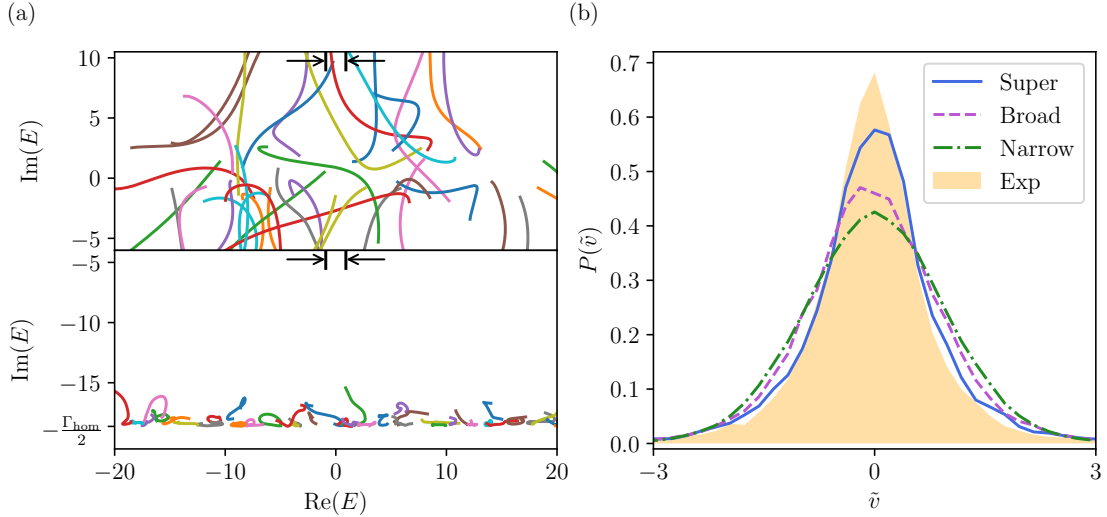


Figure 4.18: (a) Dynamics of the numerical zeros, calculated by effective Hamiltonian (4.8) and (4.20), whose parameters are from over-coupling case. (Top panel) Dynamics of the zeros close to real axis, gathered from varying realizations. (Bottom panel) Dynamics of the zeros close to $-\Gamma_{\text{hom}}/2$, calculated from a single realization for clarity and consistency in the visualization of dynamics. (c) Experimental and numerical distribution of the normalized velocity \tilde{v} , for the real parts of the dynamical zeros. The experimental data is depicted with light yellow filling. The labels for the lines are clarified in the main text.

4.5.2 Numerical Findings

Like the continuous perturbation by the mechanical stirrer in experiment, numerically we can also parametrically study dynamics of zeros by introducing the Hamiltonian consists of an unstirred component H_{us} and a stirred component H_{s} [Die06]

$$H_{\text{P}} = \cos(\beta)H_{\text{us}} + \sin(\beta)H_{\text{s}}, \quad (4.20)$$

where β is the perturbation strength generating the dynamics, and both H_{us} and H_{s} are drawn from GOE. If we replace the Hamiltonian H_0 of Eq. (4.8) by H_{P} , we can calculate the zeros related to parameter β .

Fig. 4.18 (a) shows the simulation results, the upper and lower parts are the zeros whose imaginary part is close to 0 and $-\Gamma_{\text{hom}}/2$. Here, we use the parameters from subsection 4.4.2 that best match the experiment, namely $N = 91$, $M = 4$, $\kappa_{\text{O}} = 2.005$, and $\Gamma_{\text{hom}} = 37.26$. The window of complex plane is chosen exactly same as Fig. 4.17 (b). We adjust the parameter β length of the dynamics in the upper figure to visually as similar as the one in experiment, and the lower figure has the same parameter length with the upper one. Visually comparing the dynamics of the upper and lower panels, we can see that for the upper one, the zeros move over a larger area in the complex plane, while most of the zeros of $\text{Im}(E)$ close to $-\Gamma_{\text{hom}}/2$ are concentrated in a very small area. Note, that in the figure, for clarity, we only draw part of the dynamics, and for the zeros in the bottom panel, some may show a wider movement, indicating a superradiant transition.

For comparison with the experimental results, we calculated the normalized ve-

locity of the zeros in our numerical simulations. Note, that the statistics include only zeros in the real energy interval shown by the black arrow, where $|\text{Re}(E)| \leq N/100$ to keep the density of states practically constant and very close to 1 in the investigated energy range. Fig. 4.18 (b) shows the distribution of \tilde{v} , and we begin by discussing zeros close to $-\Gamma_{\text{hom}}/2$, referring to the lower panel of Fig. 4.18 (a) and labeled “Narrow”. These zeros are selected from the range $-\Gamma_{\text{hom}}/2 < \text{Im}(z) < -\Gamma_{\text{hom}}/2 + 1$, and the distribution of their velocities, shown by the green dash-dotted line in the figure, exhibits Gaussian behavior. This aligns with the RMT predictions for the velocity distribution of eigenvalues for under-coupling chaotic system [Bar99, Lu20]. It is clear, that this part of the zeros, its velocity distribution is not consistent with the experiment. In this case, $\sigma_\beta = 0.53$.

Next, we focus on zeros near the real axis, as shown in the upper panel of Fig. 4.18 (a). In particular, we analyze the zeros where the imaginary part satisfies $-10 < \text{Im}(z) < 15$ and the real part is restricted to the range shown by the black arrows. The dynamics depicted by the solid blue line labeled “Super” in Fig. 4.18 (b), and it matches the experimental findings very well, especially the tail. There is a deviation in the middle peak of the two, which may be due to experimental error. In this case, $\sigma_\beta = 1.9$. The agreement here, in another respect, again validates our numerical model for describing the experimental system using overcoupling.

To provide a more convincing demonstration, we also performed another simulation with under-coupling conditions using the parameters $N = 1500$, $M = 4$, $\kappa_U = 0.7196$, and $\Gamma_{\text{hom}} = 37.26$. As shown in Fig. 4.13 (a), this setup predicts the presence of zeros near the real axis. Thus in this case, we are able to observe the dynamics of these zeros. By restricting the selection of zeros where their imaginary part satisfies $-10 < \text{Im}(z) < 15$ and real part by the black arrows, their normalized velocities can be calculated. We label this group as “Broad” with a value of $\sigma_\beta = 1.8$. In Fig. 4.18 (b), shown by the purple dashed line, the distribution derived from under-coupling does not match the experimental results; it lies between the “Super” and “Narrow” distributions.

In this section, the level dynamics of zero was investigated experimentally and numerically. By comparing the experimental and numerical results, we find a good agreement, affirming that over-coupling is an accurate way to describe CRC system, which is a strong support for the discussion in this subsection 4.4.2. The discussion confirms that the observed behavior of the zeros is different from the zeros with narrow width under perturbation. In section 4.6, we will focus on the zero that located on the real axis, CPA, and explore the sensitivity of this particular zero to temperature perturbations in experimental studies.

4.6 CPA in CRC as Temperature Sensor

Earlier works have demonstrated the ability of the CPA to act as a sensor [Li19, Zha22b]. In CRC, the sensitivity of the CPA could be used to verify the stability of the chamber. This can infer whether a mechanical stirrer returns to its initial position, whether opening and closing a door or other types of changes change the RC. In this thesis, to demonstrate the sensitivity of CPA in our CRC system, specifically, we will investigate the relation between temperature and the CPA.

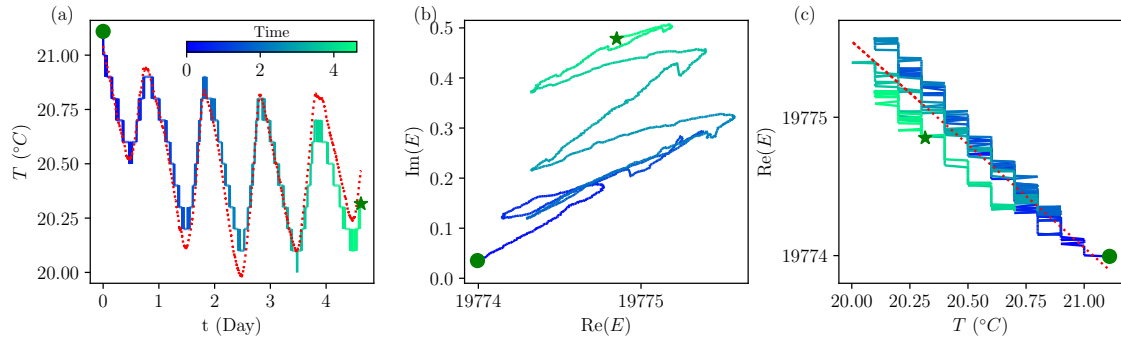


Figure 4.19: (a) Temperature of reverberation chamber versus time. Color variations along the curves indicate elapsed time, with circles and stars marking the start and end points, respectively. The red dotted curves represents a temperature curve reconstructed from the relationship between temperature and the real part of zeros derived from (c). (b) Time-dependent zeros plotted in the complex plane, illustrating the dynamical evolution of a superradiant CPA. (c) The relation between temperature T and the real part of zeros.

In the first case, we study CPA in a lab where the temperature T is oscillating due to day-night temperature variation. The discussion of experimental temperature and humidity measurement, and the details of sensors can be found in subsection 4.2.1. Fig. 4.19 (a) records the fluctuations of the temperature of the lab over several days, where the color represents the time, and the circles and stars represent the starting and ending points. At the starting point, we realized CPA, by optimizing the eigenvalues of scattering matrix as close as possible to 0 through the RISs, see the method mentioned in subsection 4.2.4. Then we re-measure the spectra at around every 4 minutes, and we extract and trace the zeros in the complex plane, where both real and imaginary parts are normalized. In Fig. 4.19 (b), we obtain the variation of the zeros in the complex plane with time, which shows that the zeros are moving further and further away from the real axis over time and on oscillating behavior of the real part. This indicates that the CPA is not stable and will not lie on the real axis once it is subjected to an external perturbation (e.g., temperature).

Then, we plot the temperature versus the real part of the zero, see Fig. 4.19 (c), what we find is that zero's real value gets smaller every time the temperature of the room gets lower over the days, and these lines oscillate with a linear relationship. In panel (c), we fit a linear function for the real part of zeros and temperatures with red dotted line. Satisfying such a relationship, in fact, our CRC is acting like a sensor, because now we can use the zeros to predict the temperature. The red dotted line in Fig. 4.19 (a) is the reconstruction result, which is obtained by using the information of experimental zeros and the fitting parameter. It is shown that the reconstructed temperature is very close to the original temperature, and now just by measuring the spectrum from the experiment and extract the zeros, we are able to determine the temperature. Also, it is worth noting that the resolution of the temperature sensor in this measurement is 0.1°C , as can be seen from the measurements' discretization in Fig. 4.19 (a) and (c). However, based on the CPA, one could obtain temperature curves with much better resolution.

Fig. 4.20 (a), (b) and (c) show the other example, where we installed the rever-

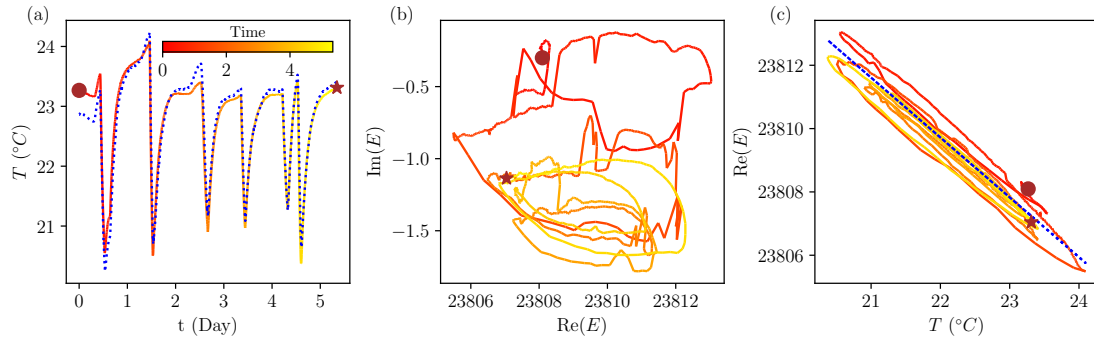


Figure 4.20: (a), (b) and (c) replicate the analyses of Fig. 4.19 respectively, but are conducted in a different laboratory environment (equipped with air conditioning).

beration chamber in an air-conditioned laboratory. By controlling the temperature of the air conditioner to the maximum or minimum, the room has a greater range of temperature changes. Similarly, following the experimental steps, we can obtain the dynamics of the zeros in the complex plane as the temperature changes, as well as obtaining the relationship between the real part of the zeros and the temperature. The relationship between the two in Fig. 4.20 (c) can be fitted with a linear function (blue dotted line), which is consistent with the previously observed dependence. Here we used a temperature sensor with a resolution of 0.01°C , thus no discretization appears in the figure. In this case, the reconstructed curve (blue dotted line) also agrees very well with the temperature line previously measured by the temperature sensor, see Fig. 4.20 (a). Note, that we only found a relationship between temperature and the real part of zeros, we did not find any relationship between temperature and the imaginary part of zeros, nor did we find any relationship between humidity and the real or imaginary part of zeros.

The investigation into the stability behavior of CPA within a chaotic system, has uncovered a linear relationship between the real part of zeros and temperatures. This finding extends our understanding of CPA behavior in complex environments and unveils a temperature-dependent aspect of CPA points.

4.7 Conclusion

In section 4.1, we introduce CRC and the phenomenon of CPA. We refine the description of lossy systems within the framework of the effective Hamiltonian approach, setting the stage to explain why CPAs and zeros occur near the real axis in the strong overlap regime.

The section 4.2 detail our experimental setup, three important experimental parameters, number of the channels $M = 4$, transmission coefficient $T_a = 0.97$ and global loss $\Gamma_{\text{hom}} = 37.26$. It also details how CPAs are realized experimentally and how zeros are extracted, presenting the distribution of the imaginary parts of zeros obtained from experiments.

In the section 4.3, aimed at deriving numerical parameters for the effective Hamiltonian, we adjust the average scattering characteristics of a chaotic system with global loss. By incorporating complex energy into the formulation, we validate that

both exact and approximate solutions align with numerical simulations, confirming that our revised formulas meet our experimental needs.

The section 4.4 employs the refined approximate solution to initially attempt describing experimental findings with an under-coupling numerical model, which proves unsuccessful. We then discover that to account for the distribution of the imaginary parts of zeros observed experimentally, over-coupling parameters are necessary. The optimal parameters found are $N = 91$ and $\kappa_O = 2.005$, where κ_O is calculated by substituting $N = 91$, $M = 4$, and $\Gamma_{\text{hom}} = 37.26$ into the formulas to guarantee a transmission coefficient $T_a = 0.97$ with the RMT simulations matching the experimental one.

In section 4.5, we apply continuous perturbations using a stirrer, and study the distribution of the normalized velocities of the real parts of zeros. We further confirm that the experimentally results can be fully described by the effective Hamiltonian constructed from over-coupling parameters, whereas again a description via the under-coupling case shows prominent deviations.

In section 4.6, by investigating the temperature perturbation to CPA in two environments, we find a linear dependence between external temperature and the real part of CPA, suggesting that CPA could serve as a temperature sensor for the reverberation chamber.

Chapter 5

Conclusions and Outlook

In this thesis, I have conducted microwave experiments on two systems: microwave networks and chaotic reverberation chambers (CRC). In both systems, I have compared the experimental findings to numerical simulations fixing their parameters partially on newly developed theoretical descriptions. In both cases superradiance, i.e., the existence of fast decaying states due to strong coupling to the environment, plays a crucial role. In case of the microwave network it leads toward the reduction of resonances when the boundary conditions at the coupling vertex are varied from near to exact Neumann conditions. In case of the CRC it guarantees the existence of sufficient number of zeros in the vicinity of the real axis, predicted by the effective Hamiltonian with over-coupling.

For the first time we succeeded to vary experimentally the coupling strength to microwave networks over a large frequency range. This was realized by using a T-junction with a phase-variable bond, where the boundary condition at the coupling vertex was varied from Dirichlet to Neumann, based on the idea from the analogue experiment [Reh16] of Gaussian symplectic ensemble (GSE) graphs. This technique is particularly well-suited for studying non-Weyl graphs, open graphs with balanced vertices where the relationship between the wavenumber and the number of resonances does not satisfy Weyl's law. In tetrahedral graphs with balanced vertex of valency 2, we observed complex dynamics of resonances in the complex plane as a function of coupling. These dynamics included loop structures, regions of connected resonances, and some resonances escaping to infinite width via a superradiant transition, thus unambiguously demonstrating non-Weyl behavior. The latter features is not related to the complexity of the graph but already appears in lasso graphs. For this simple system an analytical solution was derived and had a good agreement with experiments and perfect agreement with numerical simulations were found. For rational ratios of the two length the spectrum shows a corresponding periodic structures of the poles and the dependence of the pole structure on the ratios will be investigated in the future. I would like to point out that close to balanced conditions, superradiant states and bound states in the continuum coexist, thus providing a basis for studying their interaction when small perturbations are introduced. In the future, the technique of variable coupling gives the possibility to study numerous interesting problems in graphs, such as the interlacing theorem [Ber13, Ber17] in open systems, coherent perfect absorption (CPA) [Cho10, Che20, Wan24a] and

exceptional points (EP) [Dem01, Dop16].

Also, I presented the studies of CPAs in a CRC system and found that the proper description of CPAs in this system with large modal overlap relies on the use of over-coupling, i.e., the existence of superradiance in the system. This conclusion is obtained from comparing the experimental and numerical statistical distributions in the strong modal overlap case. One key distribution is that of the imaginary part of the zeros. Experimentally, we extracted zeros through uncorrelated realizations generated by reconfigurable intelligent surfaces (RIS). Numerically, we computed the zeros from the effective Hamiltonian where we have used experimentally determined parameters related to losses and over-coupling. The other distribution is that of the velocity of the real part of zeros. Experimentally, we collected these zeros using a continuous perturbation via mechanical stirring, and numerically simulated a parametrically varied internal Hamiltonian together with over-coupling. In both cases, a good agreement was found only when over-coupling was present and distinct deviations were found if it was not present. Thus, I could demonstrate that the zeros measured in our experiments correspond to associated superradiant poles. In addition, we changed the temperature of CPA systems, and found that these CPAs are extremely sensitive to this perturbation, thus rendering them excellent candidates to act as sensors, which I demonstrated experimentally. This work should trigger new developments in the framework of RMT to address the till now more or less neglected regime of over-coupling. Hopefully analytical descriptions of the here investigated distributions as well as the density of states will be derived in the near future. Additionally, the determination of the parameters like coupling strength, size of Hamiltonian or number of channels will be hopefully better justified by new theoretical means. This discovery should also pave the way to new sensors based on CPAs in the strong modal overlap regime.

Bibliography

- [All14] M. Allgaier, S. Gehler, S. Barkhofen, H.-J. Stöckmann, and U. Kuhl: Spectral properties of microwave graphs with local absorption. *Phys. Rev. E* **89**, 022925 (2014).
- [Alt97] A. Altland and M. R. Zirnbauer: Nonstandard symmetry classes in mesoscopic normal-superconducting hybrid structures. *Phys. Rev. B* **55**, 1142 (1997).
- [Ara16] M. O. Araújo, I. Krešić, R. Kaiser, and W. Guerin: Superradiance in a large and dilute cloud of cold atoms in the linear-optics regime. *Phys. Rev. Lett.* **117**, 073002 (2016).
- [Aue11] N. Auerbach and V. Zelevinsky: Super-radiant dynamics, doorways and resonances in nuclei and other open mesoscopic systems. *Rep. Prog. Phys.* **10**, 74 (2011).
- [Bal71] R. Balian and C. Bloch: Asymptotic evaluation of the Green's function for large quantum numbers. *Ann. Phys. (N.Y.)* **63**, 592 (1971).
- [Bal77] R. Balian and B. Duplantier: Electromagnetic waves near perfect conductors. I. Multiple scattering expansion. Distribution of modes. *Ann. Phys. (N.Y.)* **104**, 300 (1977).
- [Bal16] C. A. Balanis: *Antenna theory: analysis and design*. John Wiley & sons 2016.
- [Bar99] M. Barth, U. Kuhl, and H.-J. Stöckmann: Global versus local billiard level dynamics: The limits of universality. *Phys. Rev. Lett.* **82**, 2026 (1999).
- [Bar17] D. G. Baranov, A. Krasnok, T. Shegai, A. Alù, and Y. Chong: Coherent perfect absorbers: linear control of light with light. *Nature Reviews Materials* **2**, 17064 (2017).
- [Bas17] L. Bastianelli, G. Gradoni, F. Moglie, and V. M. Primiani. Full wave analysis of chaotic reverberation chambers. In *2017 XXXIIInd General Assembly and Scientific Symposium of the International Union of Radio Science (URSI GASS)* pages 1–4. IEEE 2017.
- [Ber13] G. Berkolaiko and P. Kuchment: *Introduction to Quantum Graphs*. volume 186 of *Mathematical Surveys and Monographs*. American Mathematical Society Providence, Rhode Island 2013.
- [Ber17] G. Berkolaiko. *An elementary introduction to quantum graphs* volume 700 of *Contemporary Mathematics* chapter 2. American Mathematical Society Providence, Rhode Island 2017.

-
- [Bes11] P. Besnier and B. Démoulin: *Electromagnetic Reverberation Chambers*. ISTE/Wiley 2011.
- [Bia16] M. Białous, V. Yunko, S. Bauch, M. Lawniczak, B. Dietz, and L. Sirko: Power spectrum analysis and missing level statistics of microwave graphs with violated time reversal invariance. *Phys. Rev. Lett.* **117**, 144101 (2016).
- [Bla52] J. M. Blatt and V. F. Weisskopf: *Theoretical Nuclear Physics*. Wiley New York 1952.
- [Blü92] R. Blümel, I. H. Davidson, W. P. Reinhardt, H. Lin, and M. Sharnoff: Quasilinear ridge structures in water surface waves. *Phys. Rev. A* **45**, 2641 (1992).
- [Boh84] O. Bohigas, M. J. Giannoni, and C. Schmit: Characterization of chaotic spectra and universality of level fluctuation laws. *Phys. Rev. Lett.* **52**, 1 (1984).
- [Bun79] L. A. Bunimovich: On the ergodic properties of nowhere dispersing billiards. *Commun. Math. Phys.* **65**, 295 (1979).
- [Cas80] G. Casati, F. Valz-Gris, and I. Guarnieri: On the connection between quantization of nonintegrable systems and statistical theory of spectra. *Lett. Nuov. Cim.* **28**, 279 (1980).
- [Che20] L. Chen, T. Kottos, and S. M. Anlage: Perfect absorption in complex scattering systems with or without hidden symmetries. *Nat. Commun.* **11**, 5826 (2020).
- [Che21a] J. Che, J. Lu, X. Zhang, B. Dietz, and G. Chai: Missing-level statistics in classically chaotic quantum systems with symplectic symmetry. *Phys. Rev. E* **103**, 042212 (2021).
- [Che21b] L. Chen, S. M. Anlage, and Y. V. Fyodorov: Generalization of Wigner time delay to subunitary scattering systems. *Phys. Rev. E* **103**, L050203 (2021).
- [Che21c] L. Chen, S. M. Anlage, and Y. V. Fyodorov: Statistics of complex Wigner time delays as a counter of S -matrix poles: Theory and experiment. *Phys. Rev. Lett.* **127**, 204101 (2021).
- [Che22a] J. Che, X. Zhang, W. Zhang, B. Dietz, and G. Chai: Fluctuation properties of the eigenfrequencies and scattering matrix of closed and open unidirectional graphs with chaotic wave dynamics. *Phys. Rev. E* **106**, 014211 (2022).
- [Che22b] L. Chen and S. M. Anlage: Use of transmission and reflection complex time delays to reveal scattering matrix poles and zeros: Example of the ring graph. *Phys. Rev. E* **105**, 054210 (2022).
- [Chi96] P. A. Chinnery and V. F. Humphrey: Experimental visualization of acoustic resonances within a stadium-shaped cavity. *Phys. Rev. E* **53**, 272 (1996).
- [Cho10] Y. D. Chong, L. Ge, H. Cao, and A. D. Stone: Coherent perfect absorbers: Time-reversed lasers. *Phys. Rev. Lett.* **105**, 053901 (2010).

-
- [Dav27] C. Davisson and L. H. Germer: The scattering of electrons by a single crystal of nickel. *Nature* **119**, 558–560 (1927).
- [Dav10] E. B. Davies, P. Exner, and J. Lipovský: Non-Weyl asymptotics for quantum graphs with general coupling conditions. *J. Phys. A* **43**, 474013 (2010).
- [Dav11] E. B. Davies and A. Pushnitski: Non-Weyl resonance asymptotics for quantum graphs. *Anal. PDE* **4**, 729 (2011).
- [Dav21] M. Davy, P. Besnier, P. del Hougne, J. de Rosny, E. Richalot, F. Sarrazin, D. V. Savin, F. Mortessagne, U. Kuhl, and O. Legrand: Diffuse field cross-correlations: Scattering theory and electromagnetic experiments. *Phys. Rev. E* **104**, 044204 (2021).
- [Del22] T. Delage, O. Pascal, J. Sokoloff, and V. Mazières: Experimental demonstration of virtual critical coupling to a single-mode microwave cavity. *Journal of Applied Physics* **132**, 153105 (2022).
- [Dem01] C. Dembowski, H.-D. Gräf, H. L. Harney, A. Heine, W. D. Heiss, H. Rehfeld, and A. Richter: Experimental observation of the topological structure of exceptional points. *Phys. Rev. Lett.* **86**, 787 (2001).
- [dH20] P. del Hougne, D. V. Savin, O. Legrand, and U. Kuhl: Implementing nonuniversal features with a random matrix theory approach: Application to space-to-configuration multiplexing. *Phys. Rev. E* **102**, 010201 (2020).
- [dH21] P. del Hougne, K. B. Yeo, P. Besnier, and M. Davy: On-demand coherent perfect absorption in complex scattering systems: Time delay divergence and enhanced sensitivity to perturbations. *Laser & Photonics Reviews* **15**, 2000471 (2021).
- [Dic54] R. H. Dicke: Coherence in spontaneous radiation processes. *Phys. Rev.* **93**, 99–110 (1954).
- [Die06] B. Dietz, A. Heine, A. Richter, O. Bohigas, and P. Leboeuf: Spectral statistics in an open parametric billiard system. *Phys. Rev. E* **73**, 035201(R) (2006).
- [Die15] B. Dietz and A. Richter: Quantum and wave dynamical chaos in superconducting microwave billiards. *Chaos: An Interdisciplinary Journal of Nonlinear Science* **25**, 097601 (2015).
- [Die17] B. Dietz, V. Yunko, M. Białous, S. Bauch, M. Ławniczak, and L. Sirko: Nonuniversality in the spectral properties of time-reversal-invariant microwave networks and quantum graphs. *Phys. Rev. E* **95**, 052202 (2017).
- [Die24] B. Dietz, T. Klaus, M. Masi, M. Miski-Oglu, A. Richter, T. Skipa, and M. Wunderle: Closed and open superconducting microwave waveguide networks as a model for quantum graphs. *Phys. Rev. E* **109**, 034201 (2024).
- [Din02] J. Dingjan, E. Altewischer, M. P. van Exter, and J. P. Woerdman: Experimental observation of wave chaos in a conventional optical resonator. *Phys. Rev. Lett.* **88**, 064101 (2002).

-
- [Dit00] F.-M. Dittes: The decay of quantum systems with a small number of open channels. *Phys. Rep.* **339**, 215 (2000).
- [Dop16] J. Doppler, A. A. Mailybaev, J. Böhm, U. Kuhl, A. Girschik, F. Libisch, T. J. Milburn, P. Rabl, N. Moiseyev, and S. Rotter: Dynamically encircling an exceptional point for asymmetric mode switching. *Nature* **537**, 76 (2016).
- [Doy01] V. Doya, O. Legrand, F. Mortessagne, and C. Miniatura: Light scarring in an optical fiber. *Phys. Rev. Lett.* **88**, 014102 (2001).
- [Dys62] F. J. Dyson: The threefold way. Algebraic structure of symmetry groups and ensembles in quantum mechanics. *J. Math. Phys.* **3**, 1199 (1962).
- [Exn11] P. Exner and J. Lipovský: Non-Weyl resonance asymptotics for quantum graphs in a magnetic field. *Phys. Lett. A* **375**, 805 (2011).
- [Far24] O. Farooq, A. Akhshani, M. Ławniczak, M. Białous, and L. Sirko: Coupled unidirectional chaotic microwave graphs. *Phys. Rev. E* **110**, 014206 (2024).
- [Fra20] B. W. Frazier, T. M. Antonsen, S. M. Anlage, and E. Ott: Wavefront shaping with a tunable metasurface: Creating cold spots and coherent perfect absorption at arbitrary frequencies. *Phys. Rev. Res.* **2**, 043422 (2020).
- [Fyo96] Y. V. Fyodorov and H.-J. Sommers: Statistics of s -matrix poles in few-channel chaotic scattering: crossover from isolated to overlapping resonances. *JETP Lett.* **63**, 1026 (1996).
- [Fyo97] Y. V. Fyodorov and H.-J. Sommers: Statistics of resonance poles, phase shifts and time delays in quantum chaotic scattering: Random matrix approach for systems with broken time-reversal invariance. *J. Math. Phys.* **38**, 1918 (1997).
- [Fyo17] Y. V. Fyodorov, S. Suwunnarat, and T. Kottos: Distribution of zeros of the s -matrix of chaotic cavities with localized losses and coherent perfect absorption: non-perturbative results. *J. Phys. A* **50**, 30LT01 (2017).
- [Fyo19] Y. Fyodorov: Reflection time difference as a probe of s -matrix zeroes in chaotic resonance scattering. *Acta Physica Polonica A* **136**, 785 (2019).
- [Gnu04] S. Gnutzmann and A. Altland: Universal spectral statistics in quantum graphs. *Phys. Rev. Lett.* **93**, 194101 (2004).
- [Gnu06] S. Gnutzmann and U. Smilansky: Quantum graphs: Applications to quantum chaos and universal spectral statistics. *Advances in Physics* **55**, 527 (2006).
- [Gnu13] S. Gnutzmann, H. Schanz, and U. Smilansky: Topological resonances in scattering on networks (graphs). *Phys. Rev. Lett.* **110**, 094101 (2013).
- [Grä92] H.-D. Gräf, H. L. Harney, H. Lengeler, C. H. Lewenkopf, C. Rangacharyulu, A. Richter, P. Schardt, and H. A. Weidenmüller: Distribution of eigenmodes in a superconducting stadium billiard with chaotic dynamics. *Phys. Rev. Lett.* **69**, 1296 (1992).

-
- [Gri13] V. Grigoriev, A. Tahri, S. Varault, B. Rolly, B. Stout, J. Wenger, and N. Bonod: Optimization of resonant effects in nanostructures via weierstrass factorization. *Phys. Rev. A* **88**, 011803 (2013).
- [Gro14a] J.-B. Gros. *Statistiques spatiales des cavités chaotiques ouvertes : applications aux cavités électromagnétiques*. Dissertation at Université de Nice-Sophia Antipolis, 2014.
- [Gro14b] J.-B. Gros, U. Kuhl, O. Legrand, F. Mortessagne, E. Richalot, and D. V. Savin: Experimental width shift distribution: A test of nonorthogonality for local and global perturbations. *Phys. Rev. Lett.* **113**, 224101 (2014).
- [Gro14c] J.-B. Gros, O. Legrand, F. Mortessagne, E. Richalot, and K. Selemani: Universal behaviour of a wave chaos based electromagnetic reverberation chamber. *Wave Motion* **51**, 664 (2014).
- [Gro15] J.-B. Gros, U. Kuhl, O. Legrand, F. Mortessagne, and E. Richalot. Universal intensity statistics in a chaotic reverberation chamber to refine the criterion of statistical field uniformity. In *Metrology for Aerospace (MetroAeroSpace), 2015 IEEE Metrology for Aerospace (MetroAeroSpace), 2015 IEEE* page 225 Benevento, Italy Jun 2015. IEEE.
- [Gro16] J.-B. Gros, U. Kuhl, O. Legrand, and F. Mortessagne: Lossy chaotic electromagnetic reverberation chambers: Universal statistical behavior of the vectorial field. *Phys. Rev. E* **93**, 032108 (2016).
- [Gro20] J.-B. Gros, P. del Hougne, and G. Lerosey: Tuning a regular cavity to wave chaos with metasurface-reconfigurable walls. *Phys. Rev. A* **101**, 061801(R) (2020).
- [Gro21] J.-B. Gros, G. Lerosey, F. Mortessagne, U. Kuhl, and O. Legrand: Uncorrelated configurations and field uniformity in reverberation chambers stirred by reconfigurable metasurfaces. *Appl. Phys. Lett.* **118**, 144101 (2021).
- [Guh09] T. Guhr: Doorway mechanism in many body systems and in quantum billiards. *Acta Physica Polonica A* **116**, 741 (2009).
- [Haa92] F. Haake, F. Izrailev, N. Lehmann, D. Saher, and H.-J. Sommers: Statistics of complex levels of random matrices for decaying systems. *Z. Phys. B* **88**, 359 (1992).
- [Haa18] F. Haake, S. Gnutzmann, and M. Kuś: *Quantum Signatures of Chaos. 4th edition*. Springer Berlin 2018.
- [Hau52] W. Hauser and H. Feshbach: The inelastic scattering of neutrons. *Phys. Rev.* **87**, 366–373 (1952).
- [Hil98] D. A. Hill: Plane wave integral representation for fields in reverberation chambers. *IEEE transactions on electromagnetic compatibility* **40**, 209–217 (1998).
- [Hil09] D. A. Hill: *Electromagnetic fields in cavities: deterministic and statistical theories*. John Wiley & Sons 2009.
- [Hö24] H. Hörner, L. Wild, Y. Slobodkin, G. Weinberg, O. Katz, and S. Rotter. Coherent perfect absorption of arbitrary wavefronts at an exceptional point. arXiv:2404.04151, 2024.

-
- [Hof21] T. Hofmann, J. Lu, U. Kuhl, and H.-J. Stöckmann: Spectral duality in graphs and microwave networks. *Phys. Rev. E* **104**, 045211 (2021).
- [Hsu16] C. W. Hsu, B. Zhen, A. D. Stone, J. D. Joannopoulos, and M. Soljačić: Bound states in the continuum. *Nature Reviews Materials* **1**, 1–13 (2016).
- [Hul04] O. Hul, S. Bauch, P. Pakoński, N. Savytsky, K. Życzkowski, and L. Sirko: Experimental simulation of quantum graphs by microwave networks. *Phys. Rev. E* **69**, 056205 (2004).
- [Hul12] O. Hul, M. Ławniczak, S. Bauch, A. Sawicki, M. Kuś, and L. Sirko: Are scattering properties of graphs uniquely connected to their shapes?. *Phys. Rev. Lett.* **109**, 040402 (2012).
- [Ing22] M. Ingrebeau: Scattering resonances of large weakly open quantum graphs. *Pure and Applied Analysis* **4**, 49 (2022).
- [Ino99] S. Inouye, A. P. Chikkatur, D. M. Stamper-Kurn, J. Stenger, D. E. Pritchard, and W. Ketterle: Superradiant rayleigh scattering from a bose-einstein condensate. *Science* **285**, 571–574 (1999).
- [Jia24] X. Jiang, S. Yin, H. Li, J. Quan, H. Goh, M. Cotrufo, J. Kullig, J. Wiersig, and A. Alù: Coherent control of chaotic optical microcavity with reflectionless scattering modes. *Nature Physics* **20**, 109–115 (2024).
- [Joy14] C. H. Joyner, S. Müller, and M. Sieber: GSE statistics without spin. *Europhys. Lett.* **107**, 50004 (2014).
- [Kai14] N. Kaina, M. Dupré, M. Fink, and G. Lerosey: Hybridized resonances to design tunable binary phase metasurface unit cells. *Opt. Express* **22**, 18881–18888 (2014).
- [Kan21] Y. Kang and A. Z. Genack: Transmission zeros with topological symmetry in complex systems. *Phys. Rev. B* **103**, L100201 (2021).
- [Kil02] P.-S. Kildal, K. Rosengren, J. Byun, and J. Lee: Definition of effective diversity gain and how to measure it in a reverberation chamber. *Microwave and Optical Technology Letters* **34**, 56–59 (2002).
- [Kil04] P.-S. Kildal and K. Rosengren: Correlation and capacity of mimo systems and mutual coupling, radiation efficiency, and diversity gain of their antennas: simulations and measurements in a reverberation chamber. *IEEE Communications Magazine* **42**, 104–112 (2004).
- [Kö10] B. Köber, U. Kuhl, H.-J. Stöckmann, T. Gorin, D. V. Savin, and T. H. Seligman: Microwave fidelity studies by varying antenna coupling. *Phys. Rev. E* **82**, 036207 (2010).
- [Kop10] M. Kopp and H. Schomerus: Fractal Weyl laws for quantum decay in dynamical systems with a mixed phase space. *Phys. Rev. E* **81**, 026208 (2010).
- [Kot97] T. Kottos and U. Smilansky: Quantum chaos on graphs. *Phys. Rev. Lett.* **79**, 4794 (1997).
- [Kot99] T. Kottos and U. Smilansky: Periodic orbit theory and spectral statistics for quantum graphs. *Ann. Phys. (N.Y.)* **274**, 76 (1999).

-
- [Kot03] T. Kottos and U. Smilansky: Quantum graphs: a simple model for chaotic scattering. *J. Phys. A* **36**, 3501 (2003).
- [Kot04] T. Kottos and H. Schanz: Statistical properties of resonance widths for open quantum graphs. *Waves in Random Media* **14**, S91 (2004).
- [Kra19] A. Krasnok, D. Baranov, H. Li, M.-A. Miri, F. Monticone, and A. Alú: Anomalies in light scattering. *Adv. Opt. Photon.* **11**, 892–951 (2019).
- [Kuh05] U. Kuhl, H.-J. Stöckmann, and R. Weaver: Classical wave experiments on chaotic scattering. *J. Phys. A* **38**, 10433 (2005).
- [Kuh08] U. Kuhl, R. Höhmann, J. Main, and H.-J. Stöckmann: Resonance widths in open microwave cavities studied by harmonic inversion. *Phys. Rev. Lett.* **100**, 254101 (2008).
- [Kuh13] U. Kuhl, O. Legrand, and F. Mortessagne: Microwave experiments using open chaotic cavities in the realm of the effective Hamiltonian formalism. *Fortschritte der Physik* **61**, 404 (2013).
- [Kuh17] U. Kuhl, O. Legrand, F. Mortessagne, K. Oubaha, and M. Richter. Statistics of reflection and transmission in the strong overlap regime of fully chaotic reverberation chambers. arXiv:1706.04873, 2017.
- [Ławni10] M. Ławniczak, S. Bauch, O. Hul, and L. Sirko: Experimental investigation of the enhancement factor for microwave irregular networks with preserved and broken time reversal symmetry in the presence of absorption. *Phys. Rev. E* **81**, 046204 (2010).
- [Ławni17] M. Ławniczak, M. Białous, V. Yunko, S. Bauch, B. Dietz, and L. Sirko: Analysis of missing level statistics for microwave networks simulating quantum chaotic graphs without time reversal symmetry—the case of randomly lost resonances. *Acta Physica Polonica A* **132**, 1672 (2017).
- [Ławni19] M. Ławniczak, Jiří Lipovský, and L. Sirko: Non-Weyl microwave graphs. *Phys. Rev. Lett.* **122**, 140503 (2019).
- [Ławni24] M. Ławniczak, A. Akhshani, O. Farooq, S. Bauch, and L. Sirko: Experimental distributions of the reflection amplitude for networks with unitary and symplectic symmetries. *Acta Physica Polonica A ISSN 1898-794X* **144**, 469 (2024).
- [Leh95a] N. Lehmann, D. Saher, V. V. Sokolov, and H.-J. Sommers: Chaotic scattering: the supersymmetry method for large number of channels. *Nucl. Phys. A* **582**, 223 (1995).
- [Leh95b] N. Lehmann, D. V. Savin, V. V. Sokolov, and H.-J. Sommers: Time delay correlations in chaotic scattering: Random matrix approach. *Physica D* **86**, 572 (1995).
- [Lew91] C. H. Lewenkopf and H. A. Weidenmüller: Stochastic versus semiclassical approach to quantum chaotic scattering. *Ann. Phys. (N.Y.)* **212**, 53 (1991).
- [Li17] H. Li, S. Suwunnarat, R. Fleischmann, H. Schanz, and T. Kottos: Random matrix theory approach to chaotic coherent perfect absorbers. *Phys. Rev. Lett.* **118**, 044101 (2017).

-
- [Li19] C. Li, J. Qiu, J.-Y. Ou, Q. H. Liu, and J. Zhu: High-sensitivity refractive index sensors using coherent perfect absorption on graphene in the vis-nir region. *ACS Applied Nano Materials* **2**, 3231–3237 (2019).
- [Lim04] S.-H. Lim, T. G. Bjorklund, F. C. Spano, and C. J. Bardeen: Exciton delocalization and superradiance in tetracene thin films and nanoaggregates. *Phys. Rev. Lett.* **92**, 107402 (2004).
- [Lip15] J. Lipovský: Pseudo-orbit expansion for the resonance condition on quantum graphs and the resonance asymptotics. *Acta Physica Polonica A* **128**, 968 (2015).
- [Lu03] W. T. Lu, S. Sridhar, and M. Zworski: Fractal Weyl laws for chaotic open systems. *Phys. Rev. Lett.* **91**, 154101 (2003).
- [Lu20] J. Lu, J. Che, X. Zhang, and B. Dietz: Experimental and numerical investigation of parametric spectral properties of quantum graphs with unitary or symplectic symmetry. *Phys. Rev. E* **102**, 022309 (2020).
- [Lu24] J. Lu, T. Hofmann, H.-J. Stöckmann, and U. Kuhl. Non-weyl behavior induced by superradiance: A microwave graph study. arXiv:2406.11606, 2024.
- [Ma24] S. Ma and S. M. Anlage: Experimental realization of anti-unitary wave-chaotic photonic topological insulator graphs showing kramers degeneracy and symplectic ensemble statistics. *Advanced Optical Materials* **12**, 2301852 (2024).
- [Mag99] A. I. Magunov, I. Rotter, and S. I. Strakhova: Laser-induced resonance trapping in atoms. *J. Phys. B* **32**, 1669 (1999).
- [Mah69] C. Mahaux and H. A. Weidenmüller: *Shell-Model Approach to Nuclear Reactions*. North-Holland Amsterdam 1969.
- [Mai99] J. Main: Use of harmonic inversion techniques in semiclassical quantization and analysis of quantum spectra. *Phys. Rep.* **316**, 233 (1999).
- [Mar92] C. M. Marcus, A. J. Rimberg, R. M. Westervelt, P. F. Hopkins, and A. C. Gossard: Conductance fluctuations and chaotic scattering in ballistic microstructures. *Phys. Rev. Lett.* **69**, 506 (1992).
- [Meh91] M. L. Mehta: *Random Matrices (Revised and Enlarged Second Edition)*. Academic Press San Diego 1991.
- [Mén03] R. A. Méndez-Sánchez, U. Kuhl, M. Barth, C. H. Lewenkopf, and H.-J. Stöckmann: Distribution of reflection eigenvalues in absorbing chaotic microwave cavities. *Phys. Rev. Lett.* **91**, 174102 (2003).
- [Men17] C. Meng, X. Zhang, S. T. Tang, M. Yang, and Z. Yang: Acoustic coherent perfect absorbers as sensitive null detectors. *Scientific reports* **7**, 43574 (2017).
- [Mor93] F. Mortessagne, O. Legrand, and D. Sornette: Transient chaos in room acoustics. *Chaos* **3**, 529 (1993).
- [Non05] S. Nonnenmacher and M. Zworski: Fractal Weyl laws in discrete models of chaotic scattering. *J. Phys. A* **38**, 10683 (2005).

-
- [Osm20] M. Osman and Y. V. Fyodorov: Chaotic scattering with localized losses: s -matrix zeros and reflection time difference for systems with broken time-reversal invariance. *Phys. Rev. E* **102**, 012202 (2020).
- [Oub18] K. Oubaha, M. Richter, U. Kuhl, F. Mortessagne, and O. Legrand. Refining the experimental extraction of the number of independent samples in a mode-stirred reverberation chamber. In *2018 International Symposium on Electromagnetic Compatibility (EMC EUROPE)* pages 719–724 2018.
- [Oub20] K. Oubaha. *Transport micro-ondes dans un milieu complexe vers une communication sans fil à base des circuits intégrés*. Dissertation at Université Côte d’Azur, 2020.
- [Özd19] Ş. K. Özdemir, S. Rotter, F. Nori, and L. Yang: Parity–time symmetry and exceptional points in photonics. *Nature Materials* **18**, 783 (2019).
- [Pau36] L. Pauling: The diamagnetic anisotropy of aromatic molecules. *J. Chem. Phys.* **4**, 673 (1936).
- [Pen14] B. Peng, Ş. K. Özdemir, S. Rotter, H. Yilmaz, M. Liertzer, F. Monifi, C. M. Bender, F. Nori, and L. Yang: Loss-induced suppression and revival of lasing. *Science* **346**, 328–332 (2014).
- [Per98] E. Persson, T. Gorin, and I. Rotter: Resonance trapping and saturation of decay widths. *Phys. Rev. E* **58**, 1334 (1998).
- [Per99] E. Persson and I. Rotter: Doorway concept at high excitation energy. *Phys. Rev. C* **59**, 164 (1999).
- [Per00] E. Persson, I. Rotter, H.-J. Stöckmann, and M. Barth: Observation of resonance trapping in an open microwave cavity. *Phys. Rev. Lett.* **85**, 2478 (2000).
- [Pic19] K. Pichler, M. Kühmayer, J. Böhm, A. Brandstötter, P. Ambichl, U. Kuhl, and Stefan Rotter: Random anti-lasing through coherent perfect absorption in a disordered medium. *Nature* **567**, 351 (2019).
- [Pie14] R. Pierrat, P. Ambichl, S. Gigan, A. Haber, R. Carminati, and S. Rotter: Invariance property of wave scattering through disordered media. *Proceedings of the National Academy of Sciences* **111**, 17765–17770 (2014).
- [Plu14] Z. Pluhař and H. A. Weidenmüller: Universal quantum graphs. *Phys. Rev. Lett.* **112**, 144102 (2014).
- [Por65] C. E. Porter: *Statistical Theory of Spectra: Fluctuations*. Academic Press New York 1965.
- [Pot12] A. Potzuweit, T. Weich, S. Barkhofen, U. Kuhl, H.-J. Stöckmann, and M. Zworski: Weyl asymptotics: From closed to open systems. *Phys. Rev. E* **86**, 066205 (2012).
- [Ra’di15] Y. Ra’di, C. R. Simovski, and S. A. Tretyakov: Thin perfect absorbers for electromagnetic waves: Theory, design, and realizations. *Phys. Rev. Appl.* **3**, 037001 (2015).
- [Reh16] A. Rehemangiang, M. Allgaier, C. H. Joyner, S. Müller, M. Sieber, U. Kuhl, and H.-J. Stöckmann: Microwave realization of the Gaussian symplectic ensemble. *Phys. Rev. Lett.* **117**, 064101 (2016).

-
- [Reh18] A. Rehemanjiang. *Microwave Experiments on Graphs Simulating Spin-1/2 System*. Dissertation at Philipps-Universität Marburg, 2018.
- [Rot01] I. Rotter: Dynamics of quantum systems. *Phys. Rev. E* **64**, 036213 (2001).
- [Rut11] Ernest Rutherford: Lxxix. the scattering of α and β particles by matter and the structure of the atom. *The London, Edinburgh, and Dublin Philosophical Magazine and Journal of Science* **21**, 669–688 (1911).
- [Sav03] D. V. Savin and H.-J. Sommers: Fluctuations of delay times in chaotic cavities with absorption. *Phys. Rev. E* **68**, 036211 (2003).
- [Sav06] D. V. Savin, O. Legrand, and F. Mortessagne: Inhomogeneous losses and complexness of wave functions in chaotic cavities. *Europhys. Lett.* **76**, 774 (2006).
- [Sav17] R. Savo, R. Pierrat, U. Najar, R. Carminati, S. Rotter, and S. Gigan: Observation of mean path length invariance in light-scattering media. *Science* **358**, 765–768 (2017).
- [Sch07] M. Scheibner, T. Schmidt, L. Worschech, A. Forchel, G. Bacher, T. Passow, and D. Hommel: Superradiance of quantum dots. *Nature Physics* **3**, 106–110 (2007).
- [SH10] J. D. Sánchez-Heredia, J. F. Valenzuela-Valdés, A. M. Martínez-González, and D. A. Sanchez-Hernandez: Emulation of mimo rician-fading environments with mode-stirred reverberation chambers. *IEEE Transactions on Antennas and Propagation* **59**, 654–660 (2010).
- [Sig22] O. Sigwarth and C. Miniatura: Time reversal and reciprocity. *AAPPS Bulletin* **32**, 23 (2022).
- [Sim93] B. D. Simons and B. L. Altshuler: Universal velocity correlations in disordered and chaotic systems. *Phys. Rev. Lett.* **70**, 4063 (1993).
- [Sin63] Y. G. Sinai: On the foundations of the ergodic hypothesis for a dynamical system of statistical mechanics. *Sov. Math. Dokl.* **4**, 1818 (1963).
- [Skr73] N. Skribanowitz, I. P. Herman, J. C. MacGillivray, and M. S. Feld: Observation of dicke superradiance in optically pumped hf gas. *Phys. Rev. Lett.* **30**, 309–312 (1973).
- [Sle16] T. Sleasman, M. F. Imani, J. N. Gollub, and D. R. Smith: Microwave imaging using a disordered cavity with a dynamically tunable impedance surface. *Phys. Rev. Appl.* **6**, 054019 (2016).
- [Slo22] Y. Slobodkin, G. Weinberg, H. Hörner, K. Pichler, S. Rotter, and O. Katz: Massively degenerate coherent perfect absorber for arbitrary wavefronts. *Science* **377**, 995–998 (2022).
- [Sok88] V. V. Sokolov and V. G. Zelevinsky: On a statistical theory of overlapping resonances. *Phys. Lett. B* **202**, 10 (1988).
- [Sok89] V. V. Sokolov and V. G. Zelevinsky: Dynamics and statistics of unstable quantum states. *Nucl. Phys. A* **504**, 562 (1989).
- [Sok92] V. V. Sokolov and V. G. Zelevinsky: Collective dynamics of unstable quantum states. *Ann. Phys. (N.Y.)* **216**, 323 (1992).

-
- [Sri91] S. Sridhar: Experimental observation of scarred eigenfunctions of chaotic microwave cavities. *Phys. Rev. Lett.* **67**, 785 (1991).
- [Stö90] H.-J. Stöckmann and J. Stein: “Quantum” chaos in billiards studied by microwave absorption. *Phys. Rev. Lett.* **64**, 2215 (1990).
- [Stö99] H.-J. Stöckmann: *Quantum Chaos - An Introduction*. University Press Cambridge 1999.
- [Stö02] H.-J. Stöckmann, E. Persson, Y.-H. Kim, M. Barth, U. Kuhl, and I. Rotter: Effective Hamiltonian for a microwave billiard with attached waveguide. *Phys. Rev. E* **65**, 066211 (2002).
- [Stö22] H.-J. Stöckmann and U. Kuhl: Microwave studies of the spectral statistics in chaotic systems. *J. Phys. A* **55**, 383001 (2022).
- [Suw22] S. Suwunnarat, Y. Tang, M. Reisner, F. Mortessagne, U. Kuhl, and T. Kottos: Non-linear coherent perfect absorption in the proximity of exceptional points. *Communications Physics* **5**, 5 (2022).
- [Ver85] J. J. M. Verbaarschot, H. A. Weidenmüller, and M. R. Zirnbauer: Grassmann integration in stochastic quantum physics: The case of compound-nucleus scattering. *Phys. Rep.* **129**, 367 (1985).
- [Vol03] A. Volya and V. Zelevinsky: Exploring quantum dynamics in an open many-body system: transition to superradiance. *Journal of Optics B: Quantum and Semiclassical Optics* **5**, S450 (2003).
- [Wan11] W. Wan, Y. Chong, L. Ge, H. Noh, A. D. Stone, and H. Cao: Time-reversed lasing and interferometric control of absorption. *Science* **331**, 889 (2011).
- [Wan21] C. Wang, W. R. Sweeney, A. D. Stone, and L. Yang: Coherent perfect absorption at an exceptional point. *Science* **373**, 1261–1265 (2021).
- [Wan23] X. S. Wang, R. Savo, A. Maeder, F. Kaufmann, J. Kellner, A. Morandi, S. Rotter, R. Sapienza, and R. Grange: Graph model for multiple scattering in lithium niobate on insulator integrated photonic networks. *Opt. Express* **31**, 42255–42270 (2023).
- [Wan24a] C.-Z. Wang, J. Guillamon, W. Tuxbury, U. Kuhl, and T. Kottos. Nonlinearity-induced scattering zero degeneracies for spectral management of coherent perfect absorption in complex systems. arXiv:2403.10690, 2024.
- [Wan24b] C.-Z. Wang, U. Kuhl, A. Dowling, H. Schanz, and T. Kottos: Bound states in the continuum induced via local symmetries in complex structures. *Phys. Rev. Appl.* **22**, 014010 (2024).
- [War03] L. K. Warne, K. S. H. Lee, H. G. Hudson, W. A. Johnson, R. E. Jorgenson, and S. L. Stronach: Statistical properties of linear antenna impedance in an electrically large cavity. *IEEE Transactions on antennas and propagation* **51**, 978–992 (2003).
- [Wea89] R. L. Weaver: Spectral statistics in elastodynamics. *J. Acoust. Soc. Am.* **85**, 1005 (1989).

- [Wei14] P. Wei, C. Croënne, S. T. Chu, and J. Li: Symmetrical and anti-symmetrical coherent perfect absorption for acoustic waves. *Applied Physics Letters* **104**(2014).
- [Wei21] P. Weiss, A. Cipris, R. Kaiser, I. M. Sokolov, and W. Guerin: Superradiance as single scattering embedded in an effective medium. *Phys. Rev. A* **103**, 023702 (2021).
- [Wey12a] H. Weyl: Das asymptotische Verteilungsgesetz der Eigenwerte linearer partieller Differentialgleichungen (mit einer Anwendung auf die Theorie der Hohlraumstrahlung). *Math. Annalen* **71**, 441 (1912).
- [Wey12b] H. Weyl: Über das Spektrum der Hohlraumstrahlung. *Journal für die reine und angewandte Mathematik* **141**, 163 (1912).
- [Wey12c] H. Weyl: Über die Abhängigkeit der Eigenschwingungen einer Membran von deren Begrenzung. *Journal für die reine und angewandte Mathematik* **141**, 1 (1912).
- [Wig55] E. P. Wigner: Characteristic vectors of bordered matrices with infinite dimensions. *Annals of Mathematics* **62**, 548–564 (1955).
- [Won16] Z. J. Wong, Y.-L. Xu, J. Kim, K. O’Brien, Y. Wang, L. Feng, and X. Zhang: Lasing and anti-lasing in a single cavity. *Nature photonics* **10**, 796–801 (2016).
- [Xia12] H. Xia, A. A. Svidzinsky, L. Yuan, C. Lu, S. Suckewer, and M. O. Scully: Observing superradiant decay of excited-state helium atoms inside helium plasma. *Phys. Rev. Lett.* **109**, 093604 (2012).
- [Zak91] J. Zakrzewski and M. Kuś: Distributions of avoided crossings for quantum chaotic systems. *Phys. Rev. Lett.* **67**, 2749 (1991).
- [Zak93a] J. Zakrzewski and D. Delande: Parametric motion of energy levels in quantum chaotic systems. I. Curvature distributions. *Phys. Rev. E* **47**, 1650 (1993).
- [Zak93b] J. Zakrzewski, D. Delande, and M. Kuś: Parametric motion of energy levels in quantum chaotic systems. II. Avoided-crossing distributions. *Phys. Rev. E* **47**, 1665 (1993).
- [Zha22a] W. Zhang, X. Zhang, J. Che, J. Lu, M. Miski-Oglu, and B. Dietz: Experimental study of closed and open microwave waveguide graphs with preserved and partially violated time-reversal invariance. *Phys. Rev. E* **106**, 044209 (2022).
- [Zha22b] Y. Zhang, F.-P. Wu, and H.-F. Zhang: Theoretical model of a ri thz sensor realized by coherent perfect absorption with optical phase modulation. *IEEE Sensors Journal* **22**, 14842–14850 (2022).
- [Zwo89] M. Zworski: Sharp polynomial bounds on the number of scattering poles. *Duke Math. J.* **59**, 311 (1989).